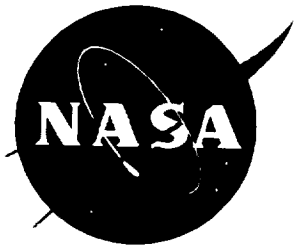

NASA Contractor Report 4625

Design of Passive Piezoelectric Damping for Space Structures

Nesbitt W. Hagood IV and Jack B. Aldrich
Massachusetts Institute of Technology • Cambridge, Massachusetts

Andreas H. von Flotow
Mide Technology Corporation • Hood River, Oregon

National Aeronautics and Space Administration
Langley Research Center • Hampton, Virginia 23681-0001

Prepared for Langley Research Center
under Contract NAS1-19381

September 1994

Abstract

Passive damping of structural dynamics using piezoceramic electromechanical energy conversion and passive electrical networks is a relatively recent concept with little implementation experience base. This report describes an implementation case study, starting from conceptual design and technique selection, through detailed component design and testing to simulation on the structrure to be damped. About 0.5kg. of piezoelectric material was employed to damp the ASTREX testbed, a 5000kg structure. Emphasis was placed upon designing the damping to enable high bandwidth robust feedback control. Resistive piezoelectric shunting provided the necessary broadband damping. The piezoelectric element was incorporated into a mechanically-tuned vibration absorber in order to concentrate damping into the 30 to 40Hz frequency modes at the rolloff region of the proposed compensator. A prototype of a steel flex-tensional motion amplification device was built and tested. The effective stiffness and damping of the flex-tensional device was experimentally verified. When six of these effective springs are placed in an orthogonal configuration, strain energy is absorbed from all six degrees of freedom of a 90kg. mass.

A NASTRAN finite element model of the testbed was modified to include the six-spring damping system. An analytical model was developed for the spring in order to see how the flex-tensional device and piezoelectric dimensions effect the critical stress and strain energy distribution throughout the component. Simulation of the testbed demonstrated the damping levels achievable in the completed system.

Acknowledgments

This work was sponsored by NASA Contract NAS1-19381. This report is based on the unaltered thesis of Jack Aldrich submitted to the Department of Aeronautics and Astronautics in partial fulfillment of the requirements for the degree of Master of Science at the Massachusetts Institute of Technology

Table of Contents

Abstract iii
Acknowledgments iv
Nomenclature vii
Relevent Key Words ix
Chapter I. Introduction 1
1.1. Motivation 1
1.2. Objective 3
1.3. Background: Passive Damping Mechanisms 5
1.4. Approach: Piezoelectric Passive Damping 8
1.4.1. Modeling of Shunted Piezoelectrics 9
1.4.2. Resistive versus Resonant Shunted Piezoelectrics 10
1.4.3. Resistive Shunted Piezoelectric Material Properties 10
1.4.4. Resonant Shunted Piezoelectric Material Properties 12
1.4.5. Coupling Shunted Piezoelectrics to Structures 13
1.4.6. Finite Element Modeling of Piezoelectric-based Dampers 14
Chapter II. Potential Piezoelectric Damping Implementations for ASTREX 16
2.1. Potential Damping Device: Smart Joint 17
2.1.1. Piezoelectric Washer Design 19
2.1.2. Piezoelectric Washer Manufacturing Issues 20
2.1.3. Piezoelectric Washer Stress Analysis 22
2.1.4. Alternative "Smart Joint" Designs 23
2.2. Potential Damping Device: Six-Axis Vibration Absorber 25
2.3. Damping Performance: Smart Joint versus 6-axis Absorber 27
Chapter III. Design and Analysis of the Flex-Tensional Component 29
3.1. Design Details of the Flex-Tensional Device 30
3.2. Device Analysis: Analytical Truss Model 31
3.2.1. Kinematic Derivation of Effective Stiffness 31
3.2.2. Truss Model Design of the Component 33
3.3. Device Analysis: NASTRAN Finite Element Model 36
3.4. Comparison of Analytical Truss and NASTRAN Models 42
3.5. The New Component Design 45
3.5.1. Local Elasticity Analysis and Model Refinement 45
3.5.2. Second Iteration Device Optimization with NASTRAN 47
Chapter IV. Experimental Verification of Component Performance 54

4.1. The Component Tester Hardware....55
4.2. Calibrating the Component Tester....58
4.3. Component Test Data....59
4.4. Component Experimental Results Summary....61
Chapter V. Simulated Frequency Response Performance for ASTREX....63
5.1. Finite Element Formulation and Solution Algorithms of the Damped Testbed Model....64
5.2. Line-of-Sight Performance Transfer Functions....68
5.3. Isolation System Performance Transfer Function....71
Chapter VI. Conclusions and Recommendations....72
Appendix I: Analytical Finite Element Component Model....75
Appendix II: Low-Frequency ASTREX Mode Shapes....92
Bibliography....93

Nomenclature

A	diagonal matrix of cross-sectional areas of piezoelectric bar
B	magnetic field
C	generic capacitance, farads
d_{ij}	piezoelectric material constant relating voltage in *i*th direction to strain in the *j*th direction
D	vector of electrical displacements (charge/area)
E	Young's Modulus, elastic field
E	vector of electric fields (volts/meter)
g	$= \omega/\omega_n$, real non-dimensional frequency ratio
G	shear modulus
I	vector of external applied currents
J	torsional constant
K	modal stiffness
k_{ij}	material electromechanical coupling coefficient
K_{ij}	generalized electromechanical coupling coefficient
L	diagonal matrix of lengths of piezoelectric bar
L	generic inductor, Henry's
M	modal mass
r	dissipation tuning parameter
R	generic resistance, ohms
s	Laplace parameter
s^E	piezoelectric material compliance matrix at constant electric field
S	vector of material engineering strains
T	vector of material stresses
U_i	strain energy in element *i*
V	voltage
β	semi-rigid beam stiffness ration, p 95
ζ	damping coefficient
γ	$= s/\omega_n$, complex non-dimensional frequency
δ	$= \omega_e/\omega_n$, resonant shunted piezoelectric frequency tuning parameter
η	loss factor
ρ	=RCω, non-dimensional resistance (or frequency)
ω_n	natural frequency of a one-degree of freedom system
ω_e	resonant shunted piezoelectric electrical resonant frequency

τ	shear stress (Pascals)
σ	normal stress (Pascals)
f	freqnency, force
Λ	diagonal matrix of the squares of the natural frequency
ϕ	real or normal mode of the system, electric potential
θ	flex-tensional component lever angle

Subscripts:

oc	open circuit
sc	short circuit
f	flexure
piezo	piezoelectric material
eff	effective properties
t	transpose of a vector or matrix

Superscripts:

E	value taken at constant field (short circuit)
D	value taken at constant electrical displacement (open circuit)
S	value taken at constant strain (clamped)
T	value taken at constant stress (free)

Relevant Key Words

ASTREX: Air Force Phillip's Laboratory Advanced Space Structure Research Experiment facility at Edwards Air Force Base

Collocation: 1. collocated actuators and sensors are located at same point on the structure. 2. collocated transfer functions have their input and output at the same point on the model.

Complex mode: modeshape associated to a single pole, complex modes come in complex conjugate pairs.

Component: the essential part or mechanism of the damper. *(i.e. the flex-tensional)*

Damper: any damping implementation *(i.e. washer or six-axis vibration absorber)* or any damping component *(i.e. flex-tensional or washer)*

Device: any damping implementation with a distinctive mechanism and damping material. *(i.e. the piezoelectric-based flex-tensional or the six-axis vibration absorber)*

Flex-tensional: steel part that uses preloaded flexured lever arms to amplify the stroke of the piezoelectric

Non-proportional damping: damping implementation that influences collocated and adjacent degrees of freedom. *i.e. off-diagonal damping terms in damping matrix and coupled equations of motion*

Orthogonal: 1. matrices whose product is zero are mutually orthogonal. (decoupling the equations of motion). 2. truss struts that are orthogonal are perpendicular to each other (decoupling their control authority).

Proof mass damper: synonym for six-axis vibration absorber.

Proportional damping: damping implementation that influences collocated degrees of freedom only. Mass-proportional damping is excluded in this definition. *i.e. diagonal damping matrix and decoupled equations of motion*

Real or normal mode: modeshape associated to a pair of complex conjugate poles. The definition of such modes implies the assumption of proportional damping.

Six-axis vibration absorber: three pairs of orthogonal flex-tensional dampers whose purpose is to absorb the energy of a 90kg proof mass via shunted piezoelectics

Six-axis vibration isolator: three pairs of orthogonal flex-tensional actuators whose purpose is to isolate the 90kg proof mass from ASTREX dynamics via actuated piezoelectrics

Smart Joint: rotary damper/actuator combination that absorbs or commands tripod-end rotations via shunted/actuated piezoelectrics *(i.e. washer, sleeve or equivalent strut)*

CHAPTER 1

INTRODUCTION

Most modern spacecraft, including the proposed Space Station, need a means to isolate precision-pointing instruments or microgravity experiments from the unpleasant dynamics that are inherent to large flexible space trusses. Various disturbances can excite the spacecraft's structural dynamics: a thrusting maneuver, a shuttle docking, an astronaut's movement, onboard machinery or solar dust impacting to name a few. In order to prevent any of these disturbances from propagating through the truss to the sensitive equipment, a device must be designed to damp and/or isolate the performance-sensitive vibrations that are excited by predicted disturbances. The implementation usually requires passive and active stages, consisting of a passive structural damping implementation, and an isolation control system, respectively.

1.1 MOTIVATION

There are many other applications where the addition of passive vibration damping to a structural system can greatly increase the system's performance or stability. For example, bridges and buildings need to damp the destructive dynamics from earthquakes. Automobiles need to be isolated from rough road surfaces. In any case, the addition of passive damping can decrease peak vibration amplitudes in structural systems and add robustness to marginally stable active control systems Refs.[1, 2, 3]. Since the actual system modes are rarely in complete agreement with the model, even the modeled modes pose some threat to the stability of the closed loop system. In addition, lightly damped

modes can exist in the rolloff region of the control system. Although these modes may not be included in the model, they are still subject to control authority that has not yet rolled off. These rolloff modes pose another threat of instability to the control designer.

There are several sources of passive damping in space structures. The most common is material damping by which structural strain energy is dissipated. Damping is also provided by the friction and impacting that occur in the structural joints. The inherent damping in a truss can be increased by using damping enhancement schemes Refs.[3, 4, 25, 26, 27, 28]. Several damping techniques are applicable to space structures. Some viscoelastic techniques have been developed for trusses in Ref. [5]. Proof-mass dampers (PMD's) have been applied previously to space structure damping in Ref. [14] and conceptually in Ref. [23]. Viscous damping struts were implemented in Ref. [7]. An active thermal damping scheme was used in Ref. [8]. Impact dampers were used in Ref. [9]. Truss structures with active piezoelectric members for vibration suppression are presented in Refs. [10, 14, 24].

With the advent of smart materials, like piezoelectrics, it is possible to sense, control and passively damp structural vibrations with the same device, simultaneously. Using passive electrical networks, such as resistor-capacitor (RC) and inductor-resistor-capacitor (LRC) circuits, the device can absorb vibrations with minimal mass penalty.

In recent years, piezoelectric elements have been used as embedded sensors and actuators in smart structures by Forward[11], Crawley and De Luis[13], and Hagood and Crawley[14], and as elements of active structural vibration systems by Fanson and Caughey[6], Hanagud *et al.* [15], and Bailey and Hubbard[16]. They have also been used as actuation components in wave control experiments by Pines and von Flotow [17]. Within active control systems, the piezoelectrics require complex amplifiers and associated sensing electronics. These can be eliminated in passive shunting applications where the only external element is a simple passive electrical circuit. Modelling of passive piezoelectric damping is described in Ref. [4]. Experimental verification of passive piezoelectric damping in a laboratory structure is described in Ref. [4, 14]. The shunted piezoelectric itself could also be used as a damped structural actuator in a control system, as will be discussed later in this paper.

This report will present a passive piezoelectric damping implementation on Air Force Phillip's Laboratory Advanced Space Structure Research Experiment (ASTREX) facility at Edwards Air Force Base, figures 1 and 2. The motivation behind this research is to provide as much passive damping as possible to facilitate Line-Of-Sight control roll-off. Passively-shunted piezoelectrics were the chosen damping scheme because of their small implementation experience base relative to the viscoelastic or viscous damping schemes.

Piezoceramic's high stiffness and temperature stability make it useful for structural damping applications.

In chapter 1, the modeling and passive damping issues of shunted piezoelectrics are defined. In chapter 2, potential damping implementations, and control objectives are introduced for ASTREX. In chapter 3, the design, manufacturing and assembly details of the better device from the previous section is explained. This chapter also describes analytical and finite element modeling techniques of the component. Chapter 4 gives the experimental verification of the component. Chapter 5 simulates the damping performance of the six-axis proof mass dynamic absorber in the ASTREX testbed. Conclusions are summarized in Chapter 6.

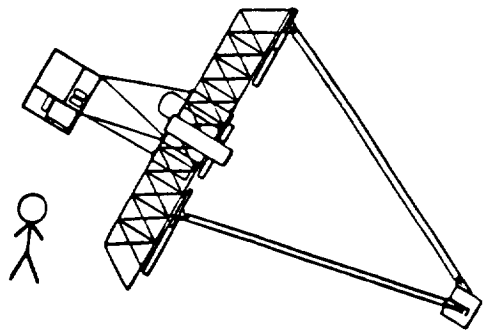

Figure 1. ASTREX space structure with scaled six-foot figure. Support pedestal that elevates the center of the truss from the lab floor is not shown.

1.2 OBJECTIVE

The objective of this study was to develop optimal damping/actuation mechanisms that demonstrate the virtues of passive damping for spacecraft performance and control. Before the passive damping implementation ideas can be generated, the characteristics and performance criteria of the undamped structure, ASTREX, must be considered. After all, the development of piezoelectric dampers, actuators and sensors must be guided by the performance-sensitive dynamics and control architectures of the specific class of structures to be damped.

ASTREX consists of two major parts, a vertical pedestal upon which the test-article pivots through an air-bearing system. The mass center is positioned such that the test-article points downward from the horizontal position by about 30 degrees. The ASTREX test article includes a tripod that supports a mirror known as the secondary (figure 2). The primary consists of over a hundred 1 meter back plane struts that form a hexagonal-shaped

lattice truss. The tertiary, located a couple of meters behind the primary, houses the electronics. Thrusters, located on opposite sides of the primary, are available to perform rapid slewing maneuvers. Two control moment gyros are placed on the primary, as are two reaction wheels on the secondary.

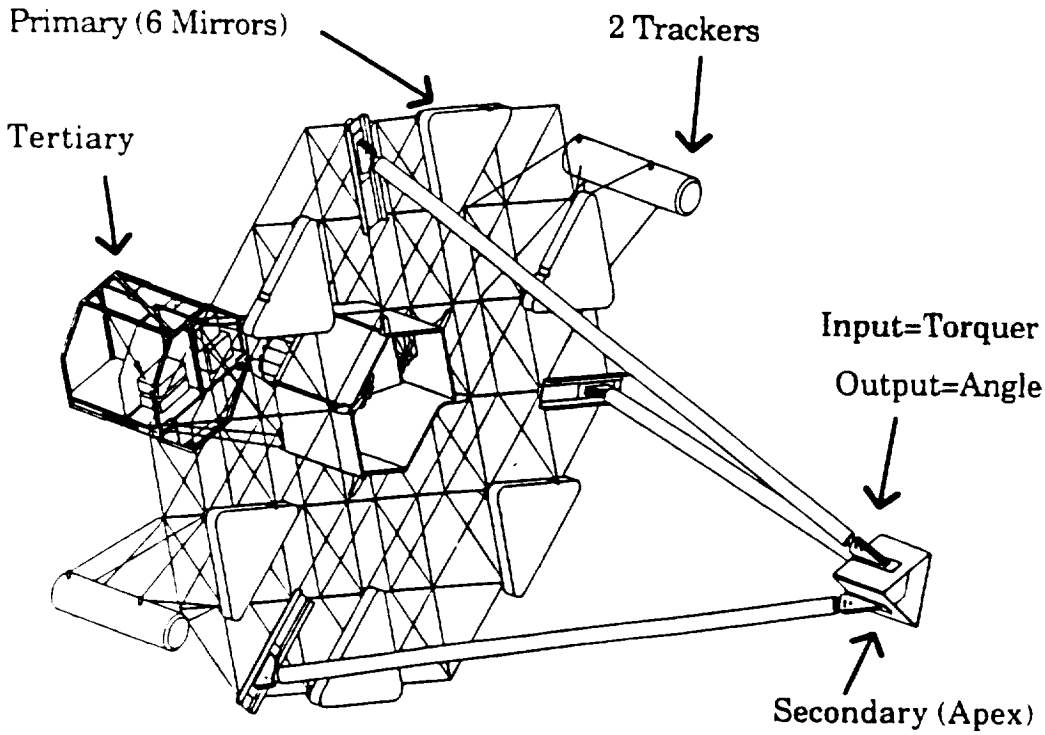

Figure 2. ASTREX space structure overview.

ASTREX's original control-structures interaction performance-metric, involved minimizing the line-of-sight error from step input slewing maneuvers. For purposes of this project, we have assumed use of the two reaction wheels on the secondary as control actuators for line of sight. The frequency response of this transfer function (from torque applied to line-of-sight) for the undamped structure is reproduced in chapter five. From considerations of practical bandwidth limits of the reaction-wheel actuators, together with knowledge of the capability of fast steering mirrors (which might be used in a fast, but small-angle inner loop), the 30 to 40Hz frequency range was selected as a target closed-loop bandwidth for this control loop. Eigenfrequencies below this bandwidth would be actively controlled. Eigenfrequencies near the 30 to 40Hz cross-over would present robust stability problems. Eigenfrequencies far above this bandwidth will need enough passive damping for gain stabilization as depicted in figure 3.

These heuristic considerations, codified in [18], lead us to emphasize passive damping . treatments that target the decade centered about 30 to 40Hz, and target modes which contribute strongly to rotational motion of the secondary.

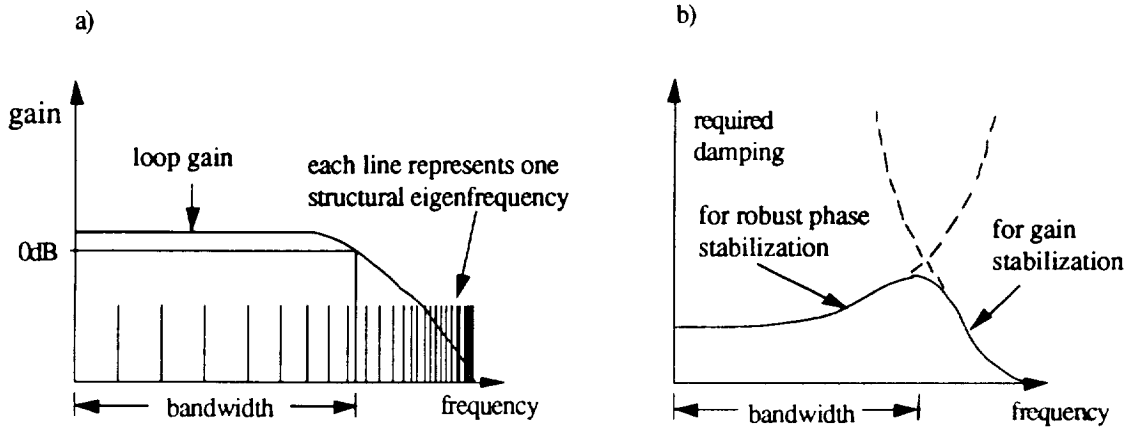

Figure 3. Phase and Gain Stabilization issues. (a) Figurative depiction of testbed for bandwidth to include many poorly modeled, lightly damped, closely spaced modes. (b) Required level of passive damping to meet problem specification. Reference [1].

1.3. BACKGROUND: PASSIVE DAMPING MECHANISMS

The are many passive damping implementations which can be applied to large space structures. For example, lossy materials can be applied to critical surfaces of the structure to absorb strain energy. Structural members can be replaced with smart struts or actuators to provide passive damping and active control. Vibrational energy in the host structure can be dumped into active/passive tuned mass dampers, that are attached to the existing structure to absorb vibrational energy. Regardless of the damping implementation employed, the type of energy dissipation must be selected from conventional techniques or a growing number of new options being developed in smart materials technology.

In the following seven paragraphs, viscoelastic, viscous, frictional, impact, thermal, electromechanical, and magnetomechanical energy dissipation techniques that are applicable to large spacecraft structures are presented.

Viscoelastic damping dissipates structural strain energy that is virtually proportional to the velocity of relative movement. Since viscoelastic materials cannot be depended on for their structural integrity, viscoelastics are generally shear strained only as in the composite strut application seen in figure 4.

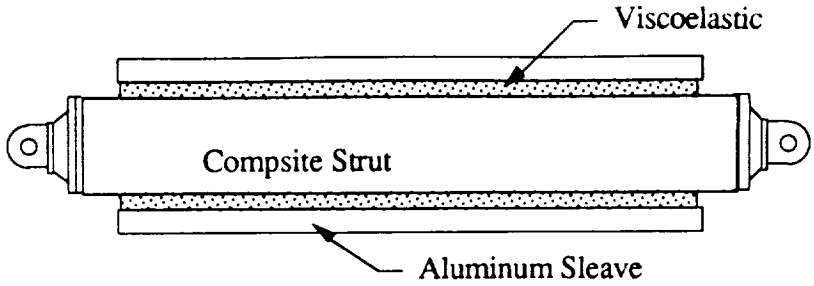

Figure 4. Composite strut with viscoelastic/sleeve damping application.

As the strut undergoes an axial deformation the viscoelastic provides a resistive force proportional to the relative velocity between the composite strut and the sleeve.

Viscous dampers, like the Honeywell D-Strut, depend on the fluid flow through a small internal orifice to obtain passive damping performance. Analogous to the viscoelastic, the viscous damper has insignificant internal stiffness in its dashpot. Parallel stiffnesses, such as a preload spring, or the stiff housing in figure 5, must be created to give the device structural integrity while allowing enough deformation for forced fluid flow through the bellows. As the strut in figure 5, undergoes an axial displacement, the annulus is compressed near the arch flexures, and fluid is forced into the bellows proportional to the velocity of oscillation.

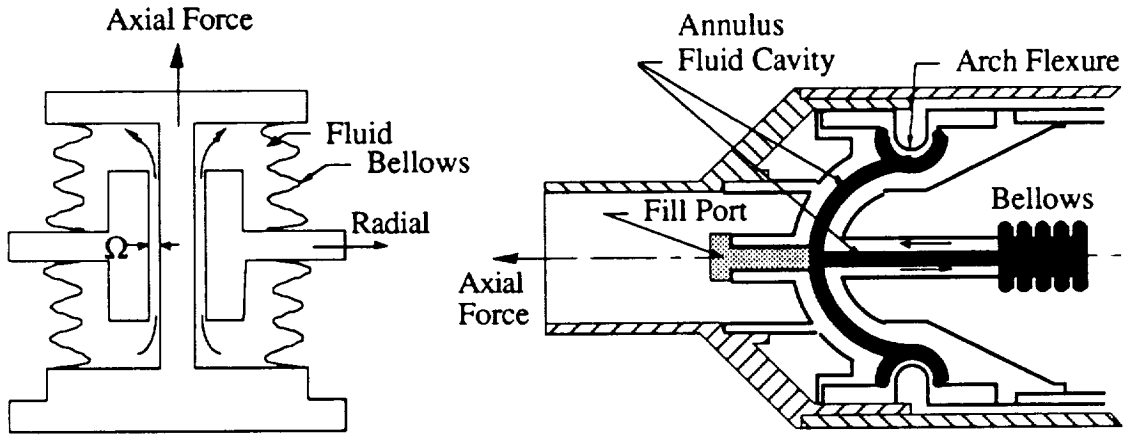

Figure 5. (a) Simplified schematic for the viscous damper. (b) D-strut.

When the fluid elastic actuator in figure 6 is used actively, a commanded force controls the fluid pressure, which in turn elongates the strut. The pressurized composite cylinder supports structural loads. Like other viscous dampers, the P-strut also uses viscous fluid flow through an orifice to provide passive damping.

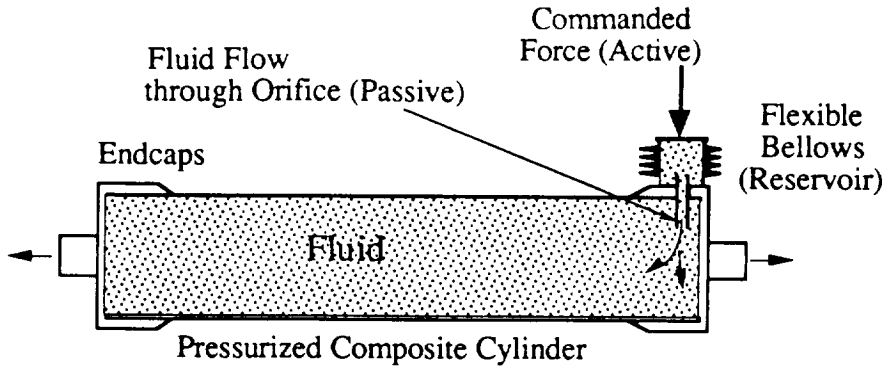

Figure 6. P-Strut: Fluid Elastic Actuator

Frictional or Coulomb damping is another form of damping that results from the sliding of two dry surfaces. The damping force is equal to the product of the normal force and the coefficient of friction, μ, and is assumed to be independent of the velocity, once motion is initiated. Since large space structures have large beam stiffnesses with small displacements compared to civil structures, it is difficult to build a frictional damper that is not burdened by overcoming static friction.

Impact dampers, also known as acceleration dampers, operate by allowing a series of collisions between the primary vibrating system and a secondary mass carried in or on the primary mass (figure 7). Since conservation of momentum is needed to model the damping, velocity proportional damping cannot be assumed in the equations of motion. However, it has been determined in reference [9] that the device is most efficient if two impacts per cycle occur with impacts equally spaced in time.

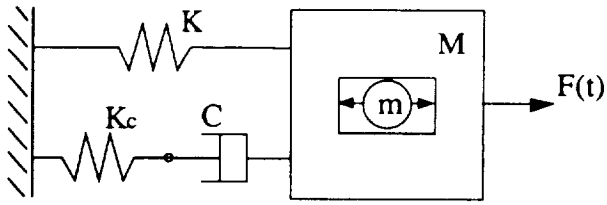

Figure 7. Simple impact damper.

Adaptive damping for spacecraft by temperature control was investigated in reference [8]. The objective of this type of damping is to use the damping material's temperature dependence as a control parameter to adjust the damping value. Controlling the damping of various modes of vibration in a structural system can be accomplished by varying the temperature of the appropriate damping elements through the use of individual heating elements. Since the heating elements and the damping materials are embedded directly

within a composite material of low thermal conductivity, the temperature within each control point can be easily controlled with a minimum of heat input and very little cross coupling between the control points.

Electromechanical energy dissipation techniques, such as resistively-shunted piezoelectrics used in reference [4], convert mechanical strain energy into electrical energy that is then dissipated across a resistor. A piezoelectric truss strut is depicted in figure 8. Truss structures with active piezoelectric members for vibration suppression are presented in Refs. [10, 14]. Magnetostrictives dissipate energy in a similar manner, by converting mechanical strain energy into a magnetically-induced current, that flows through a spiral coil, and is dissipated across a resistor. Since passive piezoelectric damping technique was used exclusively in this thesis, the next section presents a more thorough discussion of passive piezoelectric damping from a modelling point of view.

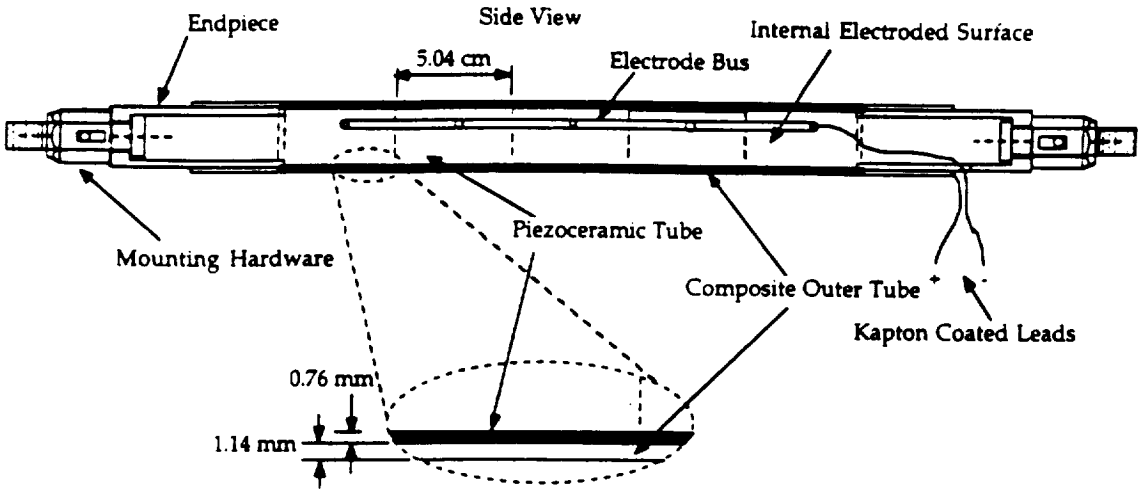

Figure 8. Piezoelectric truss member used in the space structure of reference [14].

1.4. APPROACH: PASSIVE PIEZOELECTRIC DAMPING

In this thesis, an attempt has been made to increase the system damping using passive piezoelectric techniques, because the project sponsor wished to emphasize this technique. Passive piezoelectric damping was also the chosen approach by consensus, because of its relatively small implementation experience base compared to the viscoelastic or viscous damping techniques. Piezoelectric damping is also justified by its relative temperature insensitivity compared to other damping schemes, such as the viscoelastic. This exercise was intended to test the suitability of passive piezoelectric damping for damping large scale structures.

1.4.1. MODELING OF SHUNTED PIEZOELECTRICS

Piezoelectric material can be used simultaneously as a passive damper, actuator and sensor. This report focuses on its development as a passive damper. This function, however, is best understood in the context of its other two roles. The model in figure 9 shows that the passive damping shunting current, the actuation current and the applied stress can all be used to strain the piezoelectric. See equation (1). Once the piezoelectric is strained, mechanical energy is converted into electrical energy which is dissipated across a shunting circuit. Thus, the piezoelectric is depicted as an transformer in the network analog in Figure 9(b). This electromechanical coupling gives the piezoelectric its third role as a sensor.

It is possible to choose the shunting parallel circuit impedance, $Z_i^{SU}(s)$, to maximize the effective material loss factor, η. If an appropriate $Z_i^{SU}(s)$ is selected, the cyclic voltage buildup is appropriately phased with the applied stress to yield piezoelectric passive damping. A complete treatment of this concept is given in reference [4]. Once the shunting and electrical impedances are defined by passive damping performance considerations, the current-strain and stress-strain frequency dependent relationships are constrained by equation (1).

$$\mathbf{S} = \left[\mathbf{s}^E - \mathbf{d}_t\mathbf{L}^{-1}\mathbf{Z}^{EL}s\mathbf{A}\mathbf{d}\right]\mathbf{T} + \left[\mathbf{d}_t\mathbf{L}^{-1}\mathbf{Z}^{EL}\right]\mathbf{I} \tag{1}$$

This equation gives the strain, S, for a given applied stress, T, and forcing current, I. Notice that shunting the piezoelectric does not preclude use of the shunted element as an actuator in an active control system but rather modifies the passive characteristics of the actuator.

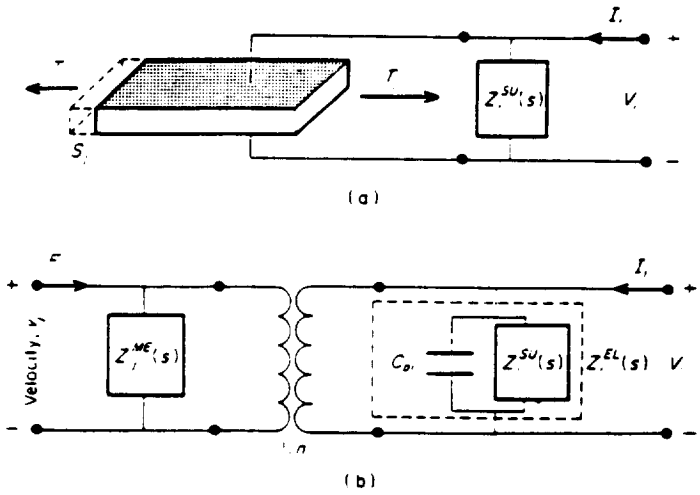

Figure 9. Simple physical model of a uniaxial shunted piezoelectric (a) and its network analog (b).

1.4.2. RESISTIVE VERSUS RESONANT SHUNTED PIEZOELECTRICS

In many applications, it is possible to model the piezoelectric element as loaded in only one of the following three directions: *longitudinal case*, force and field in the "3" direction; *transverse case*, force in "1" or "2" direction, field in "3" direction: *shear case*, force in "4" or "5" direction (shear), field in "2" or "1" direction, respectively (figure 10). If the designer desires broadband damping for the structure, the shunting circuit is a resistor. If the designer desires narrowband damping, both an inductor and a resistor must be shunted across the piezoelectric to form a resonant shunted LRC circuit.

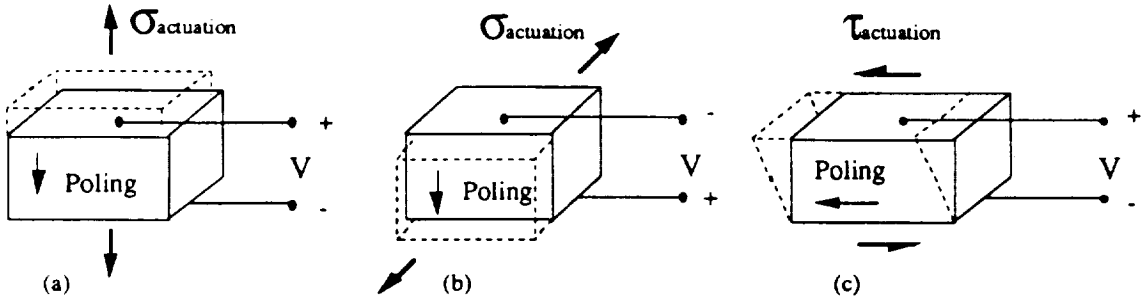

Figure 10. Poling: (a)Longitudinal case. (b)Transverse Case. (c)Shear Case.

In resistively shunted piezoelectric damping, the resistor is varied until the RC circuit time constant, ρ, is in the vicinity of modes to be damped. In resonant shunting, both the inductor and the resistor must be tuned. Such a scheme should only be considered for damping well-modeled structural modes that require excessive damping. This is one reason why resonant circuit shunting was not investigated in this paper. Another option is to tune several inductor and resistor pairs to damp discrete modes as in reference [4].

1.4.3. RESISTIVE SHUNTED PIEZOELECTRIC MATERIAL PROPERTIES

The resistor shunts the electrodes of a piezoelectric element as seen in figure 11.

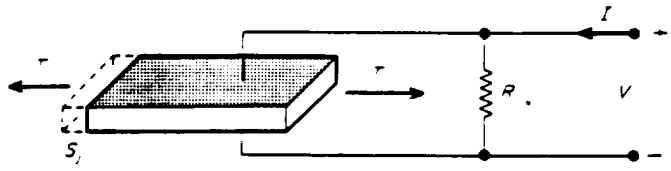

Figure 11. Resistor shunted piezoelectric assumed geometry with forcing in the *j*th direction and electric field in the *i*th direction. Ref. [4].

Deriving the effective material properties from impedance yields the loss factor, η and relative modulus, $\overline{E}$. Ref. [4]:

$$\eta_{ij}^{res}(\omega) = \frac{\rho_i k_{ij}^2}{1+\rho_{ij}^2\left(1-k_{ij}^2\right)} \tag{2}$$

$$\overline{E}_{ij}^{res}(\omega) = 1 - \frac{k_{ij}^2}{1+\rho_{ij}^2\left(1-k_{ij}^2\right)^2} \tag{3}$$

Where ρ_i is the dimensionless frequency:

$$\rho_i = R_i C_{pi}\omega = \frac{\omega}{\omega_d}, \tag{4}$$

The loss factor and relative modulus equations have been plotted versus ρ, the dimensionless frequency (or the dimensionless resistance) in Figure 12 for a typical value of the longitudinal coupling coefficient. These curves are similar to the equivalent material curves for a standard linear solid. As illustrated by the graphs, for a given resistance the stiffness of the piezoelectric changes from its short circuit value at low frequencies to its open circuit value at high frequencies. The frequency of this transition is determined by the shunting resistance. The material also exhibits a maximum loss factor at this transition point.

As seen in figure 12, the material loss factor peaks at 42.5% in the longitudinal and shear cases (k_{33}=k_{13}=0.75). The transverse case has an 8% peak loss factor (k_{15}=0.3).

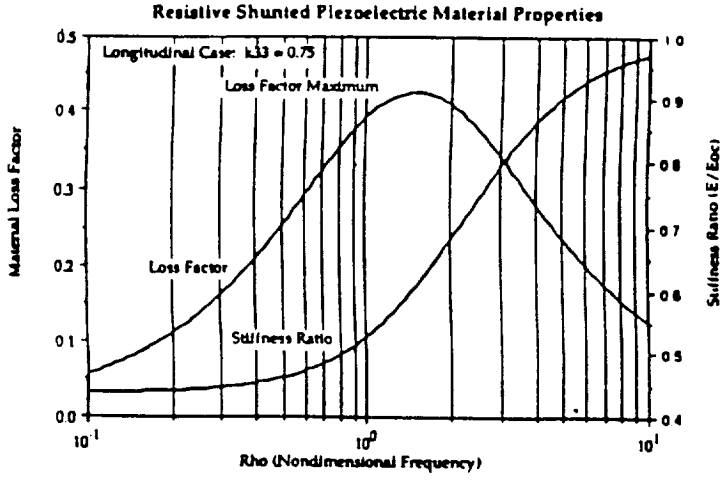

Figure 12. Effective material properties of a resistively shunted piezoelectric in the longitudinal case (k_{33}=0.75) showing material loss factor (solid) and relative modulus (dash). Reference [4].

1.4.4. RESONANT SHUNTED PIEZOELECTRIC MATERIAL PROPERTIES

An inductor and resistor shunt the electrodes of the piezoelectric as seen in figure 13.

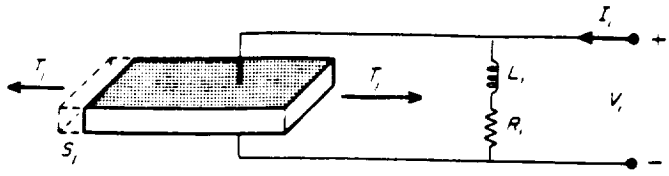

Figure 13. Resonant shunted piezoelectric assumed geometry with forcing in the *j*th direction and electric field in the *i*th direction. Ref. [4].

Deriving the effective material properties from impedance yields the loss factor, η and relative modulus, $\overline{E}$. Ref. [4]:

$$\eta_{ij}^{res}(\omega) = \frac{k_{ij}^2 \delta^2 \left(\delta^2 rg\right)}{\left(\delta^2 - g^2\right)^2 + \left(\delta^2 rg\right)^2 - k_{ij}^2 \delta^2 \left(\delta^2 - g^2\right)} \tag{5}$$

$$\overline{E}_{ij}^{res}(\omega) = 1 - k_{ij}^2 \left(\frac{\delta^2 \left(\delta^2 - g^2\right)}{\left(\delta^2 - g^2\right)^2 + \left(\delta^2 rg\right)^2} \right) \tag{6}$$

where

$$\begin{aligned} g &= \omega/\omega_n = \text{dimensionless frequency} \\ \delta &= \omega_e/\omega_n = \text{tuning ratio} \\ \omega_e &= 1/\sqrt{L_i C_{pi}^S} = \text{electrical resonant frequency.} \end{aligned} \tag{7}$$

The loss factor and relative modulus equations have been plotted versus g, the dimensionless frequency in Figure 5 for a typical value of the coupling coefficient. As illustrated by figure 14, peak loss factors close to 100% are possible. It should also be noted that the stiffness of the piezoelectric changes drastically from its short circuit value at low frequencies to its open circuit value at high frequencies. This stiffness jump at $g = 1$, does not lend itself to the simple optimization techniques used in resistive shunting. Transfer function techniques described completely in reference 4, must be used instead. Sizing the LRC circuit for the smart joint and six-axis damping designs described in the next chapter, yielded 15kH, and 0.4kH inductors, respectively. Inductors as large as these must be simulated with the active inductor techniques described in reference [4]. Despite the feasibility of this design, resonant circuit damping of discrete modes was not

investigated any further. Instead, this research focuses on using broadband damping to facilitate the control of these discrete modes.

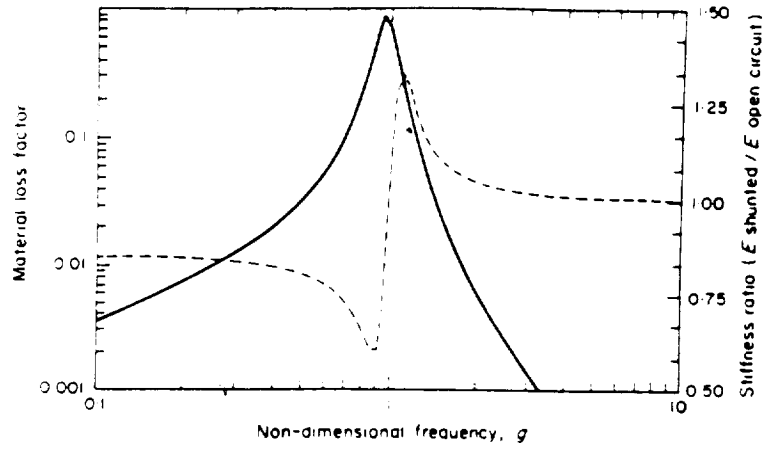

Figure 14. Effective material properties of piezoceramic shunted by a resonant LRC circuit (r = 0.20) in the transverse mode of operation (k_{33}=0.38) showing material loss factor (solid) and relative modulus (dash). Reference [4].

1.4.5. COUPLING SHUNTED PIEZOELECTRICS TO STRUCTURES

The peak loss factor of a vibration will decrease from that of the piezoelectric, when it is coupled to its host structure, according to the fraction of the total strain energy that is actually in the piezoelectric, reference [4]

$$\eta^{TOT} = \sum_{i=1}^{n} \eta_i U_i \Big/ \sum_{i=1}^{n} U_i, \tag{8}$$

where U_i is the strain energy in the ith element of the structure. The challenge is thus to employ the damping piezoelectric material in areas of high strain energy to take advantage of this weighting. Of course, the high strain energy locations must also be ranked by their influence on system performance objectives.

The strain energy sharing concept is first considered when designing the damper to be applied to the structure. Note that the word, damper, refers to the piezoelectric damping material and any necessary series or parallel stiffnesses that give the device structural integrity. All damping devices can be simplified to follow one of two different design procedures:

Case(1) If the damper is made up of 100% piezoelectric that is loaded in one direction the material properties in figure 12 apply. An example of this is a shear washer to be

$$\rho_i = R_i C_{pi}^S \omega = \sqrt{1 - k_{ij}^2} \tag{9}$$

Case(2) If the damper consists of a piezoelectric with series and/or parallel stiffnesses, the peak loss factor location can no longer be guided by equation (9). In this case, equation (9) is a good first iteration approximation if series stiffnesses are high and parallel stiffnesses are low compared to the piezoelectric. The short circuit stiffness, K_1 and the open circuit stiffness, $(K_1 + K_2)$ must be computed from an analytical or finite element model of the complete device. Assuming the component's effective material properties are analogous to the piezoelectric, a first order estimate of the effective coupling coefficient,

$$K_{ij}^2 = \left.\frac{K_{sc}}{K_{oc}}\right|_{component}, \tag{10}$$

is then used in (9) in place of k_{ij}^2 to size the resistor. An example of this is the flex-tensional device described in section 2.2.

Regardless of the design case, the short and open circuit stiffnesses of the damper determine two of the minimum three points necessary to describe the first-order stiffness curve of the damper (figure 15(a)). The third parameter, conveniently given by the transition frequency, ρ, is determined by the value of the shunting resistor.

1.4.6. FINITE ELEMENT MODELING OF PIEZOELECTRIC-BASED DAMPERS

In order to determine the performance of a given piezoelectric damping scheme in its host structure, the damper's stiffness and loss factor curves from figure 15(a) must be modeled. This behavior is captured by the following spring and dashpot finite element configuration (figure 15(b)).

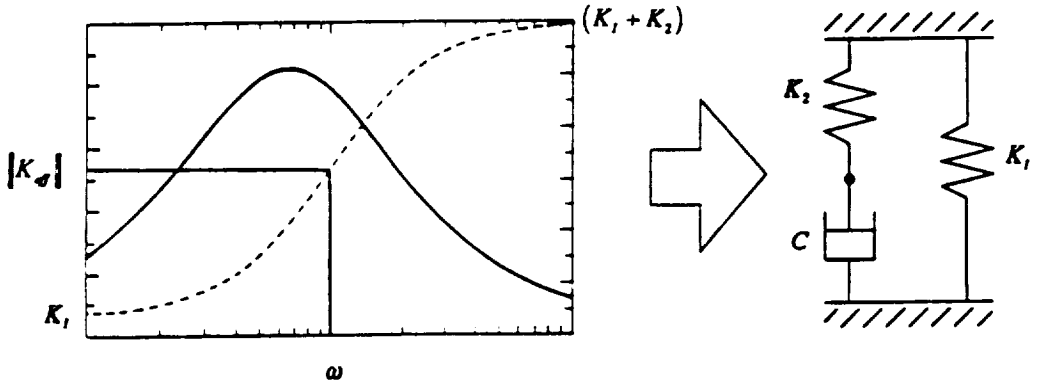

Figure 15. (a) Effective damper properties of a resistively shunted piezoelectric damper in the longitudinal case (k_{33}=0.75) showing damper loss factor (solid) and the damper's stiffness (dash). (b) Equivalent model of the piezoelectric-based damper.

The complex stiffness of the three element configuration is modeled with two linear spring stiffnesses, K_1, K_2 and one complex dashpot stiffness, $Ci\omega$ as follows:

$$Keff = K_1 + \left(\frac{1}{K_2} + \frac{1}{Ci\omega} \right)^{-1} \tag{11}$$

Given K_1 and K_2 from static structural models, C is the only unknown constant needed to complete the dynamic model. Simple algebraic manipulations yield the appropriate value of C such that the transition from low-frequency short-circuit stiffness to high-frequency open-circuit stiffness occurs at the correct transition frequency, ρ. This is accomplished by arbitrarily selecting a third coordinate point, (ω, $\|K_{eff}\|$), near the transition of the stiffness curve.

Figure 15 shows an equivalent mechanical model of the resistively-shunted piezoelectric damper (including series and parallel stiffnesses). This mechanical equivalent model is suitable for inclusion in commercial finite element software.

The real and imaginary parts of the complex stiffness are separated in (12) to calculate the real magnitude in (13):

$$Keff = \left(\frac{K_1 K_2^{\,2} + (C\omega)^2 (K_1 + K_2)}{K_2^2 + (C\omega)^2} \right) + i \left(\frac{C\omega K_2^2}{K_2^2 + (C\omega)^2} \right) \tag{12}$$

$$\|Keff\| = \sqrt{\left[\mathrm{Re}al(Keff) \right]^2 + \left[\mathrm{Im}ag(Keff) \right]^2} \tag{13}$$

The results of (12 & 13) are manipulated into the quadratic equation, $C^4\{a_1\} + C^2\{a_2\} + \{a_3\} = 0$ and solved for the only unknown, C.

$$C^4 \left\{ \omega^4 \left[(K_1 + K_2)^2 - (\|Keff\|)^2 \right] \right\} +$$

$$C^2 \left\{ \omega^2 \left[2K_1 K_2^2 (K_1 + K_2) + K_2^4 - 2(\|Keff\|)^2 K_2^2 \right] \right\} +$$

$$\left\{ K_2^4 \left(K_1^2 - (\|Keff\|)^2 \right) \right\} = 0 \tag{14}$$

This equivalent mechanical model is used in Chapter five to generate the simulated performance transfer functions of the piezoelectric-based component

CHAPTER 2

POTENTIAL PIEZOELECTRIC DAMPING IMPLEMENTATIONS FOR ASTREX

The general problem of damping a complicated space structure with piezoelectric materials is open-ended. In trusses consisting of repetitious truss bays the problem is to optimize strut placement, in order to maximize the percentage of strain energy in the damping elements. In structures, like ASTREX, which consists of tripod legs and a hexagonal-planar truss, the options are more numerous for placing various damping elements in various locations. There is freedom to use any device that has considerable influence in damping the modes that facilitate control rolloff.

The most obvious damping scheme, building struts for ASTREX, was not considered for the following two reasons: 1. It was determined in reference 2 that replacing ASTREX's primary composite struts with piezoelectric struts offers insignificant damping with only a few struts being switched. Obviously, if too many struts are replaced, the structure becomes too heavy. 2. Laminated piezoelectric/composite active struts made by TRW, which replaced the three tripod legs, have already been installed in the testbed. Prior to their installation, full-length piezoelectric-composite tripod struts of figure 16, would have been considered for manufacture. This implementation would replace a fraction of the tripod composite tubing with three equally spaced piezoelectric stacks (nine meters long, one inch diameter), such that the axial and bending stiffnesses were unaltered.

Two alternative damping schemes were considered. The "smart-node", active-joint or piezoelectric washer is addressed in section 2.1. The six-axis proof mass damper with

piezoelectric actuators is addressed in section 2.2. These devices are ranked in section 2.3 according to their loss factor potential.

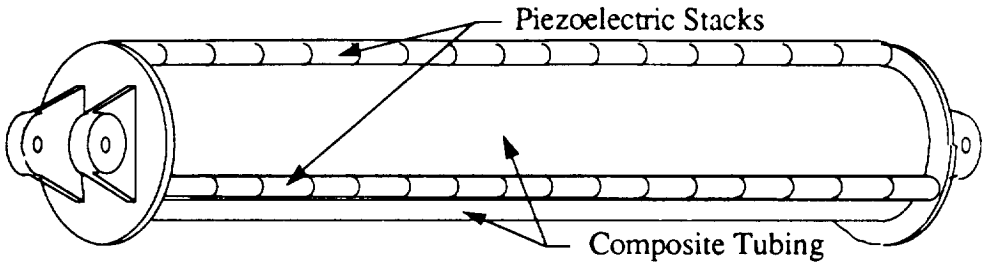

Figure 16. Proposed Piezoelectric-composite tripod strut with three equally spaced piezoelectric stacks (three meter version). Tripod length is nine meters.

2.1. POTENTIAL DAMPING DEVICE: SMART JOINT

An inexpensive and lightweight alternative to building full-length piezoelectric tripod struts is the tripod rotational damper, or "smart joint". The objective of this device is to damp the first two or three bending modes of the tripod fixture. Previous analysis in reference [18], has determined that the low-frequency tripod bending modes are critical to the line-of-sight performance. Therefore, the design issues of having a rotational damping mechanism at each of the three tripod-to-backplane mounts was investigated.

Damping rotational motion can be accomplished with piezoelectric washers, sleeves or equivalent struts. Each of these designs will be assessed later. First, it is necessary to determine the rotational stiffness, K_{rot} in figure 17, that leads to maximum strain energy in the rotary spring, for the first and second bending modes (that occur at roughly 20 and 60Hz). Recall that a peak damping target frequency near 40Hz was selected to best enable feedback control.

The quickest way to find the optimal stiffness of the rotational damper, is to use the assumed modes method on a simple model of the essential deformation in ASTREX at low frequencies; namely the spring-mass-tripod leg model of figure 17.

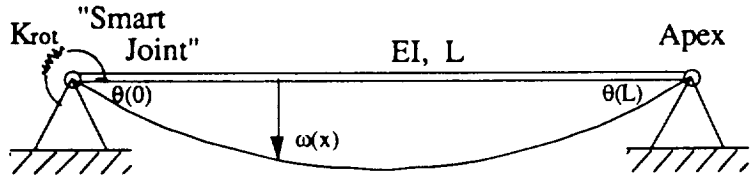

Figure 17. Tripod bending: The essential low frequency ASTREX dynamics.

Calculating the piezoelectric strain energy fraction with an assumed first-bending mode shape for the tripod leg, $\omega(x) = \sin(\pi x/L)$, yields:

$$U_{beam} = \frac{1}{2}\int_0^L EI\frac{\partial^2\omega(x)}{\partial x^2}dx = \frac{1}{4}EI\left(\frac{\pi}{L}\right)^4 L. \tag{15}$$

$$U_{rot} = \frac{1}{2}K_{rot}(\theta(0))^2 = \frac{1}{2}K_{rot}\left(\frac{\pi}{L}\right)^2 \tag{16}$$

$$\frac{U_{rot}}{U_{total}} = \left(1 + \frac{EI\pi^2}{2LK_{rot}}\right)^{-1}, \tag{17}$$

The variables, U_{rot}, U_{beam} and U_{total} are the strain energies of the rotary damper, the tripod leg and their sum, respectively. For example, when the strain-energy fraction is ten percent (typical value from other ASTREX analyses), an initial estimate for the rotational stiffness is: $K_{rot} \approx 0.5EI/L$.

A less quick, but more accurate method is to use the dynamic finite element model shown in figure 18. The goal is to maximize the piezoelectric strain energy in the first or second bending modes. This can be evaluated using the ratio:

$$\frac{U_{piezo}}{U_{total}} = \frac{(\Phi_i^T)_{piezo}K_{piezo}(\Phi_i)_{piezo}}{\Phi_i^T[K]\Phi_i} \tag{18}$$

Since the piezoelectric's rotary stiffness is in series with its deformable channel interface with the backplane truss (see figure 2), the modal displacements of the rotary damper must be scaled by the ratio of piezoelectric flexibility to total rotary flexibility, α.

$$(\Phi_i)_{piezo} = \alpha(\Phi_i)_{rot}; \quad \alpha = \left(\frac{K_{channel}}{K_{channel} + K_{piezo}}\right)$$

where,
$$K_{rot} = \left(\frac{1}{K_{piezo}} + \frac{1}{K_{channel}}\right)^{-1}. \tag{19}$$

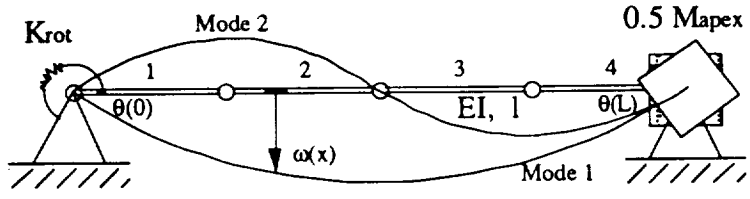

Figure 18. Finite element modeling of tripod bending

The optimal stiffness value of 400kNm agrees with the optimal value obtained by iterating the stiffness in the full-scale ASTREX finite element model until the piezoelectric strain energy peaks near 40Hz (the mean frequency between the first two bending modes). This indicates that it is safe to assume that most of the total strain energy at low frequencies is in the tripod legs, not the backplane truss. NASTRAN also indicates that the piezoelectric absorbs 10% of the total strain energy (4.2% modeled loss factor) for a typical tripod bending mode at 29Hz. The optimal stiffness can now be used to design and assess three different rotational dampers: the washer, the sleeve, and the equivalent strut.

2.1.1. PIEZOELECTRIC WASHER DESIGN

The washer design consists of piezoelectric material that is strained in shear under dynamic loading. As the tripod leg bends it exerts a reaction torque at the tripod mount, which behaves as a fixed boundary condition. Inserting piezoelectric washers between the ears of the tripod strut and the clamps of the mount, transforms the rigid boundary condition into a rotary spring as seen in figure 19.

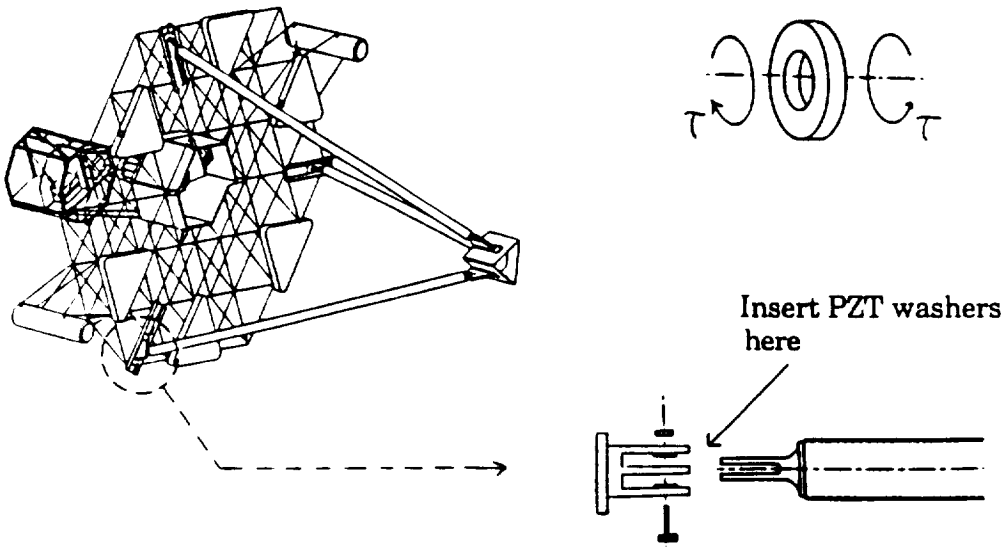

Figure 19. Piezoelectric "washer" design for tripod strut joints. Two washers per strut are each loaded in the shear mode.

Using the optimal stiffness in the shear stiffness equation (6), a washer with a one inch outer diameter with a half-inch hole and one-eighth inch thickness is calculated.

$$K_p = 400kNm = \frac{GJ}{t} = \frac{G}{t}\left(\frac{\pi}{32}\left(d_{out}^4 - d_{in}^4\right)\right), \tag{20}$$

where J is the polar moment of inertia of a disk and the shear modulus is, $G = 26GPa$ for Ch-5400 piezoelectric material (short-circuit).

After the washer's size was determined acceptable, the feasibility of shunting circuits for the piezoelectric dimensions must also be determined. Sizing the inductor, L, and resistor, R, for resonant circuit shunting according to the formulations described in chapter 1, yields: L = 15kH and R = 1000kΩ. For resistive shunting, a resistor, R = 1490kΩ, is ideal. Both of these resistors are accessible. The inductors, however, would be heavier and larger than the actual testbed itself, unless an active inductor scheme described in chapter one was used. Despite the feasibility of the resonant circuit, the broadband damping of resistive shunting was used for the sake of controller gain stabilization.

2.1.2. PIEZOELECTRIC WASHER MANUFACTURING ISSUES

Once the washer's dimensions and shunting network has been sized and determined feasible, the piezoelectric poling issues must be addressed. Manufacturing the washers would involve inventing a feasible means to accomplish circumferencial poling of a disk. Two methods were investigated: magnetic field poling and continuous sweep poling.

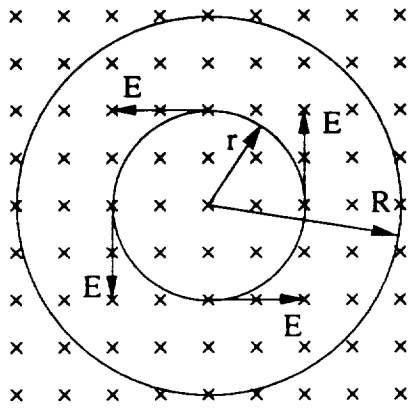

Figure 20. Circumferencial poling technique using a rapid change in magnetic field to produce a circumferencial electric field, E. The magnetic field, B, is denoted by "x's" and oriented out of the plane of the page.

The feasibility of magnetic field poling, shown schematically in figure 20, was evaluated with the electromagnetic relation in equation (21). Equation (20) states that the line integral of the electric field is equal to the change in magnetic flux within that integral path, $\Phi_B = B\pi r^2$.

$$\oint E \cdot d\ell = -\frac{\partial \Phi_B}{\partial t} \tag{21}$$

For r < R, and a required polarization voltage of 38kV/cm, the required magnetic field rate of 3000 gigagauss/s is too high to create even with an instantaneous step input.

$$\left|\frac{\partial B}{\partial t}\right|_{req'd} = \frac{2}{r} E_{req'd} = 3000 \frac{gigagauss}{s} \tag{22}$$

An alternative poling scheme is a continuous circumferencial poling scheme adapted from reference [12]. This poling technique rotates the washers slowly through two flexible surface electrode pairs maintained at the required potential difference (figure 21). As the electrodes sweep the sides of the washer, the piezoelectric gets poled a full revolution in one hour: a rate sufficient to pole the piezoelectric material. This rate, ω= 6deg/minute was adapted from the experimental recommendations in reference [12]. The flux field described by equation (23) reference [12], decreases in intensity as the distance into the piezoelectric, r, is increased.

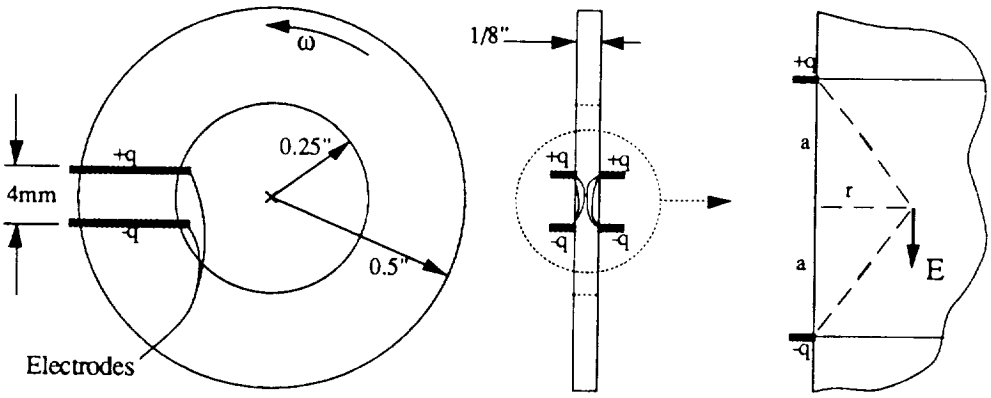

Figure 21. Continuous circumferencial poling of the washer.

$$E(x) = E_{applied} \frac{a^3}{\left(a^2 + r^2\right)^{1.5}} \tag{23}$$

From equation 23, the poling voltage across the electrodes must be applied to both sides of the piezoelectric in order to generate the same voltage in the center of the one-eighth inch thick washer. The applied poling voltage of 40kV/cm can be increased with electrode separation until the electrodes are separated by a 4mm gap. If the gap is increased still further, the required applied voltage can no longer be generated with a 10kV power supply (reference [12]). Figure 22 shows that the total electric field remains relatively constant if the electrode pairs are placed symmetric about the piezoelectric. This poling procedure would require the development of a circumferential poling machine. Such a task is out of the scope for this project.

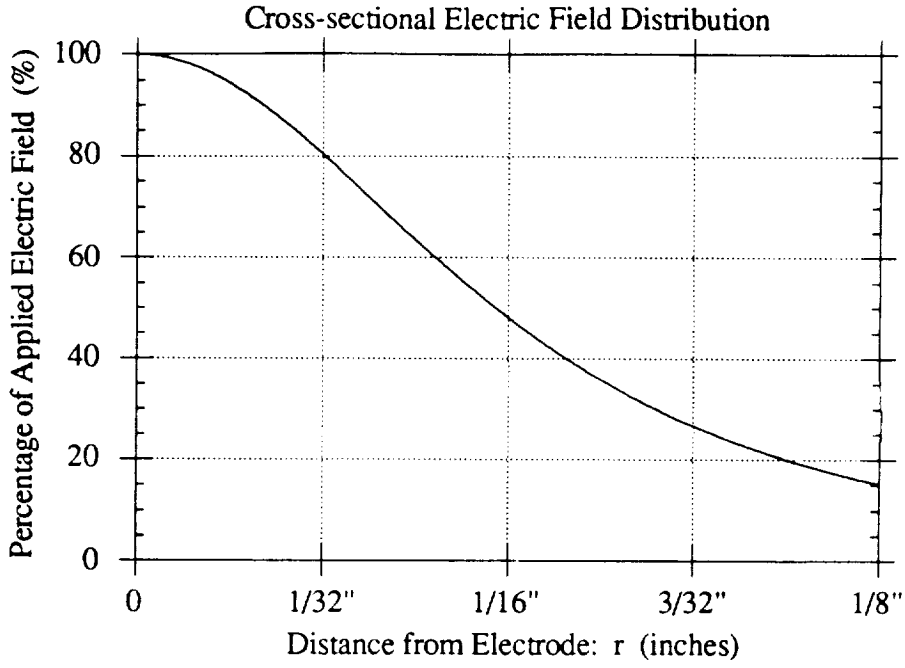

Figure 22. Continuous washer poling electric field distribution.

2.1.3. PIEZOELECTRIC WASHER STRESS ANALYSIS

Static and dynamic stresses were computed from NASTRAN finite element program and then used to evaluate the washer's load capability. Static stresses were computed from a NASTRAN model of ASTREX in its 30 degree position. Static stresses of 5.9MPa were calculated. This stress was conservatively assumed to be taken by the washers, not the tripod bolt that actually takes the load of the attached tripod structure. Torquer input to piezoelectric displacement transfer function output over the first 100Hz was calculated and scaled by the reaction wheel's maximum apex torque of 37Nm, to find the maximum dynamic stresses. The maximum dynamic stress in the piezoelectric washer is:

$$\tau_{max} = \frac{G\theta_{max}r}{t} = 104MPa, \tag{24}$$

where the shear modulus is, $G = 26GPa$, the maximum rotary displacement is, $\theta_{max} = 1000\mu radians$, the outer radius is, $r = 1/2inch$, and the thickness is, $t = 1/8inch$.

In order to maintain a factor of safety near three times brittle fracture, and avoid permanent depolarization in the piezoelectric, the piezoelectric design stress limit of 50MPa

was enforced. The 50MPa limit also ensures that the loss factor does not taper off at high stresses as seen in figure 23.

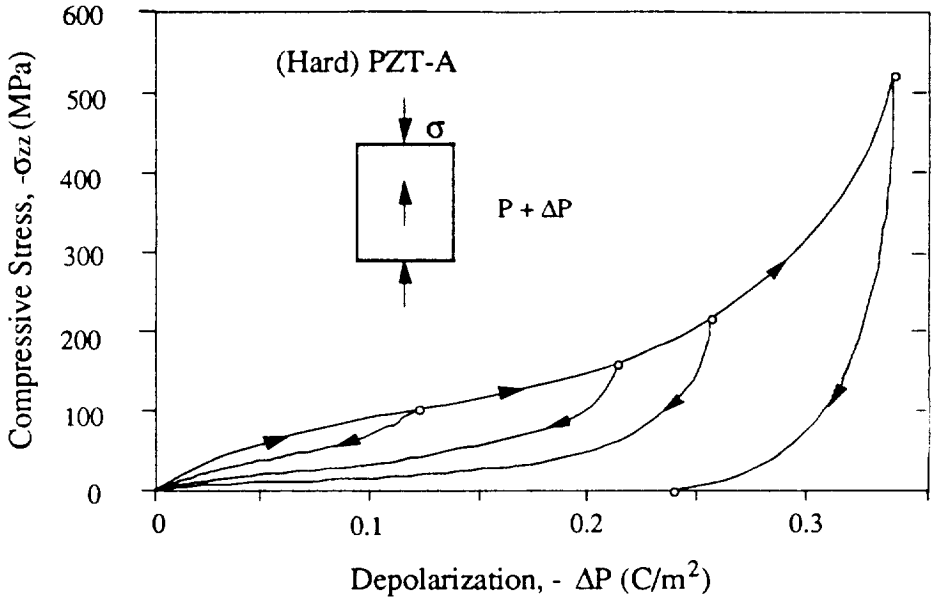

Figure 23. Percent depolarization versus applied stress in MPa for PZT Ch-5400. Note the permanent depolarization hysterisis loop.

For the washer, unlike the six-axis tuned-mass damper in section 2.2, there is no practical way to provide a mechanical stop to prevent excessive rotary motion directly. Instead a rigid mechanical stop would be required to impact with the tripod's 0.3mm displacement at a 1foot distance from the pivot point. In short, the mass penalty of the mechanical stop would be larger than the damping mechanism itself. When modes skew to the plane of the washer are considered, the non-planar tensile stresses in the piezoelectric must also be constrained. This would demand even more bulk from the prospective mechanical stop in order to constrain the tripod in three dimensions.

In conclusion, the inelegance of the mechanical stop and the overwhelming labor involved in circumferential poling, discontinued the piezoelectric washer design.

2.1.4. ALTERNATIVE "SMART JOINT" DESIGNS

This section will briefly assess two alternative "smart joint" designs that have equivalent dynamic properties as the piezoelectric washer, but different manufacturing problems. The preliminary assessment has indicated that the piezoelectric sleeve of figure 24 and the equivalent piezoelectric strut of figure 25 are difficult to manufacture.

The sleeve design in figure 24 is similar to the washer in that both designs use circumferentially poled cylinders or disks as the damping element. The sleeve, however, is sheared against the tripod's axel and through the radius of the cylinder, whereas the washer is sheared through the thickness of the disk. Also, the sleeve's electrodes are placed on the inside and outside cylindrical surfaces, as opposed to both sides of the disk.

Sizing the component according to elasticity equation for a thick-walled cylinder derived in reference [19],

$$K_\theta = 400kNm = 4\pi GL\left(\frac{r_{out}^2 r_{in}^2}{r_{out}^2 - r_{in}^2}\right), \tag{25}$$

yields the following sleeve dimensions: $r_{in} = 0.25"$, $r_{out} = 0.5"$, and $L = 0.9"$.

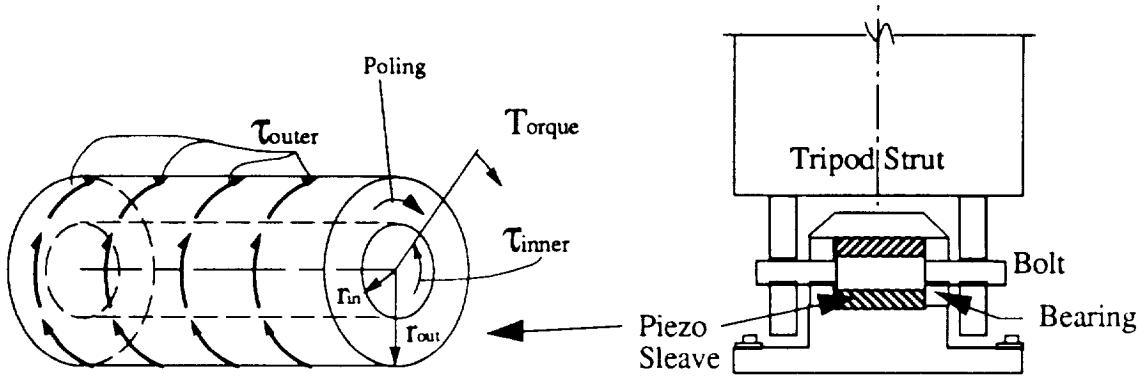

Figure 24. The sleeve is poled in the radial direction to exploit the shear mode of piezoelectric damping.

In addition to circumferential piezoelectric poling, the sleeve damper would also require a new tripod strut mount to accommodate the larger piezoelectric's length ($L = 0.9"$). With the washer design, the fixed boundary condition on both sides of the disk is ensured by preloading or tightening the bolt. The sleeve, however, has no preloading mechanism. Glue layers, that bond the inner surface to the tripod bolt and the outer surface to a modified tripod-end piece, would unfortunately absorb strain energy that could be used to actuate the piezoelectric. Shearing electrode surfaces could also present more difficulty over the easily accessible piezoelectric washers. Thus, the device was discontinued.

For a given washer or sleeve there exists an equivalent piezoelectric strut, orthogonal to the tripod strut, and separated from the tripod bolt by distance r. The strut's dimensions, A and L, and moment arm, r, are sized with the equivalent stiffness equation (26).

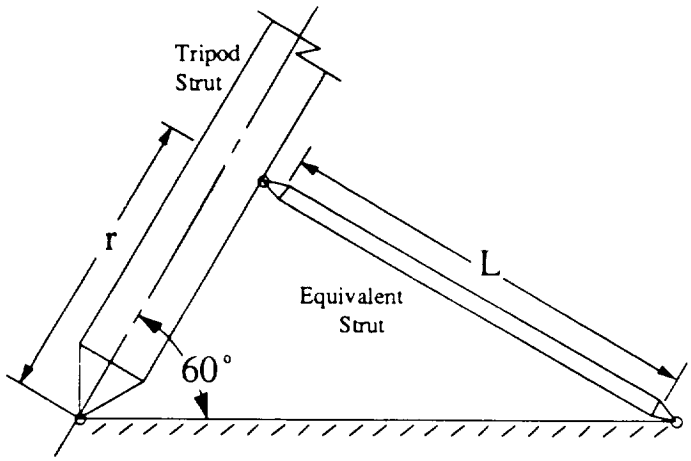

Figure 25. The equivalent piezoelectric strut.

$$\frac{GJ}{t} = \frac{EA}{L} r^2. \tag{26}$$

When the 400kNm stiffness is substituted into Equation (26) the optimal strut dimensions are: diameter = 0.5" and L = 5.2" for a moment arm r =3". Poling the device in the 3-3 direction is simplified by gluing wafers in series to form a stack with minimal electric field flux loss. The buckling loads on such a slender strut would require the design of high bending stiffness reinforcement with negligible axial contribution.

2.2. POTENTIAL DAMPING DEVICE: SIX-AXIS VIBRATION ABSORBER

The six-axis proof mass vibration absorber with six piezoelectric dampers was born out of the need to create an energy sink for the heavy (90kg) apex mass undergoing large displacements. Displacements over 4 times those found in the back plane, have been determined from ASTREX's eigenvectors. Preliminary finite element analysis of the six-axis stewart platform configuration indicated that an effective damper stiffness of 1.5N/um would channel over 50% of the total strain energy in the piezoelectric material for several modes under 50Hz. Theoretically, this means that modal loss factors as high as 20% are attainable. Mode shapes and loss factors that are representative of their corresponding frequency region, are shown in figure 27 in the next section.

The six-axis proof mass damper design in figure 26 consists of an already existing 90kg. balancing mass suspended from the interior of the 24"x24"x24" triangular apex housing by six flex-tensional damping devices. It should be noted that the 90kg. mass primary purpose is to balance the ASTREX testbed on its air bearing ball joint. The ball joint is connected to the center of the hexagonal primary truss which is elevated above the floor by a twenty foot supporting post.

The Stewart bridge configuration yields the maximum stroke capability available to the six axis damper design. This optimal stroke/actuation configuration was slightly modified to accommodate the geometrical constraints of the congested apex interior. (see figure 26) If the distance, d, between adjacent struts in each of the three orthogonal strut pairs is decreased, the rotational eigenvalues of the proof mass decrease due to the decrease in the system's effective moment arm. This yields a more effective damper for the low frequency rotary movements. The tradeoff is the increase in static stresses of the dampers due to gravity loads. The distance versus stress optimization for the modified Stewart bridge was not investigated, since the dimensions of the damping device prevented the aforementioned distance reduction.

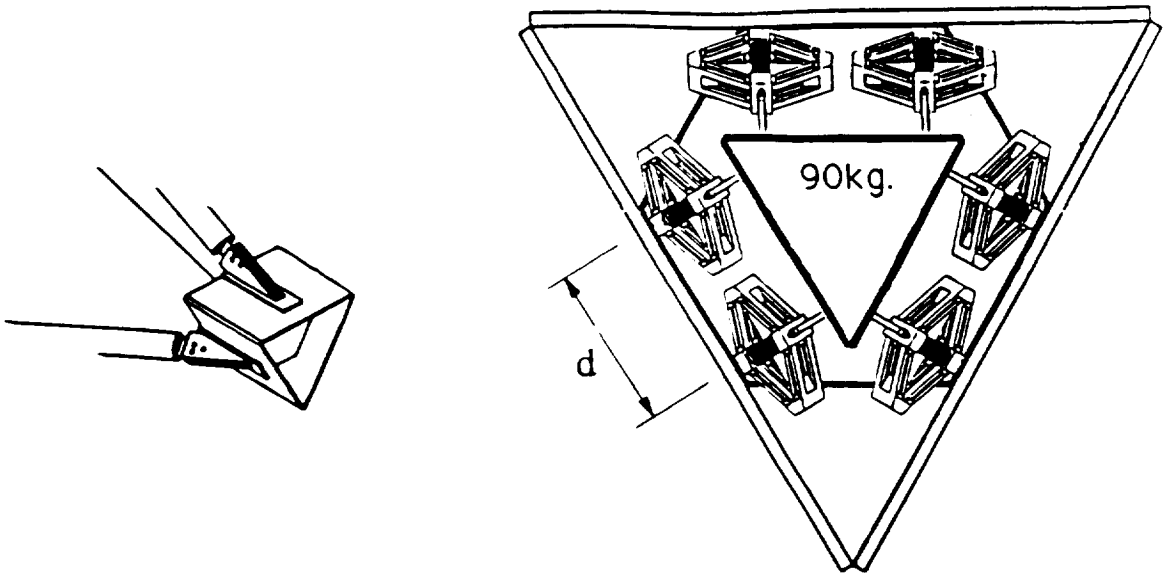

Figure 26. (a) Apex. (b) Six-axis vibration absorber with 90kg. proof mass attached to apex housing interior by 6 piezoelectric-based damper/actuators.

The applied static and dynamic component forces need to be determined before the actual piezoelectric and component properties can be determined. The total force will be used in chapter 3 to calculate component stresses. The static forces applied to each component are each dependent on the orientation of ASTREX. For this application it is important to design each component for the maximum force induced by static gravity loads and dynamic operating loads. In order to accomplish this and keep the piezoelectric in compression under dynamic loads, preload stresses in excess of the 50MPa design limit are required. In the laboratory, however, each of six actuators can be preloaded separately according to the total static and dynamic applied force. If too much preload is used the

piezoelectric may depole. If too little preload is used, the piezoelectric may fail as soon as the device flexes in tension as in equation 27.

$$0 < \sigma_{piezo} \leq \sigma_{depolarization} = 50MPa \tag{27}$$

Multiplying the peak strut displacement on the torquer to strut transfer function by the maximum operating torque of 37.5Nm, yields the dynamic force in the six components of 275N. When ASTREX is in its 30 degree laboratory configuration, the six axis has the following static strut forces: The top two struts are in 900N tension, the lower strut pairs are in 600N compression. Maintaining an approximate 10% factor of safety for the loading, the top struts need to be designed with 1300N of tension (piezoelectric compression), and the lower strut pairs need to be designed with 1000N of compression (piezoelectric tension). The best device, as designed in chapter 3, will have adjustable tensile and compressive preload capability. For instance, the lower strut pairs will need compressed preload springs to avoid piezoelectric tension, while the top struts will need a preload spring in *tension* to avoid piezoelectric depolarization.

After the preliminary device design and piezoelectric size was determined acceptable, the feasibility of shunting circuits for the piezoelectric dimensions must also be determined. Sizing the inductor, L, and resistor, R, for resonant circuit shunting according to the formulations described in chapter 1, yields: L = 0.4kH, R = 700kΩ and C = 6.8pF (inherent piezoelectric capacitance). For resistive shunting, a resistor, R = 917kΩ, is ideal. Although the resistors are accessible, the inductors would weigh 300g, unless an active inductor scheme described in chapter one was used. Despite the feasibility of the resonant circuit, the broadband damping of resistive shunting was used for the sake of controller gain stabilization.

2.3. DAMPING PERFORMANCE: SMART JOINT VERSUS SIX-AXIS ABSORBER

In order to decide which damping scheme to attempt to build, the two designs were evaluated according to their ability to absorb strain energy from performance-sensitive modes. Recall equation (5), that states that the system loss factor is proportional to the fraction of the total strain energy in the piezoelectric for a given mode. Although only three modes are listed in figure 27, the trend of six-axis vibration absorber dominance is present in all modes. The potential merit of the six-axis absorber obviously exceeds that of the washer design. In the next chapter the design of the six-axis absorber and component is presented.

Mode #13	Mode #23	Mode #40
f = 29Hz	f = 42Hz	f = 77Hz
η_{6axis} =19.4%	η_{6axis} =7.2%	η_{6axis} =0.42%
$\eta_{washers}$ =4.2%	$\eta_{washers}$ =0.042%	$\eta_{washers}$ =0.008%

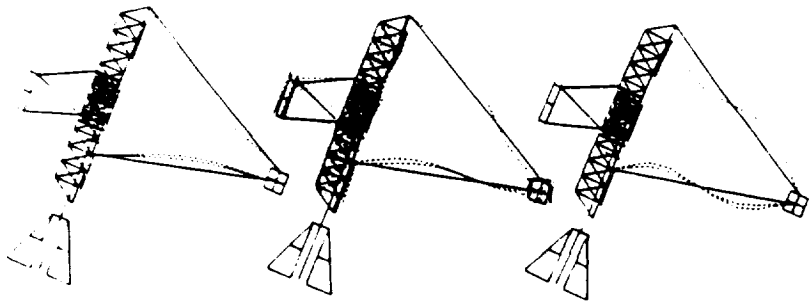

Figure 27. The washer and the six-axis vibration absorber design are compared.

CHAPTER 3

DESIGN AND ANALYSIS OF THE FLEX-TENSIONAL COMPONENT

The most critical part of six-axis proof mass damper design, described in chapter 2, is the component design of the six damping devices. The device design is complicated by the fact that piezoelectric material alone is too stiff and brittle to be used as a low-frequency damper. It is desirable to tune the vibration absorber to 30Hz. A 30Hz tuned vibration absorber will sag about 250micrometers in a one-gee field. This deflection implies a material strain for greater than the ceramic will allow. Thus, a properly designed stroke amplification device is essential in reducing the device's stiffness and increasing its travel.

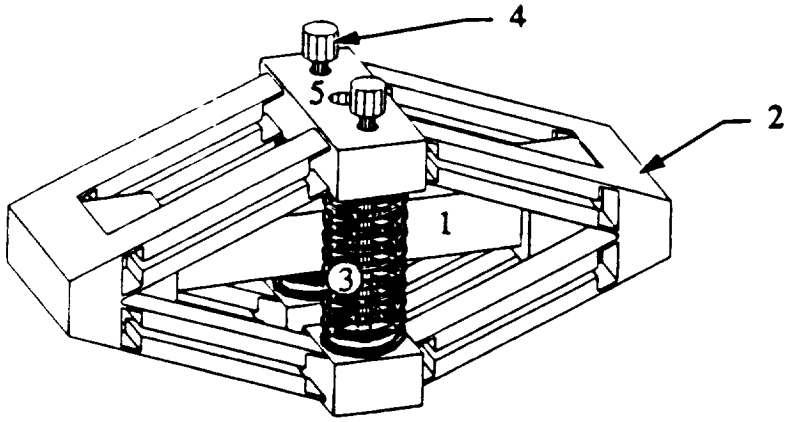

Figure 28. Illustration of the prototype flex-tensional piezoelectric stroke amplification device. Parts include: 1. One 16-layer piezoelectric stack with two steel shims. 2. One steel flex-tensional stroke amplifier. 3. Two preload springs. 4. Two threaded steel rods with adjustable mechanical stops. 5. Axial stinger.

3.1. DESIGN DETAILS OF THE FLEX-TENSIONAL DEVICE

The role of each of the five parts described in figure 28 and their associated design, manufacturing and assembly considerations will be assessed in the following five paragraphs:

Design Feature #1: The role of the piezoelectric stack is to provide resistively-shunted passive damping. The design uses mechanical amplification to reduce the stiffness of the stack in order to meet the 30Hz target eigen-frequency of the six-axis tuned mass damper. This, in turn, creates large critical stresses in the piezoelectric. Reducing the stack's stiffness may also be achieved by increasing its length and decreasing its cross-sectional area. This design is limited by a requirement that the material stresses are no greater than 50 MegaPascals (MPa). This requirement ensures minimal performance loss due to hysteretic depolarization. Buckling and shear failure must also be considered for slender stacks.

Another design consideration for the piezoelectric material is to have the appropriate number of capacitors (stacks) to balance the trade-off between glue-layer strain energy loss and large capacitor thickness fringing field loss. The glue layers between the 16 wafers act as springs in series with piezoelectric. A 16-wafer piezoelectric stack was the engineering judgment. The glue-layers gave the piezoelectric stack a longitudinal coupling-coefficient, k_{33}, of 0.59 as opposed to the nominal material value of 0.71. This reduces the available piezoelectric peak loss factor from 35% to 21% as given by equation (5), chapter 1.

Design Feature #2: The role of the steel flex-tensional stroke amplifier is to provide the necessary amplification to give the piezoelectric structural integrity and low stiffness. Stroke amplification in the device equates to a strain reduction in the piezoelectric. The ideal stroke amplifier would consist of beams with infinite axial stiffness connected by perfect hinges so that all the component's strain energy would be concentrated in the piezoelectric stack. This maximizes the peak component loss factor. A realistic component, however, has the following design criteria: 1. The lever angle is selected according to the analytical model, equation (49), so that the desired effective stiffness is realized. 2. The sum of the axial stiffness of the flexures is much greater than that of the stack. 3. The bending stiffness of the flexures is much less than that of the component. 4. The flexure stresses are less than their respective yield stresses. To meet these requirements, the stroke amplification device consists of a monolithic piece of steel, which is carved out of quenched and tempered 40 Rockwell steel by a machining process called: wire Electron Discharge Machining (wire-EDM).

Design Feature #3: The role of the two preload springs is to ensure that the piezoelectric stack remains in compression under normal loading conditions. This also

keeps the flexures in tension. The optimal design for the spring is a mile high spring with negligible stiffness. When such a combination is squeezed into the device, the preload requirement is met with negligible device stiffness contribution. Such a spring is limited by practical assembly procedures which require pronged pliers insertion to shorten the spring temporarily for insertion into the EDM'ed part. Spring coil spacing must be large enough to allow for a wrench adjustment of the mechanical stops.

Design Feature #4: The two mechanical stops are adjusted to prevent accidental overloading of the device. The maximum disturbance excitation of 28 ft.lbs. plus gravity load yields the component's maximum axial displacement of 0.3mm. Motion in excess of this number is inhibited. The mechanical stops are adjusted by wrench and locked in place with adjacent locknuts.

Design Feature #5: The role of the axial stinger is to suspend the 90kg. mass according to the modified Stewart bridge configuration. High axial stiffness and low bending stiffness of the stinger minimizes strain energy sharing. Low bending stiffnesses can be obtained by using a pinned flexure at each end of the stinger.

3.2. DEVICE ANALYSIS: ANALYTICAL TRUSS MODEL

Three different methods were investigated in designing the component. In this section, a simple truss analytical model is useful for preliminary design purposes. A NASTRAN finite element model, presented in 3.3.1, accounts for all stiffnesses. This model is upgraded in Section 3.3.2 to include the unmodeled flexibilities. In Section 3.3.3, the finite element model is used to optimize the component design.

3.2.1. KINEMATIC DERIVATION OF EFFECTIVE STIFFNESS

If it is assumed that the bending effects contribute negligible stiffness, the effective stiffness of the mount is easily determined through simple kinematics employing linearization for small displacements. Referring to figure 30, the vertical and horizontal displacements of each element are related as

$$\delta_v = 2L_a \sin(\theta) - 2(L_a - \delta_a)\sin(\theta - \delta\theta) \tag{28}$$

$$L_h + \delta_h = (L_a - \delta_a)\cos(\theta - \delta\theta), \tag{29}$$

where the kinematic constraint ensures that the elements remain connected during displacement.

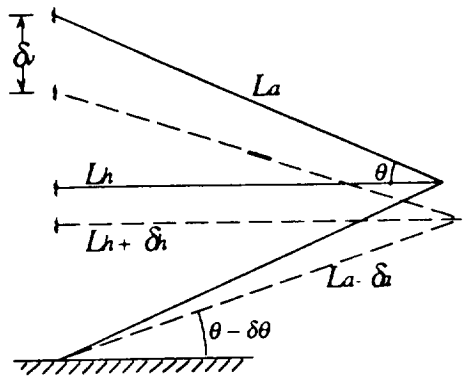

Figure 30. Schematic diagram showing mount in deflected and undeflected conditions.

Expanding the sinusoidal terms in (28) and (29) yields:

$$\delta_v = 2L_a \sin(\theta) - 2(L_a - \delta_a)(\sin\theta\cos\delta\theta - \cos\theta\sin\delta\theta) \tag{30}$$

$$L_h + \delta_h = (L_a - \delta_a)(\cos\theta\cos\delta\theta + \sin\theta\sin\delta\theta). \tag{31}$$

Linearizing (30) and (31), assuming $\sin\delta \cong \delta$ and $\cos\delta \cong 1$, and neglecting terms in δ^2, yields

$$\delta_v = 2L_a \sin\theta - 2L_a \sin\theta + 2L_a \cos\theta\delta\theta + 2\delta_a \sin\theta \tag{32}$$

$$L_h + \delta_h = L_a \cos\theta + L_a \sin\theta\delta\theta - \delta_a \cos\theta \tag{33}$$

Canceling terms and substituting $L_h = L_a \cos\theta$, yields

$$\delta_v = 2L_a \cos\theta\delta\theta + 2\delta_a \sin\theta \tag{34}$$

$$\delta_h = L_a \sin\theta\delta\theta - \delta_a \cos\theta \tag{35}$$

Dividing (35) by $0.5\tan\theta$ yields:

$$2L_a \cos\theta\delta\theta = \frac{2\delta_h}{\tan\theta} + \frac{2\delta_a \cos^2\theta}{\sin\theta} \tag{36}$$

which is then substituted into equation (34) and simplified with $\sin^2\theta + \cos^2\theta = 1$ to yield:

$$\delta_v = 2\left(\frac{\delta_h}{\tan\theta} + \frac{\delta_a}{\sin\theta}\right) \tag{37}$$

For a force F applied at the top of the device, the load transmitted in each lever arm is $F/2\sin\theta$, and that borne by the piezoelectric stack is $F/\tan\theta$. The respective stiffnesses of the piezoelectric stack and the lever arms being

$$K_{stack} = F_{stack}/\delta_{stack} = F/\tan\theta\,\delta_{stack} \tag{38}$$

$$K_a = F/2\sin\theta\,\delta_a \tag{39}$$

Substituting $\delta_h = 0.5\delta_{stack}$ into (38), and substituting (38) and (39) into (37) yields the effective stiffness of the device

$$K_{eff} = \left\{ \frac{1}{(K_{stack}\tan^2\theta)} + \frac{1}{(K_a\sin^2\theta)} \right\}^{-1} \tag{40}$$

The relation in equation (40) allows for the desired effective stiffness to be determined by the appropriate choice of lever angle, and piezoelectric and lever arm stiffnesses.

3.2.2. TRUSS MODEL DESIGN OF THE COMPONENT

Before equation (40) can be used to design the component, the stack and lever arm stiffnesses must be defined in terms of their material properties as opposed to the relations in equation (47) and (48). An expression for the bending stiffness of the flexures must also be defined, in order to ensure that the axial to bending stiffness ratio of the lever arms is large enough to channel strain energy into the piezoelectric. Additionally, this stiffness ratio must be sufficiently large in order for the negligible bending stiffness assumption of equation (40) to be valid. The previously mentioned stiffnesses needed in the design are given as follows:

1. *Piezoelectric Stack Stiffness:* The piezoelectric stack is made up of 16 piezoelectric elements glued together. The result is that the effective stiffness of the stack is reduced by the glue layers, thus

$$K_{stack} = \left\{ \frac{1}{K_p} + \frac{1}{K_{glue}} \right\}^{-1} \tag{41}$$

with K_{glue} determined through knowledge of the electromechanical coupling coefficient of the stack, and the piezoelectric stiffness. For the stack used, the measured short circuit stiffness is $K^{sc}_{stack} = 65\,MN/m$ and the calculated stiffness is $K^{sc}_{p} = 91\,MN/m$. The difference between these values is the attributed to the glue layer flexibility found in equation (13). The glue layer stiffness is determined as $K_{glue} = 203\,MN/m$ (15 glue layers in a 16 wafer piezoelectric stack).

2. *Lever Arm Stiffness:* The device is modeled with four arms, each of which comprises four "dogbone" flexure elements. The effective arm stiffness is written as

$$K_a = \frac{Eb}{\left\{ L_f/2t_f + L_{srb}/4t_{srb} \right\}} \tag{42}$$

where L_f, L_{srb}, t_f, and t_{srb} are the flexure and semirigid beam lengths and thicknesses, respectively. The lever arm width is constant: $b = b_f = b_{srb}$.

3. *Bending Stiffness:* Bending in the device is taken up in the flexures of each arm. In order to determine the total bending flexibility of the component, it is convenient to first determine the stiffness of one of the 32 flexure/half beam elements illustrated in figure 31. If the beam is assumed rigid, the non-negligible flexibility of the beam is due to its rigid body rotation seen in the component's deformed shape.

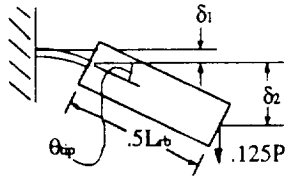

$$\delta_1 = \frac{(.125P)L_f^3}{3EI_f}, \quad \theta_{sp} = \frac{(.125P)L_f^2}{2EI_f}, \quad \delta_2 = 0.5L_{srb}(\theta_{sp})$$

Figure 31. Flexure and half rigid beam deflections.

The stiffness of a single flexure/half beam can be determined from $K_{1/32} = .125P/(\delta_1 + \delta_2)$. The $K_{1/32}$ bending stiffness is half the single lever arm stiffness (two flexures and one rigid beam). Since their are eight lever arms in series with eight adjacent lever arms, the lever arm is four times as flexible as the component bending stiffness. Thus, the effective bending stiffness of the component:

$$K_{bend} = 2K_{1/32} = \frac{P}{4(\delta_1 + \delta_2)} = \frac{Eb_f t_f^3}{\left(2L_{f_{true}}^3 + 1.5L_{srb}L_{f_{true}}^2\right)} \tag{43}$$

The bending stiffness acts in parallel with the effective truss model stiffness as follows:

$$K_{eff} = \left\{\frac{1}{(K_{truss}\tan^2\theta)} + \frac{1}{(K_x \sin^2\theta)}\right\}^{-1} + K_{bend}. \tag{44}$$

However, the truss model assumption in equation (53) is violated if K_{bend} is nonzero. This is not possible. Therefore, the design approach is to enforce the component's effective stiffness, K_{eff}, to be "n" times as stiff as the effective bending stiffness K_{bend}:

$$K_{bend} = K_{eff}/n, \tag{45}$$

where "n" is a large number (n = 9 for the original design).

The fraction of strain energy in the piezoelectric is derived by substituting δ_p, δ_{ff} and K_{ff} into the strain energy equation:

$$\frac{U_p}{U_{total}} = \frac{K_p}{K_{ff}}\left(\frac{\delta_p}{\delta_{ff}}\right)^2 = \frac{K_{ff}}{K_p \tan^2\theta} = \left(1 + \frac{K_p}{K_a \cos^2\theta}\right)^{-1} \tag{46}$$

where, $$\delta_p = \frac{P}{K_p \tan\theta} \text{ and } \delta_{ff} = \frac{P}{K_{ff}}. \tag{47}$$

Equation (55) means that it is ideal to have the axial stiffness of the lever arm, K_a, to be much larger than the axial stiffness of the piezoelectric stack, K_p: Therefore, the design approach is to enforce $K_a = RK_p$, where "R" is a large number (R = 3.5 for the original design).

The applied force is magnified in the piezoelectric by the lever ratio: $\tan^{-1}\theta$. The force in the flexures is magnified by a similar $\sin^{-1}\theta$ factor. Thus, the stresses in the piezoelectric and flexures are, respectively:

$$\sigma_p = \frac{P}{A_p \tan\theta}, \quad \sigma_f = \frac{P}{8A_f \sin\theta}. \tag{48}$$

The design approach is to enforce some of the parameters which are suited to the physical requirements of the implementation, and to determine the remaining parameters to give the desired stiffness properties. The following parameters are selected to satisfy the physical constraints of the congested apex interior (see section 3.5 for constraint details).

$$L_{arm} = 40mm, \quad b_f = b_{arm} = 10mm, \quad E = 200GPa, \quad t_{arm} = 4mm \tag{49}$$

Using design curves similar to those illustrated in section 3.4, the initial flexure dimensions were sized ($L_f = 5mm$, $t_f = 0.8mm$) to channel strain energy into the piezoelectric with negligible component bending stiffness (n=9).

This design predicts the following short and open-circuit component stiffnesses:

$$K_{ff}^{s} = 8.1N/\mu m; \quad K_{ff}^{oc} = 11.26N/\mu m \tag{50}$$

Through the procedures described in chapter 4, the following measured values were obtained:

$$K_{exp}^{s} = 9.57N/\mu m; \quad K_{exp}^{oc} = 10.66N/\mu m \tag{51}$$

The discrepancy between the truss model and the data is attributed to the unmodeled flexibilities and other factors that are discussed in chapter 4.

3.3. DEVICE ANALYSIS: NASTRAN FINITE ELEMENT MODEL

A finite element model of the component was constructed to generate insight into the important and negligible stiffness terms of the global stiffness matrix of the component. In this section and section 3.5 the finite element program, NASTRAN, is used for outputting bending and axial stresses and strain energies in the flexures to aid in an iterative design optimization of the flexures. In addition, the finite element method will be used as a basis for deriving a reduced order closed form analytical expression for the device properties which incorporate bending terms (see Appendix I).

If you can imagine the three orthogonal planes, x=0, y=0, and z=0, sharing a common origin at the device's centroid, the device becomes separated into eight equivalent quadrants The following is true for any of the eight identical quadrants: 1. The stinger is one-fourth the area and thus the component receives only one-fourth the total load. 2. The piezoelectric length is halved, and area is one-fourth the original. 3. Only one lever arm pair is needed for analysis.

By taking advantage of the component's three axes of symmetry, the analysis can be reduced to the solution of the one-eighth component model seen in figure 32. Unlike the truss model in the previous section, this model includes all bending stiffnesses and constrains θ at the two ends of the beam. This model also assumes that the large rectangular blocks at the foot of the flexures have negligible flexibility.

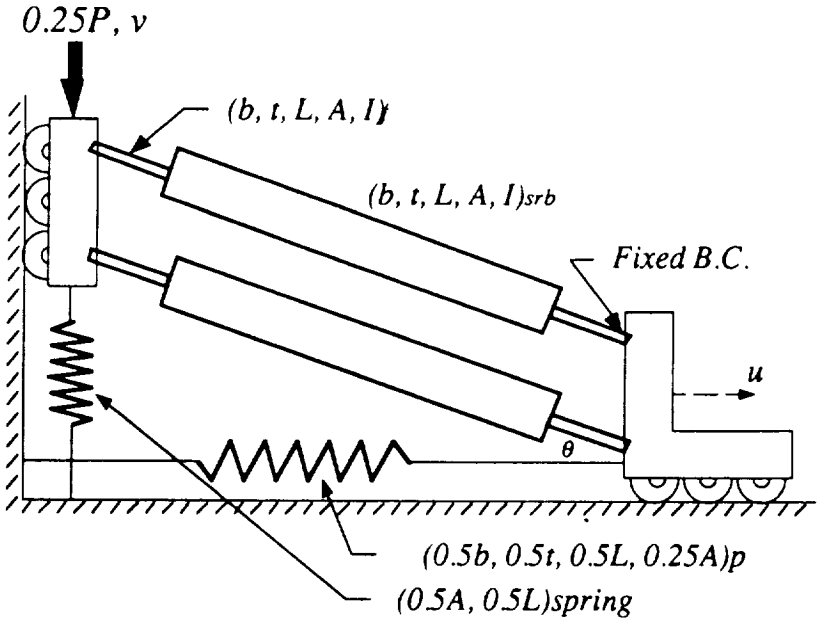

Figure 32. NASTRAN finite element component model includes all axial and bending stiffness associated with six-degree of freedom slender beam-elements.

Since the two parallel lever arms have identical displacement patterns under loading, an equivalent beam with doubled material properties is shown in figure 33. The spring's half area (two springs per component) and half length cancel to give the original spring stiffness. The piezoelectric's quarter area and half length equates to half the piezoelectric stiffness.

The model in figure 33 is now ready to build with two simple axial springs and three six-degree of freedom beam elements (one for the semirigid beam and two for the flexures), available from the NASTRAN finite element code. The boundary conditions are applied, and the assembled beams and spring model is constrained to move in the remaining u and v displacements depicted in figure 33. A quarter load is applied to the eighth model to generate deflection, stress and strain energy output for nodes and elements of interest.

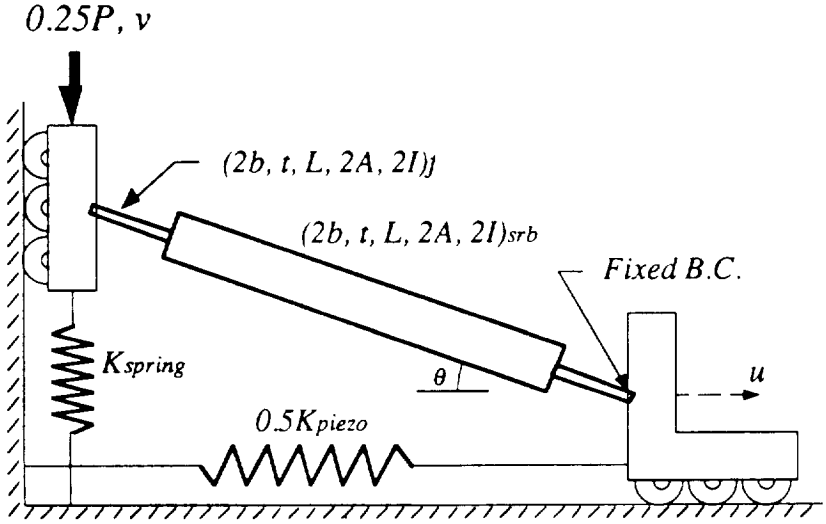

Figure 33. The one-eighth model with combined lever arm properties.

Multiple finite element analyses with minor parameter variations can be used to generate design curve data to replace the trial and error approach used with the simple truss model. The lever angle, θ, piezoelectric stiffness, K_p, and general lever arm dimensions are important to fulfilling the desired stiffness and physical constraints dictated by the structure to be damped. These properties are initially approximated with the truss model as a first design iteration. The influence of small flexure length and thickness variations on component performance, however, requires design curves derived from finite element software. The overall performance of the device is a measure of its ability to channel strain energy in the piezoelectric, maximize its flexure stress safety factor, and minimize the cyclic depolarization stress in the piezoelectric, while maintaining the desired component

stiffness. Representative component dimensions were selected to illustrate how the flexure dimensions are fine-tuned with the aid of design graphs. The selected component dimensions and properties are:

$$\theta = 10^{\circ};\ b = 2cm.;\ t_{\ast} = 1cm.;\ L_{\ast} = 4cm.;\ K_{\ast} = 91N/\mu m \qquad (52)$$

The four graphs in figures 34 through 37, plot the stiffness, $K_{\ast}$, the piezoelectric strain energy fraction, $U_{\ast}/U_{\ast}$, the piezoelectric stress, $\sigma_{\ast}$, and the flexure stress, $\sigma_{\ast}$, respectively, for various typical flexure dimensions.

All of the graphs are divided into two spaces by a vertical line at $t_{\ast} = 0.06cm.$ This vertical line separates the manufacturable space from the non-manufacturable space. The machining required to cut the steel part, Electron Discharge Machining (EDM), is a numerically controlled process with cutting tolerances of ±0.005inches (±0.0125cm.). Which means that a flexure thickness of 0.06cm (subjected to two cutting surfaces) could potentially be as small as 0.045cm or as large as 0.085cm for any of the component's 32 flexures. The machinist claims that these tolerances are conservative by an order of magnitude. Our experience with the finished product led to the engineering judgment of the minimum 0.06cm flexure thickness requirement.

The component stiffness graph in figure 34, is also divided into two more spaces by a horizontal line. This line separates unacceptable high-stiffness, high-frequency dampers from acceptable, low-frequency dampers by the $K_{\ast} = 3N/\mu m$ stiffness line. Although stiffnesses as high as this value generate significant damping in the 40 to 50Hz range, stiffnesses as low as $K_{\ast} = 1.5N/\mu m$ are optimal for providing significant damping near 30Hz. Thus, the design space for figure 34 is the lower-right quadrant. The graph depicts several trends. For a given flexure thickness, the longer flexure provides more of the desired flexibility. As the flexure thickness decreases from 0.06cm. to zero, the component stiffness decreases rapidly due to inefficient axial stiffness. As the flexure thickness increases from 0.06cm to 0.16cm and beyond, the stiffness increases exponentially due to excessive bending stiffness. The point of counterflexure in the stiffness curves is approximately where the peak strain energy occurs in figure 35.

Figure 35 illustrates that short flexures can channel more strain energy into the piezoelectric, than long flexures. For example, a flexure length of $L_{\ast} = 0.2cm.$ can push 92% of the strain energy into the piezoelectric, while a flexure length of $L_{\ast} = 0.6cm.$ can push 87% of the strain energy into the piezoelectric. The shorter flexure length unfortunately requires a flexure thickness too thin to manufacture. Another trend is that the larger flexure lengths have a broader range of flexure thicknesses to choose from that still

generate significant piezoelectric strain energy. The shorter flexure length plot $L_f = 0.2cm.$ is more narrow and less robust to flexure thickness perturbations and modelling errors.

For thin flexure thicknesses in Figure 36, all the applied force is channeled directly to the piezoelectric as expected for a component with negligible bending stiffness. As the flexure thickness approaches zero, the piezoelectric stress approaches the truss model prediction of 50.7MPa. As the flexure thickness increases, the bending stiffness of the shorter flexures increases rapidly, thereby preventing more of the applied force from reaching the piezoelectric stack. The horizontal line at 50MPa represents the upper limit of acceptable cyclic depolarization stresses for the piezoelectric. This stress also represents the beginning of partially non-reversible hysteretic depolarizations as described earlier in chapter 2. Thus, the design space of figure 36 is the lower-right quadrant.

The flexure stress graph in figure 37, indicates that low flexure thicknesses have unacceptably high axial stresses. As the flexure thickness increases, the flexure's cross-sectional area increases, and its axial stress decreases. As the flexure thickness approaches its optimal strain energy absorbing value, the flexure's moment of inertia and bending stresses become noticeable as the total stress increases. The more noticeable stress increase of the shorter flexure length ($L_f = 0.2cm.\ 0.04 \le t_f \le 0.1cm.$) is reason why the strain energy performance in figure 35 decreases at such a fast rate for that case. A careful look at the acceptable design space in the last three graphs, indicates that the $L_f = 0.2cm.$ design curve still has the highest strain energy performance with acceptably low effective stiffness and piezoelectric stress values. If a safety factor of 3 is applied to the yield stress of 600MPa for annealed and quenched steel, a design stress limit of 200MPa confines the design space in figure 37 to the lower right quadrant. Thus, figure 37 also illustrates the $L_f = 0.2cm.$ design option is still acceptable. However, if cyclic loading were considered, typical S/N plots for steel (reference [20]) indicate that all of these designs would potentially become at least partially plastic after 10^6 cycles. The lifespan of the design and the advantages and disadvantages of elastic-plastic flexures were unaddressed in this research. Instead a 150MPa design stress is enforced as a compromise between the risky and conservative safety factors of the yield stress and fatigue design criteria, respectively.

Given the previously described design considerations, two design alternatives can be extracted from the graphs. The high performance, decent robustness $L_f = 0.4cm.$ and $t_f = 0.06$ design option or the decent performance, high robustness $L_f = 0.6cm.$ and $0.06 \le t_f \le 0.08cm.$ design option are obvious design choices.

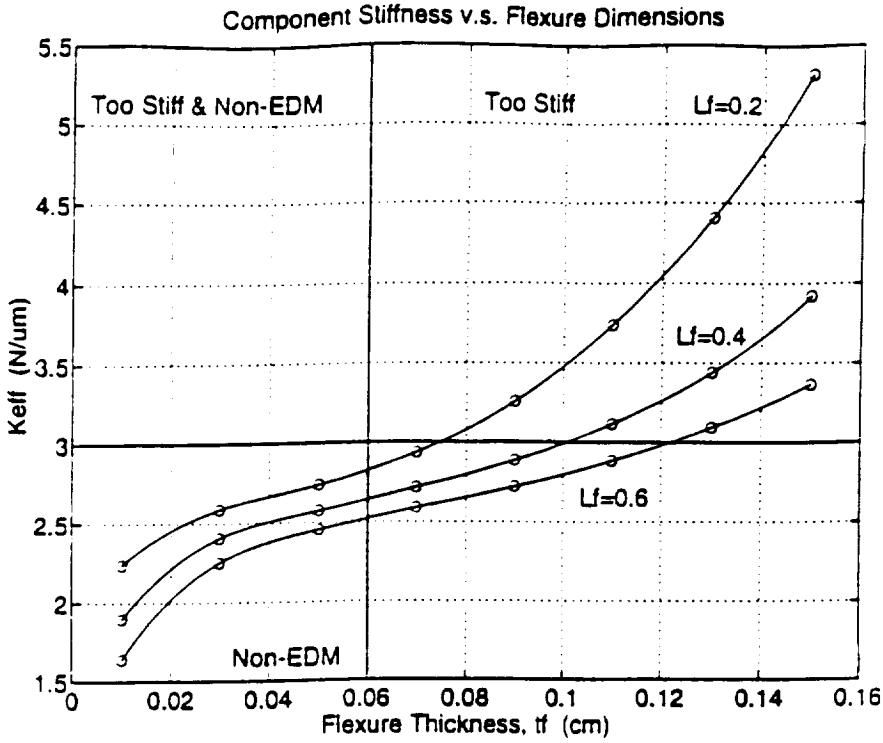

Figure 34. Component stiffness versus flexure dimensions, where $\theta = 10^{\circ}$, $b = 2cm.$, $t_{\infty} = 1cm.$, $L_{\infty} = 4cm.$, and $K_{\infty} = 91N/\mu m$ (Lf, is in cm.).

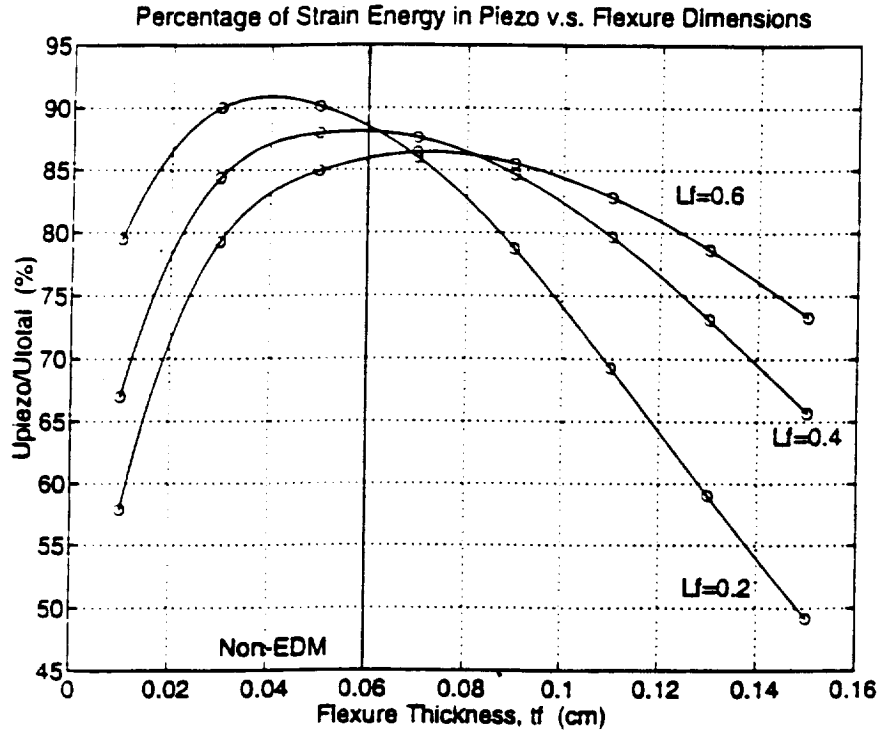

Figure 35. Piezoelectric strain energy versus flexure dimensions, where $\theta = 10^{\circ}$, $b = 2cm.$, $t_{\infty} = 1cm.$, $L_{\infty} = 4cm.$, and $K_{\infty} = 91N/\mu m$ (Lf, is in cm.).

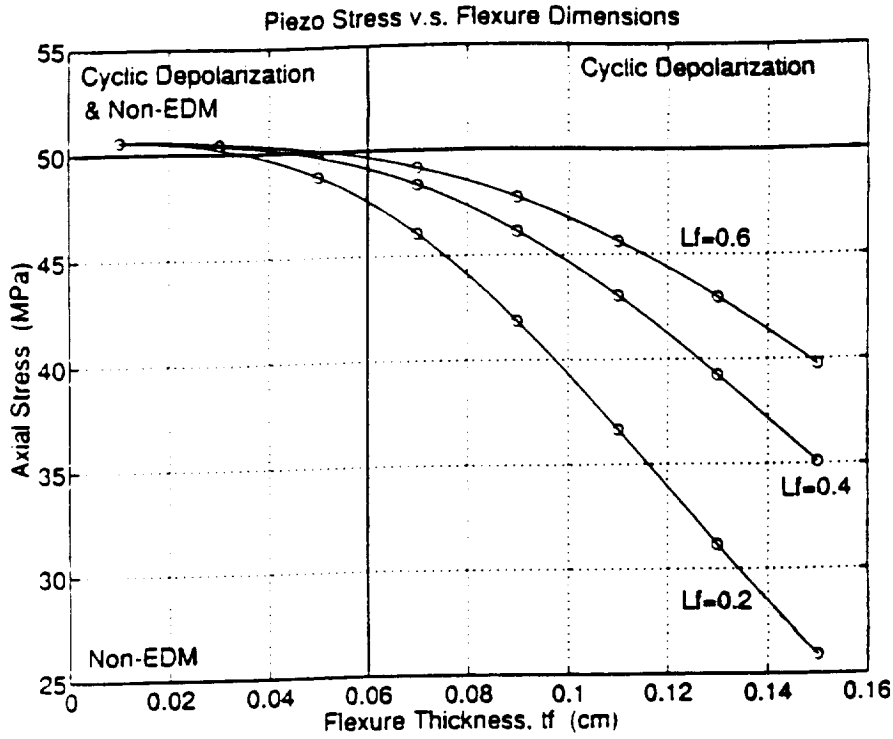

Figure 36. Piezoelectric stress versus flexure dimensions, where $\theta = 10^{\circ}$, $b = 2cm.$, $t_{ss} = 1cm.$, $L_{ss} = 4cm.$, and $K_p = 91N/\mu m$ (Lf, is in cm.).

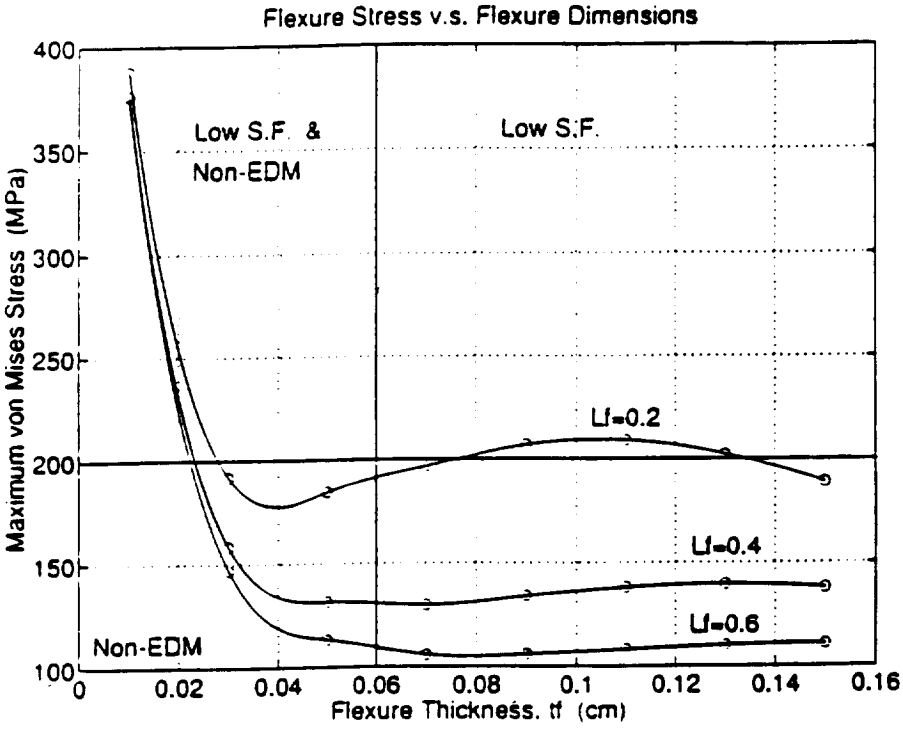

Figure 37. Flexure stress versus flexure dimensions, where $\theta = 10^{\circ}$, $b = 2cm.$, $t_{ss} = 1cm.$, $L_{ss} = 4cm.$, and $K_p = 91N/\mu m$ (Lf, is in cm.).

3.4. COMPARISON OF ANALYTICAL TRUSS AND NASTRAN MODELS

In this section the analytical truss component model is compared with the NASTRAN finite element model in order to gain insight into the errors associated with the flexure's negligible flexure bending stiffness assumption, and the rigid beam assumption of the truss model. The four graphs in figures 38 through 41, plot the stiffness, K_{eff}, the piezoelectric strain energy fraction, U_p / U_{tot}, the piezoelectric stress, σ_p, and the flexure stress, σ_f, respectively, versus the flexure thickness. Each plot compares the analytical and finite element solution for flexure length, $L_f = 0.4cm$. Otherwise, the piezoelectric and lever arm dimensions are identical to those selected in the previous section.

The finite element plot in figure 38 shows that the truss model is in relative agreement with the finite element model as the flexure thickness approaches zero and at mid-range thicknesses $0.07 \le t_f < 0.09cm.$ only. The effective stiffness and flexure stiffness simultaneously approaching zero is trivial. However, their similar high magnitude slopes both indicate that majority of the components stiffness is realized when a sufficient level of axial strength is reached. At low flexure thicknesses beyond this strength threshold, the finite element model is appropriately more flexible than the truss model, since the finite element model, unlike a truss, accounts for the bending flexibility of the "rigid beams". The finite element model is also appropriately more stiff at high flexure stiffnesses, since the bending stiffness of the relatively thick flexures (not included in the truss) contribute significantly to the component stiffness.

The percentage of piezoelectric strain energy is highly overestimated in figure 39, since the truss's deformed shape directs most of the component's deformation into piezoelectric deformation, instead of the flexibilities that are unmodeled by the rigid beam assumption.

As the flexure stiffness increases beyond $t_f = 0.08$, the truss model piezoelectric strain energy becomes increasingly overestimated since the piezoelectric deflection used in the formula for this plot is increasingly overestimated as flexure thickness increases. This piezoelectric deflection overestimation can be deduced from figure 40. Figure 40 shows that the truss model assumes 100% of the applied load to be transmitted into the piezoelectric via the lever angle. The corresponding finite element curve clearly indicates that the truss deformation assumption is less valid as the increasing bending stiffness inhibits load transfer to the piezoelectric.

The von Mises flexure stress is predominately an axial stress as modeled by the relatively close correspondence between the analytical and finite element curves of figure 41. This is less true for $t_f > 0.04cm.$, because bending stresses contribute significantly more as the flexure thickness increases. For extremely large flexures, $t_f > 0.14cm.$, the bending stress tapers off due to the excessive rigidity of the device in this range.

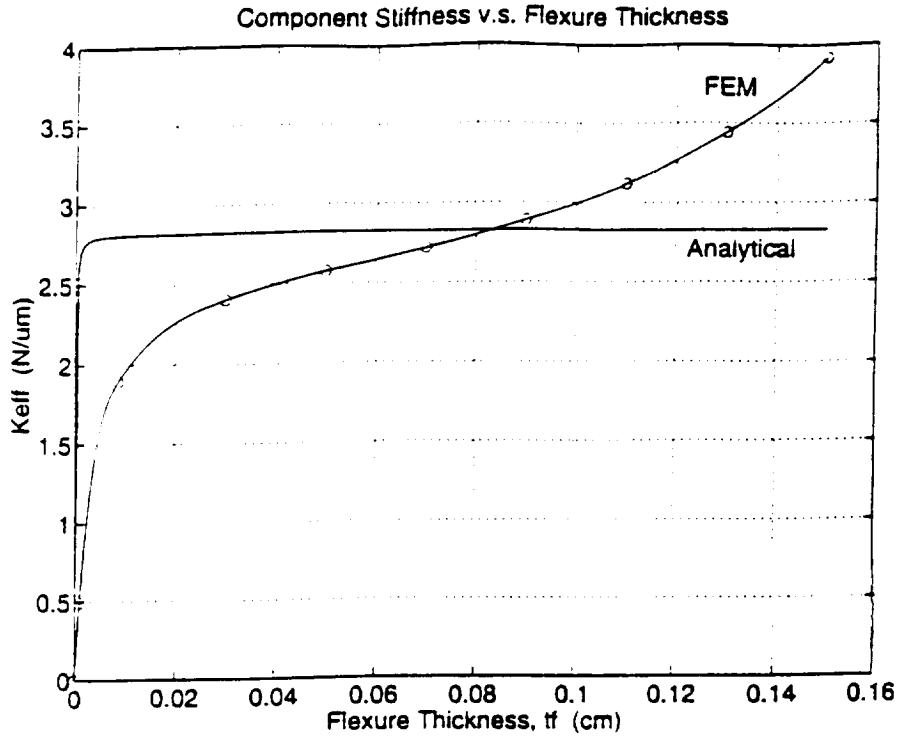

Figure 38. Component stiffness versus flexure dimensions, where $\theta = 10^{\circ}$, $b = 2cm.$, $t_{pz} = 1cm.$, $L_{pz} = 4cm.$, $L_f = 0.4cm.$, and $K_p = 91N/\mu m$. Comparison of analytical and finite element solutions.

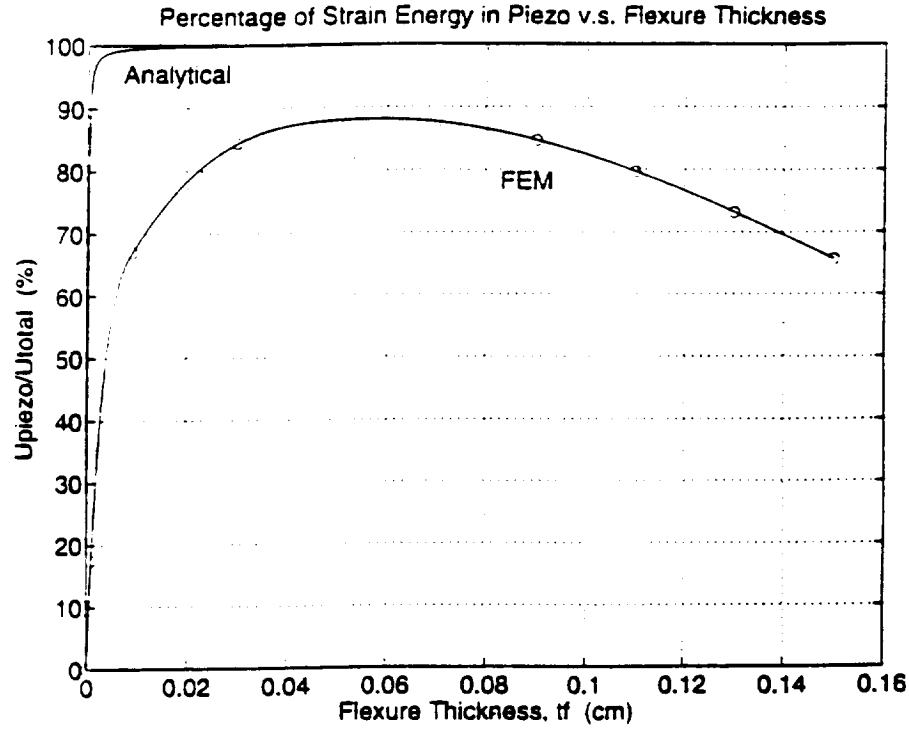

Figure 39. Piezoelectric strain energy versus flexure dimensions, where $\theta = 10^{\circ}$, $b = 2cm.$, $t_{pz} = 1cm.$, $L_{pz} = 4cm.$, $L_f = 0.4cm.$, and $K_p = 91N/\mu m$. Comparison of analytical and finite element solutions.

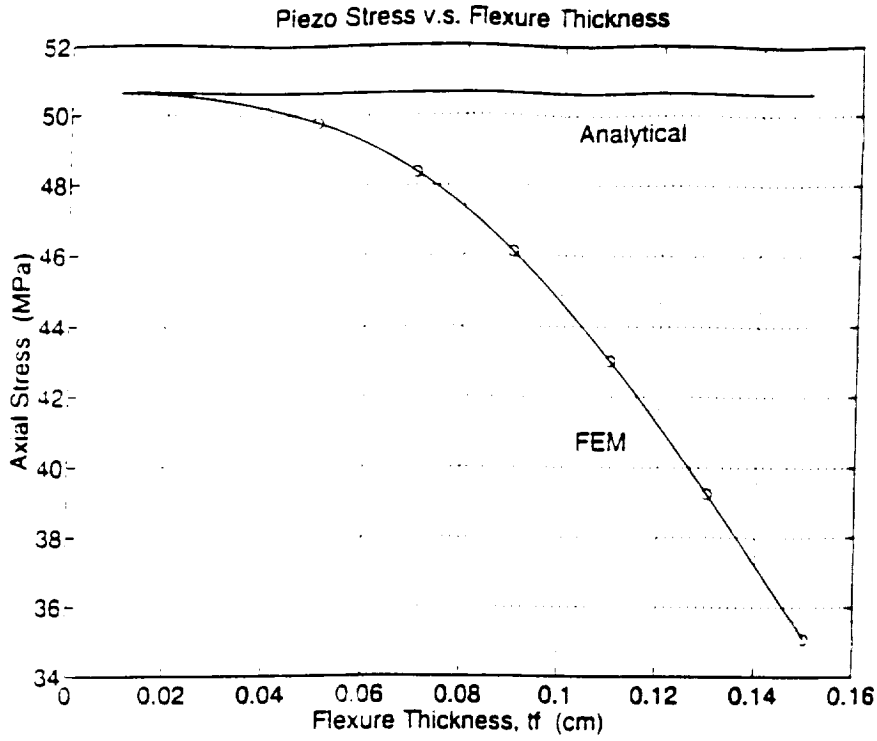

Figure 40. Piezoelectric stress versus flexure dimensions, where $\theta = 10^{\circ}$, $b = 2cm.$, $t_{pz} = 1cm.$, $L_{pz} = 4cm.$, $L_f = 0.4cm.$, and $K_p = 91N/\mu m$. Comparison of analytical and finite element solutions.

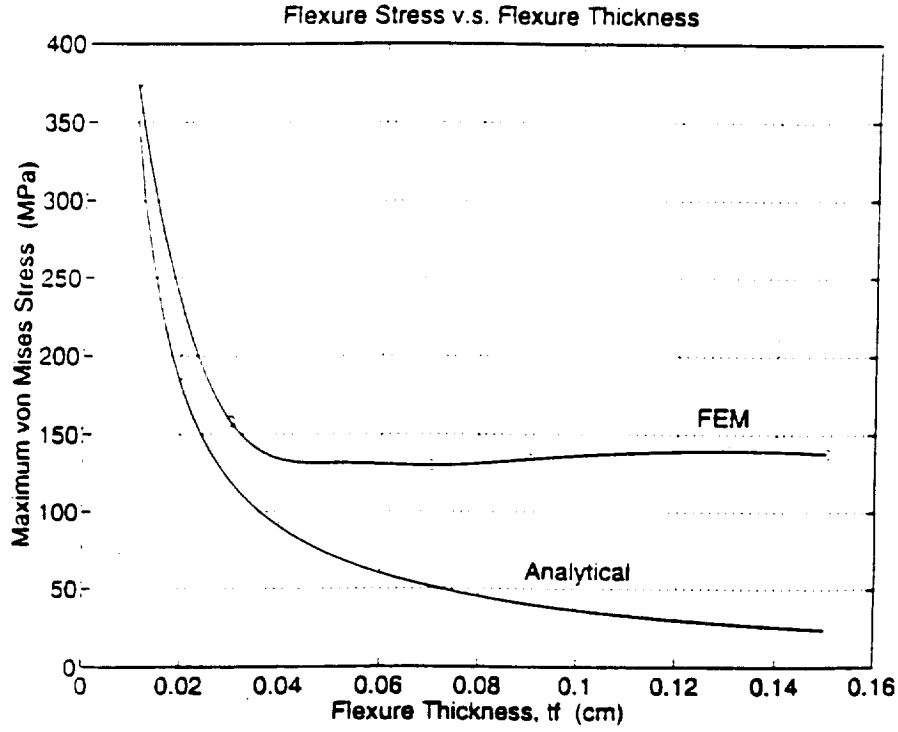

Figure 41. Flexure stress versus flexure dimensions, where $\theta = 10^{\circ}$, $b = 2cm.$, $t_{pz} = 1cm.$, $L_{pz} = 4cm.$, $L_f = 0.4cm.$, and $K_p = 91N/\mu m$. Comparison of analytical and finite element solutions.

3.5. THE NEW COMPONENT DESIGN

The original component that was designed with the analytical model, needs refinement. The experimental results motivated a second component design as well. Unpredictably high measured stiffnesses indicated that the truss model stiffness derivation was in error by a factor of two. The corrected model was presented earlier in this chapter. The experimental results are discussed in the next chapter.

The remainder of this chapter discusses improvements to the analysis and design of the component. Section 3.5.1 discusses the undesirable flexibilities that were not accounted for in the truss model design. The elimination of these undesirable flexibilities is also discussed. Section 3.5.2 presents the design constraints and solution procedure using the NASTRAN component model, that were previously discussed in section 3.3. This section attempts to show how the original design's stiffness is reduced and performance fine-tuned through an iterative design procedure accounted for in table 1.

3.5.1. LOCAL ELASTICITY ANALYSIS AND MODEL REFINEMENT

There are two undesired flexibilities in the above models that need to be addressed. The relatively high tensile stress in the smaller flexure, modeled as a single beam element, decays into the larger semi-rigid beam with low tensile stress. The depth of the decay, defined as the *footprint length*, plus the original flexure's length yields the *effective length* of the flexure to be used in the truss and finite element models discussed in earlier sections. The second undesired flexibility is caused by the smaller flexure's eccentricity with respect to the center of the larger semi-rigid beam. When the flexure is pulled in tension, the off-center axial force induces an undesirable bending moment and compressive bending stresses about the lever arm's neutral axis. The beam's curvature from the bending stresses reduces the overall axial stiffness of the lever arm.

In either case, the unmodeled flexibility, 1/K?, can be found by comparing the overapproximated two-beam junction with two-dimensional stress elements on any commercial finite element program. The total stiffness is calculated from the applied force and total displacement quotient, $K_{total} = (F/v)_{FEM}$. The stiffnesses, $K_1 = EA_f/L_f$ and $K_2 = EA_{srb}/L_{srb}$ are the nominal axial stiffnesses of the flexure and the semi-rigid beam, respectively. The mystery stiffness, K?, is backed out of the following equation:

$$K_{total} = \left(\frac{1}{K_1} + \frac{1}{K_2} + \frac{1}{K_?} \right)^{-1} \tag{53}$$

The footprint length, $L_{fp} = EA_f/K_?$, is added to the nominal flexure length, L_f, to determine the effective length of the flexure.

$$L_{eff} = \frac{EA_f}{K_?} + L_f$$

This mystery stiffness was added to the component finite element model. It is essentially an unwanted flexibility in series with the piezoceramic stack. The finite element model in figure 42(a) shows the bending tensile stress that makes the outer beam material useless for transmitting strain energy into the piezoelectric.

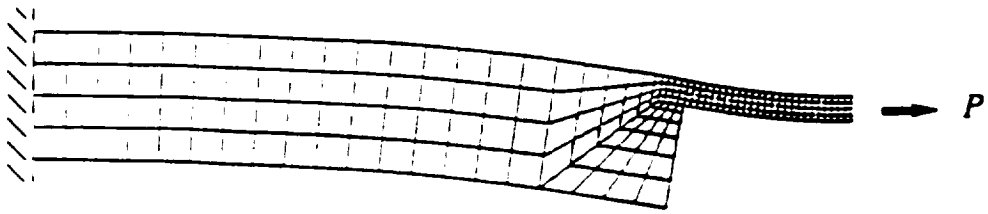

Figure 42(a). Finite element modeling of flexure/semi-rigid beam interaction. This old design included beam eccentricities. The effective length, L_{eff} = 11.88mm, is 2.29 times as long as its nominal length, L_f = 5mm. (t_f = 0.8mm; t_{srb}= 4.0mm; L_{srb}= 40mm). The *footprint length* is 8.6 times the flexure thickness.

The deflected shape of the finite element mesh in figure 42(a), depicts the undesirable effects from eccentric loading. The eccentric load induces both an axial load and a bending moment throughout the semirigid beam. As the beam bends, the bending stress increases the elongation at the top of the semirigid beam (flexure/semirigid-beam interface). This undesirable elongation increases the overall flexibility of the lever arm, as well as the non-piezoelectric strain energy throughout the component.

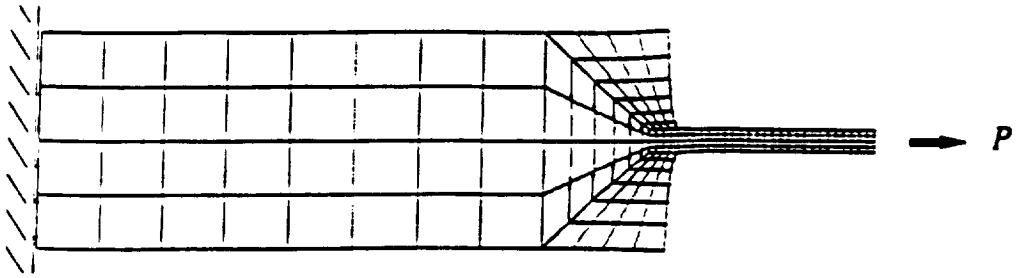

Figure 42(b). Finite element modeling of flexure/semirigid beam interaction. Since, this design is symmetric, undesirable compressive stresses are eliminated. The effective length, L_{eff} = 5.88mm, is 1.18 times as long as its nominal length, L_f = 5mm. (t_f = 0.8mm; t_{srb}= 7.2mm; L_{srb}= 40mm). The footprint length is 1.1 times the flexure thickness.

A close look at the deflected shape of the finite element mesh near the flexure/semirigid-beam interface in figure 42(b), indicates that the flexure's relatively large axial strain does not drop instantaneously to the lower strain level in the semirigid beam. The larger strain level of the flexure decays gradually into the semirigid beam, thereby causing an increase in the flexure's effective length. The new design doubles the flexure's potential to channel strain energy into the piezoelectric, since the flexure's *effective length* is decreased by about 50%.

3.5.2. SECOND ITERATION DEVICE OPTIMIZATION WITH NASTRAN

The NASTRAN finite element model of the component is a fast and most accurate method in finding the optimal design of the component. The only drawback of the NASTRAN model is that an iterative design procedure is necessary to optimize the solution. Specifically, each program output directs subsequent input by trial and error, not by design curves.

For a given piezoelectric stack, the finite element analytical model of the component consists of four output variables ($K_{eff}, U_{piezo}, \sigma_{piezo}, \sigma_f$), that are dependent on 10-input variables ($\theta, b_f, b_{srb}, b_{piezo}, t_f, t_{srb}, t_{piezo}, L_f, L_{srb}, L_{piezo}$). If the design problem were left unconstrained, there would conceivably be four 10-dimensional design curves to be drawn from the analytical finite element model. Unfortunately, graphing these curves is obviously limited to three dimensions. For a three-dimension graphing package this means one output variable can be optimized for any given two input variables. Therefore, the order of the design problem must be reduced.

Dimensional constraints dictated by the congested apex interior, and imposed design constraints based on engineering judgment were used to simplify the component design. The intersection of the eight inch hexagonal plate in the apex interior (see chapter 2, figure 26) with each of three apex walls, creates a rigid corner base mount for the six components. Mounting the components to the plate or the apex walls subjects the six-axis design to plate bending flexibility. Since two components must fit side-by-side along the eight inch base with adequate margins, the length of the component is limited to a maximum of 5.5inches. This, in turn, constrains the piezoelectric length, L_{piezo}, to 8 to 10 cm, depending on the shim design. Since wide "index finger" width shims can be manually aligned easier than thin shims, during the component assembly process, L_{piezo} was constrained to 8cm.

The piezoelectric beam thickness, t_{piezo} was limited to 8mm. If the thickness exceeds 8mm, undesired flexibility is introduced across the preload spring bridge, which acts like a simply supported beam with center point load. In addition, this would necessitate replacing

the two-dimensional analytical model with a three-dimensional finite element model. Of course, smaller diameter springs would release this constraint. Unfortunately, the only way to put a high loading, negligible stiffness spring, within the height constraint, is to use a relatively wide spring base of 20mm. The height constraint was dictated by:

$$h_{device} = 2(L_{lever}\sin(\theta) + d_{torsion}), \tag{54}$$

where $d_{torsion}$, the dual parallel lever arms separation distance, is 10mm. This gives torsional stability about the device's centroid. If single lever arms were used, the torsional strength would depend almost entirely on the shear mode strength of the piezoelectric beam.

The 14mm piezoelectric beam width, b_{piezo}, was sized to give the correct stiffness, from the analytical model's lever ratio to effective stiffness correlation, as well as for providing additional buckling stability for the device in its weaker torsional axis. It should be noted that setting the thickness equal the width, $t_{piezo} = b_{piezo} =$ 8mm, would be very effective in reducing the component's stiffness at a less critical lever ratio. This option was not investigated on the basis of enforcing reasonable torsional rigidity in the weak axis of the component. The 14:8 ratio is a back-of-the-envelope correlation between the torsional strengths in their respective axes.

The semi-rigid beam dimensions can also be prescribed to eliminate more variables from the design optimization. Once the variable flexure length, L_f, the variable lever angle, θ , the constrained preload spring footprint (L_{sfp} =20mm), and the total length of the component (L_{total} = 5.5inches), are selected, the semi-rigid beam length, L_{srb}, can be determined by:

$$L_{total} = L_{sfp} + 2(L_{srb} + 2(L_f))\cos(\theta) \tag{55}$$

Since the ideal component has infinitely stiff beams connected by perfect hinges, the thickness of the semi-rigid beam, t_{srb}, should be in excess of 10 flexure thicknesses, t_f. If the semi-arbitrary dual lever-arm separation distance of 10mm were increased to 15 or 20mm, not only would the torsional stability increase via an increase in the system's effective torsional moment arm, but the semi-rigid beam's thickness, t_{srb}, would be unconstrained. This option was not investigated in order to avoid creating an excessively bulky product for difficult assembly onto the congested apex interior of the ASTREX testbed. In addition, excessive stress gradients were also avoided, and an aesthetically pleasing part was created by constraining the semi-rigid beam length by the following ratio:

$$\frac{t_{srb}}{L_{srb}} \approx \frac{t_f}{L_f} = 0.16 \tag{56}$$

Thus, t_{srb} = 7.2mm. was selected. Maximizing the beam widths to equal the full width of the spring base, $b_f = b_{srb}$=20mm, is justified by considering the component design in figure 43.

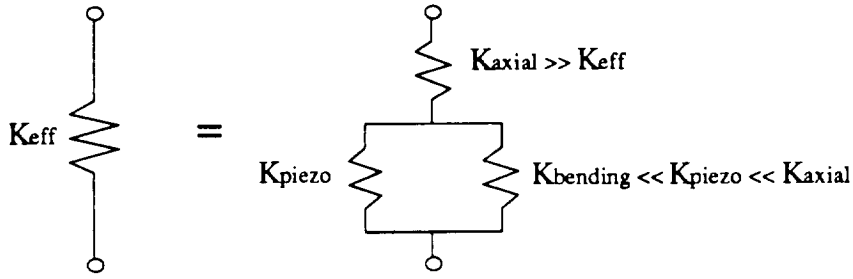

Figure 43. Conceptual component stiffness diagram.

In order to channel as much strain energy into the piezoelectric as possible, the axial stiffness of the flexures must be as stiff as possible. However, the more the piezoelectric is strained, the more the flexures absorb bending strain energy. In order to reduce this affect, the bending stiffnesses must be minimized. Thus, the flexures must be designed with maximum cross-sectional area and minimum moment of inertia to cross-sectional area ratio

$$(A)_{\max} = \max(bt) \tag{57}$$

$$\left(\frac{I_{zz}}{A}\right)_{\min} = \min\left(\frac{bt^3}{12bt}\right) = \min\left(\frac{t^2}{12}\right). \tag{58}$$

The unconstrained finite element based design problem consisted of optimizing ten input variables, $(\theta, b_f, b_{srb}, b_{piezo}, t_f, t_{srb}, t_{piezo}, L_f, L_{srb}, L_{piezo})$, to obtain the desired output variables $(K_{eff}, U_{piezo}, \sigma_{piezo}, \sigma_f)$. After constraining the design problem, only three input variables are independent: (θ, t_f, L_f).

Values of these three input variables are iterated in table 1 until the original design's stiffness, stresses, and strain energy errors are corrected with the optimal values. Optimization convergence is efficient if high-range performance-sensitive variables are realized, first. Then the design can be fine-tuned with the low-range performance-insensitive variables with minimal to negligible high-range variable updating required. To this end, design mistakes are adjusted first, lever angles are corrected second, and flexure lengths and thicknesses are adjusted last.

	Changed Variable	θ (degrees)	L_f (cm.)	t_f (cm.)	K_{eff} (MN/m)	σ_{piezo} (MPa)	σ_f (MPa)	U_{piezo} (%)
STEP ONE: Correcting Design Mistakes								
1	—	21.8	0.50	0.08	10.52	22.16	61.08	71.3
2	b	21.8	0.50	0.08	12.13	22.04	37.79	81.2
3	t_{srb}	21.8	0.50	0.08	12.43	22.05	37.54	83.3
STEP TWO: Decrease Lever Angle and Effective Stiffness								
4	θ	20.0	0.50	0.08	10.35	24.17	42.74	83.35
5	θ	18.0	0.50	0.08	8.31	26.97	50.16	83.32
6	θ	16.0	0.50	0.08	6.53	30.40	60.10	83.11
7	θ	14.0	0.50	0.08	4.98	36.22	79.76	82.51
8	θ	12.0	0.50	0.08	3.67	42.12	101.32	81.69
9	θ	**10.0**	0.50	0.08	**2.58**	47.55	125.10	**80.47**
STEP THREE: Decrease Flexture Length								
10	L_f	**10.0**	0.45	0.08	**2.61**	47.32	131.10	**80.53**
11	L_f	10.0	0.40	0.08	2.64	47.04	138.59	80.49
12	L_f	10.0	0.35	0.08	2.68	46.67	148.17	80.31
13	L_f	10.0	0.30	0.08	2.73	46.10	163.16	79.77
14	L_f	10.0	0.25	0.08	2.77	45.52	178.14	79.22
STEP FOUR: Decrease Flexure Thickness								
15	t_f	10.0	0.25	0.07	2.67	47.07	173.07	81.56
16	t_f	10.0	0.25	0.06	2.59	48.31	168.18	83.21
17	t_f	10.0	0.25	0.05	2.52	49.25	165.10	84.12
18	t_f	**10.0**	0.25	0.04	**2.45**	49.91	166.74	**84.17**
19	t_f	10.0	0.25	0.03	2.44	50.32	179.40	83.13
STEP FIVE: Design Check								
20	t_f	10.0	0.50	0.07	2.51	48.51	123.9	81.36
21	t_f	**10.0**	0.50	0.06	**2.44**	49.26	124.06	**81.65**
22	t_f	10.0	0.50	0.05	2.38	49.82	127.08	81.25

Table 1. Iterative component design data from NASTRAN finite element code with local elasticity analysis included.

It is educational and physically insightful to describe the twenty-two iterations listed in table 1. First, an introduction to the structure of table 1 is needed. It should be noted that the value of only one input variable is changed with each new line. The design iterations of

table 1 can be divided into the following 5 major design steps: 1. The original design on line 1 was corrected with the doubled lever arm width on line. The semi-rigid beam thickness on line 3 was corrected with a new flexure thickness. 2. Component stiffness is reduced by decreasing the high-range variable, theta, on lines 4 through 9. 3. The manufacturable optimal solution on line 10, is found from the iteration in lines 10 through 14 (flexure machining is limited to 0.8mm thicknesses). 4. The optimal solution, line 18, is found from the iteration in lines 15 through 19. 5. The iterations on lines 20 through 22 in path 2 serve as a check to see if the optimal solution is within the space spanned by the semi-arbitrary iteration scheme. These six items are discussed in the following six paragraphs, respectively.

Step 1: When the original design listed on line 1, doubles its lever-arm width to 2cm and increases its semirigid beam thickness, t_{srb}, from 4 to 7.2mm, the piezoelectric strain energy, and the component stiffness increase, while the stress in the flexures decreases as expected by the decrease in bending curvature from the stiffer flexures.

Step 2: Lines 4 through 9 show the effect of reducing the high-range variable, θ, to reduce the component's stiffness to the desired 2 to 3MN/m range. The lever angle needed to attain this stiffness, was fortunately not less than the 10 degree minimum. The minimum lever angle was determined by

$$L_{arm}\cos(\theta_{\min}) \geq 0.5 t_{piezo}, \tag{59}$$

which prevents the steel device from contacting the middle of the piezoceramic beam. The lever angle reduction from lines 5 through 6 shows some interesting trends. Here the lever angle drops 2 degrees, the stiffness drops 1.78MN/m, the lever ratio (equation 1) increases from 3.49 to 3.95, the stress in the piezoelectric and flexure increase, and the strain energy in the shims stays steady at 3.11% of the total. As the lever ratio (L.R.) increases, the fraction of strain energy in the flexures increases due to the larger stroke.

$$L.R. = \frac{v_{device}}{u_{piezo}} \tag{60}$$

Step 3: Lines 10 through 14 shows a design iteration that decreases the flexure's length while its thickness is kept constant. For example, in lines 9, 10 and 11, the flexure length decreases from 0.50mm to 0.45mm to 0.40mm, the component stiffness and flexure stress increase, the lever-ratio and piezoelectric stresses decrease, the piezoelectric strain energy reaches a maximum of 80.53% for the middle iteration. This local maximum is considered the optimal "manufacturable" device, since the flexure thickness is not too small for wire electron-discharge machining. In addition to the data on line 10, this design has a lever

ratio of 6.34 and 11.84%, 4.62% and 3.01% of the strain energy in the flexures, the semi-rigid beams and the shims, respectively. Notice how the piezoelectric strain energy decreases from the "manufacturable" optimal, as the flexure length is reduced to 0.5mm and the total von Mises stress is built up to a maximum of 178MPa; 77% of this stress is undesired bending stresses.

Step 4: Beginning with this iteration, the flexure thickness is decreased in order to release the build up of unwanted bending strain energy. This increases the piezoelectric strain energy to its optimal value of 84.17%, with a flexure thickness of 0.04mm. In addition to the data on line 18, this design has a lever ratio of 6.40 and 7.60%, 5.06% and 3.15% of the strain energy in the flexures, the semi-rigid beams and the shims, respectively. From the two optimums mentioned thus far, the trend suggests that for each reduction in the flexure length there is a proportional reduction in the flexure thickness that will yield even more strain energy than before. This investigation was unnecessary since maximum design stresses for the piezoelectric and the steel flexures were realized. A piezoelectric stress of 50MPa was enforced to prevent non-linear depolarization stresses depicted in figure 1. Forty Rockwell quenched and tempered steel that yields at approximately 600MPa was factored down to a maximum design stress of 200MPa to give the flexures a factor of safety of about 3.0.

Step 5: The best design considered in this iteration set, line 21, has less strain energy than the previously mentioned optimal value. This fact reconfirms that the optimization is within the design space spanned by the two iteration paths, namely step 4.

The new component to be built can be reduced in size considerably, if the piezoelectric shims are discarded. This can be done if machining tolerances are small for both the piezoelectric as well as the flex-tensional component. Discrepancies between the piezoelectric stack and the steel flex-tensional part can be alleviated by an appropriate preload adjustment now available in the new design, depicted in figure 44. For a lever angle of 10 degrees, the springs are incorporated into the rigid block volume to keep the bulk of the component as low as possible. The threaded spring plugs allow for easy preload adjustment with a large flat-head screwdriver. The center hole in the top plug also allows room for the threaded mechanical stop bolt.

The assembly procedure for the new device is as follows. 1. The threaded bolt is screwed into the bottom of the device. 2. The lower threaded plug is screwed down until it locks with the threaded bolt head. 3. The lower lock nut and travel stop nut is screwed down and locked together at the desired height. The desired height is determined from the stroke limit and the spring deformation that induces the desired piezoelectric preload. 4. The two springs are placed in the component, on top of the lower threaded plug. 5. While

the piezoelectric stack is held in its appropriate position, the upper threaded plug is lowered to its desired height, and piezoelectric preload is attained. 6. The upper travel stop nut and lock nut are screwed onto the threaded bolt, and locked together at the stoke limit.

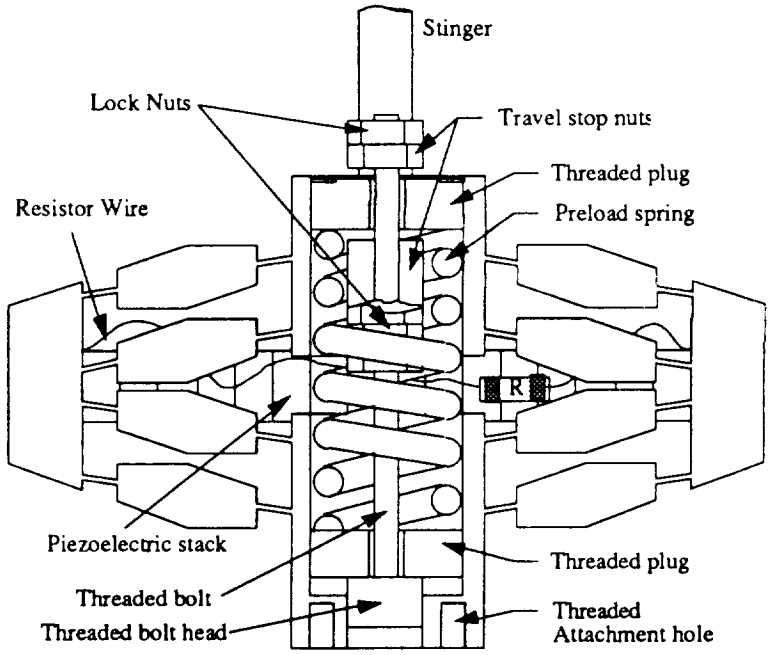

Figure 44. New EDM component design features include adjustable preload spring plugs, tapered rigid beams, and no shims.

CHAPTER 4

EXPERIMENTAL VERIFICATION OF COMPONENT PERFORMANCE

Once the six-axis tuned-mass damper was designed, building and testing of the design must be acceptable at three different levels before a prototype is ready to be built and installed in the space structure to be damped. Level one: Piezoelectric material properties manufacturing and testing by the manufacturer. Level two: Flex-tensional component level manufacture and testing. Level three: Manufacture and testing of six redesigned components/stingers, mounting blocks/bolts, and proof mass assembled in six-axis configuration. The level one and two verification tests that are described in this chapter, attempt to validate flex-tensional piezoelectric actuator technology. The level three tests are simulated in chapter five.

The microcomponent tester in figure 45 was used to measure component stiffness and

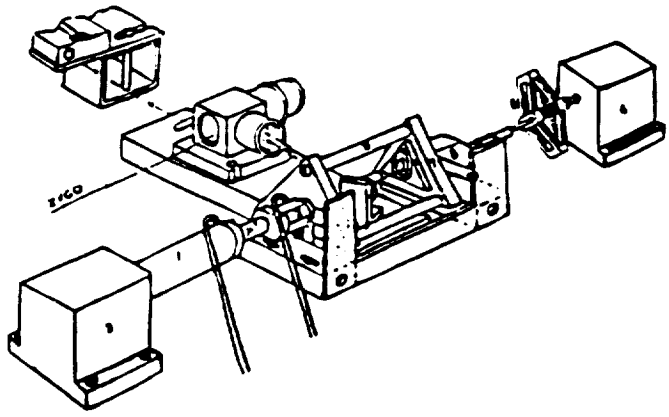

Figure 45. Interferometric Microcomponent Tester.

loss factor as a function of frequency and shunting resistance. The piezoelectric actuator drives a user-input sinusoidal or bandwidth limited white noise force signal through a load cell and into the component to be tested. A laser interferometer setup is used to measure component deflection. Component stiffness can be measured from these force and displacement measurements. Component loss factor can be measured from the tangent of the phase lag between these two measurements as by equation (75) in the next section.

The component tester is bolt-mounted onto a 4 foot wide, 12 foot long, 6 inch wide optics bench. The optics bench is isolated from the dynamics of the laboratory building floor with six rubber air tubes (12 inch outer diameter and 4 inch tube diameter). The low-stiffness tubes give the bench a rigid-body mode of 1.5Hz. The optics bench dynamics begin with a first bending mode near 82Hz.

Reacting off the left-hand mass, the piezo strut drives displacements into the load cell, as previous depicted in figure 45. The load is channeled to the component via a tri-bolt steel cage assembly. The cage assembly is designed to accommodate target reflector mounting directly above the component's stinger. The load then travels through the stinger and the component to the the right-hand reaction mass.

4.1. THE COMPONENT TESTER HARDWARE

The component tester hardware consists of a piezo driver strut, a load cell, a zygo laser and sensor, and data acquisition hardware as described in this section and in more detail in reference [21].

A Physik Instrumente piezoelectric strut and Kepco BOP 500M bipolar amplifier is used to drive the component with specified random or sinusoid inputs. Once the amplifier is biased with -250 volts, a maximum input of 0 to -500 volts may be applied across the strut's 1.5μF capacitance to yield maximum displacements of ±15μm. Because the amplifier has a limit of 80 mA, the piezo strut will not achieve full displacement at high frequencies as shown in figure 46. In order to maximize the displacement capability of the actuator, sinusoidal inputs were limited to the 1 to 40Hz range. It should be noted that 15μm is approximately one 20th of the actual displacement the component was designed to handle in space. This was not a concern, since the component's linear range was assumed to encompass the range of experimental and design displacements. The expression relating frequency, voltage and current drawn by the driving actuator is:

$$i = 2\pi fCV \tag{61}$$

This equation was used to prevent damaging the driving actuator. If the input is sinusoidal at frequency, f, the voltage is chosen such that $i \leq 80\text{mA}$, to prevent the actuator from

buzzing (signal distortion). If the input is RMS, the voltage is chosen such that $i \leq (80/3)$mA, to prevent the actuator from *clicking* (overload).

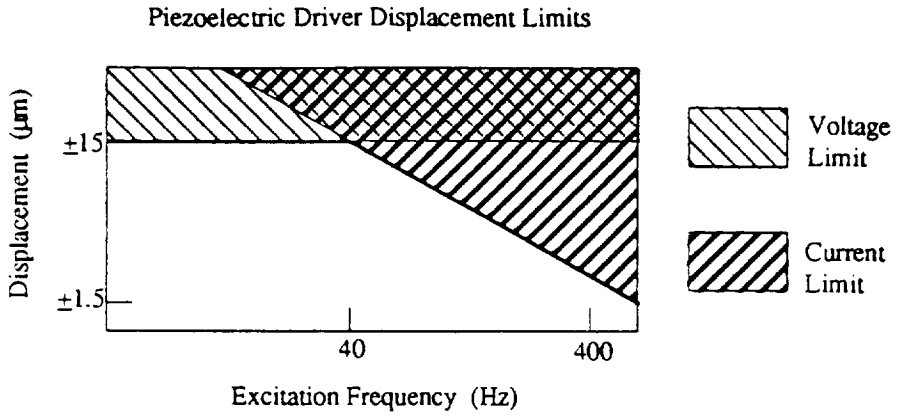

Figure 46. Displacement limits in the piezo strut driven with a sine wave of (250V)sin(2πfCV).

A load cell (PCB Model 208A02, SN 3633) was used to measure the applied component force. The load cell was calibrated at 50.5mV/lb with a minimum test frequency of 0.2Hz. The raw data is transmitted to a load cell conditioner and then sent to a Gateway 2000 computer-based Tektronix 2630 Fourier Analyzer which is used for data acquisition and Fast-Fourier transforms.

An AXIOM 2/20 laser-based measurement system uses interferometry to measure the linear displacement of the component as depicted in figure 47. This system consists of a two-frequency laser head, beam directing and splitting optics, measuring optics, receivers, and electronics. The light beam emitted from the laser head is directed through measurement optics and then to an optical receiver. The receiver provides an electrical measurement frequency that is compared to a reference frequency from the laser head. System electronics compare the frequencies and calculate the measurement. The signal is amplified to a sensitivity of 2.048μm/V to accurately measure displacements within the ±20.48μm range. Precise measurement data is updated at a 7 to 13 MHz sampling rate. The raw data is transmitted to a Gateway 2000 computer, where a Tektronix 2630 Fourier Analyzer transforms time-domain data into frequency domain data.

After the Tektronix box transforms data from the laser output, Ch.1, and the load cell conditioner, Ch.2, into the frequency-domain, the data can then be displayed with the user-interface program. This program displays stiffness transfer functions (*i.e.* Ch.2/Ch.1), and loss factor transfer functions (*i.e.* phase(Ch1.,Ch2.)). Coherence transfer functions between the input and output, and a spectral decompositions of the input and output were

also available from the CTEST display to help search for various causes of component data errors. The CTEST program also commands the Tektronix box to send a signal to the Kepco amplifier to drive the piezo strut with user-supplied amplitudes and frequency distributions.

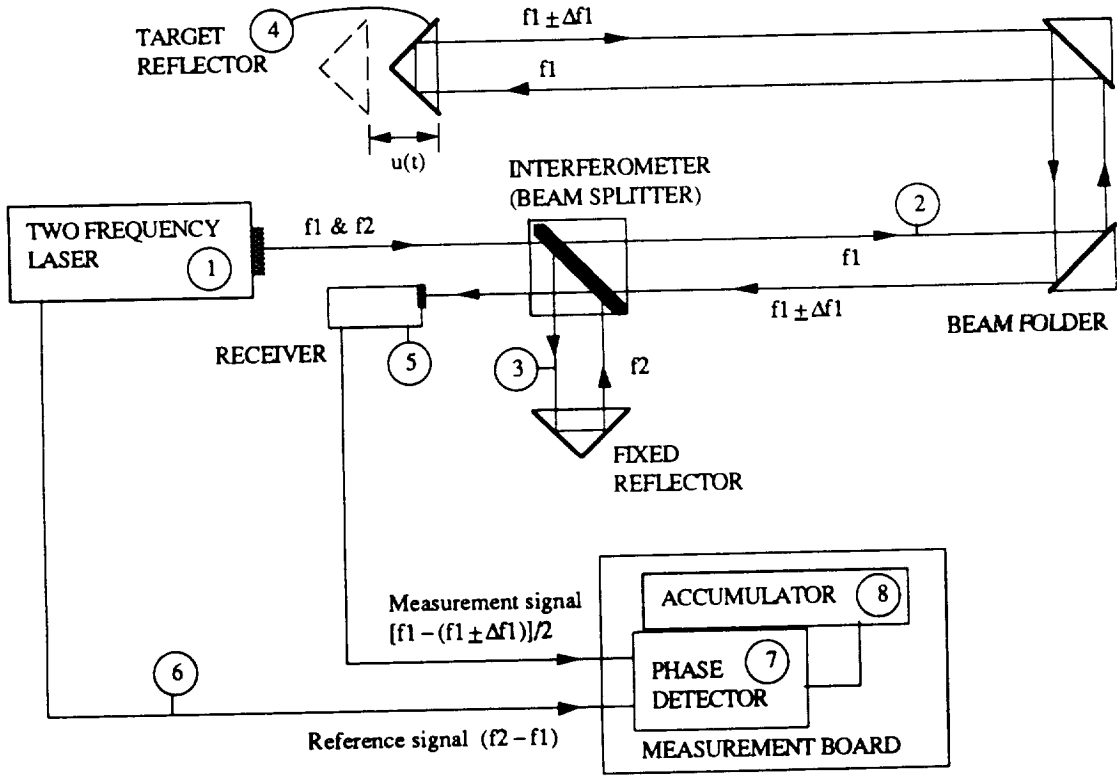

Figure 47. AXIOM 2/20 Block diagram: 1. The laser generates light of two different frequencies with orthogonal polarizations. 2. One of the two frequencies f1, is optically separated and directed to the target reflector. 3. The second frequency, f2, is optically separated and sent to a fixed reflector and then rejoins f1 at the interferometer to produce an interference signal. 4. As the target reflector moves, the returning beam frequency will be Doppler-shifted up or down by Δf1 depending on the direction of motion. 5. Receiver changes f2 and (f1± Δf1) to an electrical measurement signal (20 MHz ± Δf1). 6. Electrical reference signal from laser. (20MHz) This signal is divided by 2. 7. Phase detector calculates phase difference between reference signal and measurement signal. 8. Accumulator adds up the phase differences and outputs u(t) measurement data in 32-bit binary words.

4.2. CALIBRATING THE COMPONENT TESTER

While calibrating the component tester, slop/stiction, hysteresis, directional stiffness due to threads, and flexibility need to be checked. All these tests, except flexibility, can be

conducted by the insertion of a steel rod into the test fixture and running tests at different frequencies and amplitudes. Slop/stiction can be tested by inputting a quasi-static (0.1to 1Hz) sinusoidal voltage into the actuator and checking the displacement versus force for slop. This was repeated with different amplitudes. Hysterisis was checked in a similar way, except the force needed to be at a higher frequency less than 200Hz. The directional stiffness of the test apparatus was removed by trying different preloads and comparing measured stiffnesses. The point of zero stiffness was not easily found without a trial and error bolt adjustment of the test fixture. Flexibility in the test fixture affected the measured stiffness of the component as shown in figure 48.

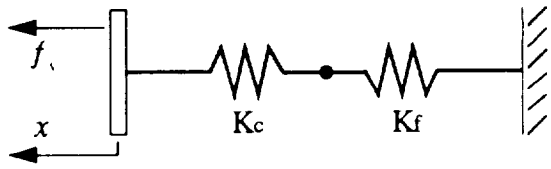

Figure 48. Fixture stiffness Kf, represents the stiffness of the threads, linkages, table, bolts and couplers. Kc is the component stiffness. f and x are measured output.

The fixture stiffness was determined experimentally to be about Kf = 45N/μm ± 10%. The error depends on the preloads from installation. The measured stiffness, $K_m = f/x$, was substituted into equation (62) to correct for the fixture stiffness.

$$\frac{1}{K_c} = \left(\frac{1}{K_m} - \frac{1}{K_f} \right)$$

$$\text{or,} \quad K_c = \frac{K_m K_f}{K_f - K_m} \tag{62}$$

The calculated value for K_c has an error associated with the 10% uncertainty in fixture stiffness K_f :

$$\frac{dK_c}{K_c} = \left(\frac{\partial K_c}{\partial K_f} \right) \times \left(\frac{dK_f}{K_c} \right) = \frac{-1}{\left(K_f / K_m \right)^2} \times \frac{dK_f}{K_c} \tag{63}$$

For example, if $K_c = 10\,N/\mu m$ and $K_f = 45\,N/\mu m \pm 10\%$ then

$$\left| \frac{dK_c}{K_c} \right| = (.05)\left(\frac{4.5}{10} \right) \cong \pm 2.3\% \tag{64}$$

4.3. COMPONENT TEST DATA

In order to verify the component design, stiffness and loss factor, test data was collected as follows. First, the effective capacitance of the piezoelectric was calculated. The resistor was selected from the following equation to tune the peak damping curve near 30Hz.

$$\rho = RC\omega \tag{65}$$

where ρ=1, ω=30Hz, C=15microfarads and R=390kΩ. It should be noted that the internal resistance of the piezoelectric capacitor was a negligible 0.245Ω.

Second, forty logarithmically-distributed resistors were selected about the ρ=1 center point, where R=390kΩ. More specifically, the first resistor used was 3.9kΩ to obtain data at ρ=0.01. Similarly, the fortieth resistor used was 39000kΩ, to obtain data at ρ=100. This approach was used to obtain data for two decades on both sides of ρ=1. In addition to the short-circuit and open-circuit transfer functions, forty stiffness and phase transfer functions were generated with each resistor using a thirty count average.

Two data points, 10Hz and and 42Hz, were semi-arbitrarily chosen to extract stiffness and phase data directly off the respective transfer functions. These frequencies demonstrated excellent signal to noise ratios. A seven-point discrete frequency average was computed about these two frequencies to smooth the noise on the transfer function. More specifically, stiffness and phase data at 9.25Hz, 9.5Hz, 9.75Hz, 10Hz, 10.25Hz, 10.5Hz and 10.75Hz were summed and then divided by 7 to eliminate the noise on the transfer function. A similar procedure was done at 42Hz.

The stiffness magnitude and loss factor was determined from the complex stiffness, $K(\omega) = K(1 + i\eta(\omega))$, output as follows.

$$\|K(\omega)\| = \sqrt{(\mathrm{Re}(K(\omega)))^2 + (\mathrm{Im}(K(\omega)))^2}$$

$$\eta(\omega) = \tan(\psi(\omega)) = \left(\frac{\mathrm{Im}(K(\omega))}{\mathrm{Re}(K(\omega))}\right) \tag{66}$$

For reference, the classical definition of damping loss factor is

$$\eta(\omega) \equiv \frac{1}{2\pi} \frac{\left(Energy|_{dissipated}\right)/cycle}{\left(Energy|_{max\ stored}\right)/cycle} \tag{67}$$

The damping coefficient is one-half of the loss factor, $\zeta \cong 0.5\eta$, for small η.

The following plots and experimental curve fits show the results of this procedure. The 10Hz data represented by x's, and the 42Hz data represented by o's, show negligible

differences, from the experimental curve fit. The generalized coupling coefficient can be determined from the experimental data by equation (68).

$$k_{ij}^2 = \left(\frac{K_{sc}}{K_{oc}} \right)\Bigg|_{measured} \tag{68}$$

The non-dimensional stiffness curve fit was generated by substituting the generalized coupling coefficient into the stiffness and loss factor equations of chapter one (equation (2) and (3)).

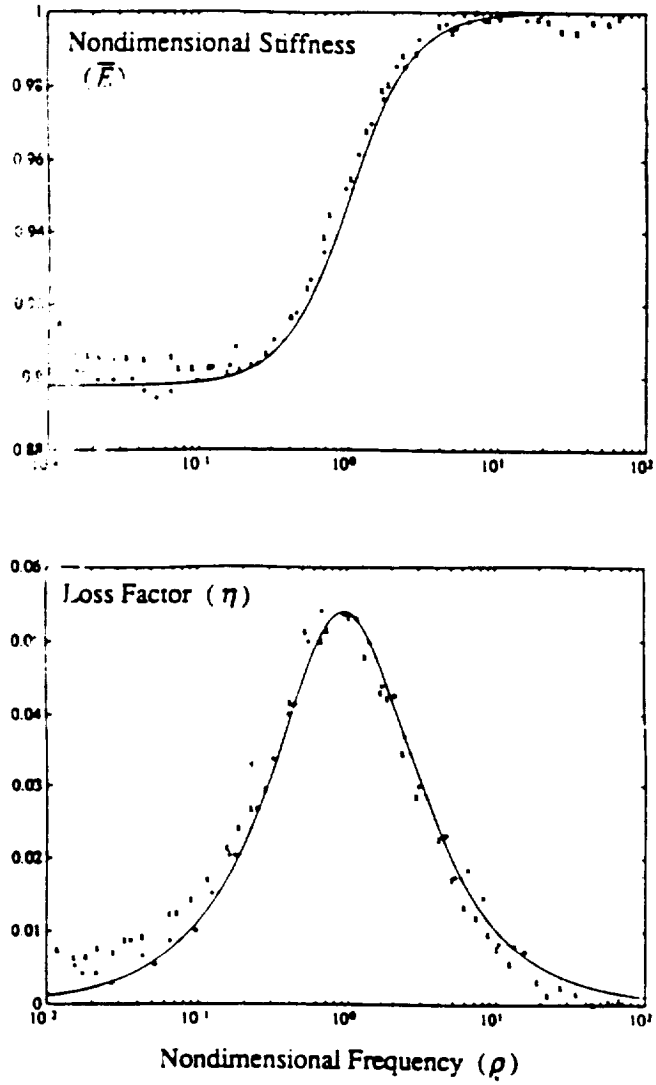

Figure 49. Nondimensional stiffness and loss factor data for experimental component data.

Although the stiffness change and loss factor are overestimated by the finite element model, the curves are clearly indicative of the predicted first-order frequency-dependent

stiffness change and the bell-shaped loss factor distribution. The results are summarized in the next section 4.4.

The piezoelectric stack was tested by the Specialty Engineering Associates, Inc. to verify material properties (reference [22]). The frequency-dependent impedance, Z(ω), was determined by driving the piezoelectric stack with V(ω), and dividing by I(ω). The impedance is at a minimum at the first axial resonance or pole of the stack. The frequency at which this occurs can be used to calculate the effective modulus of elasticity of the stack:

$$f_{pole} = \frac{1}{2L}\sqrt{\frac{EA}{\mu}} \tag{69}$$

Substituting $\mu = \rho A$ into (69) and solving for E yields:

$$E_{stack} = 4\rho\left(f_{pole}L\right)^2 = 63.2GPa \tag{70}$$

where, $f_{pole} = 18.1kHz$, $L = 8cm$ and $\rho = 7550kg/m^3$ for the piezoelectric stack. The nominal modulus for Channel Industries 5400 PZT is 65GPa. This error is well within the standard material scatter.

The generalized coupling coefficient of the piezoelectric stack was determined from the phase of the impedance frequency-response, Z(ω) as follows:

$$K_{33}^2 = \left\{\left(\omega_n^{zero}\right)^2 - \left(\omega_n^{pole}\right)^2\right\}\Big/\left(\omega_n^{pole}\right)^2 \tag{71}$$

With a first axial zero frequency, $f_{zero} = 21.7kHz$, the coupling coefficient of the piezoelectric stack is $K_{33} = 0.59$. The published coupling coefficient for 5400 PZT is $K_{33} = 0.71$. The discrepancy between the published and measured coupling coefficients is due to strain energy sharing with the glue layers. The error can also be partially attributed to material property variations.

4.4. COMPONENT EXPERIMENTAL RESULTS SUMMARY

This section presents a brief summary of the experimental results obtained from the techniques described in this chapter. The experimental data and NASTRAN results in table 2, motivated the analysis refinements and new design modifications of chapter 3. The results of these refinements are also presented in the third column of table 2.

Several conclusions can be made from the experimental results of table 2. The component is much stiffer than intended. The two-dimensional finite element model's overestimate of the piezoelectric loss factor can be accounted for by unmodeled flexibility throughout the three-dimensional wire-EDMed part, and/or unmodeled flexibility in the

component tester. It should be noted that the flexibility associated with the flexure-rigid beam interface has been included in the NASTRAN model.

	DATA	NASTRAN	DESIGN #2
K_{sc} $(N/\mu m)$	9.57	9.71	1.50
K_{oc} $(N/\mu m)$	10.66	12.12	2.57
η_{pzt} (%)	21.6	21.6	21.6
η_{comp} (%)	5.4	11.1	13.6

Table 2. Component results summary for the experimental data, the finite element model and the new design.

Design #2, in table 2, includes five important modifications: 1. The lever angle is reduced from 21.8 degrees to 10 degrees to obtain the desired component stiffness of 1.5N/um. 2. Due to the extremely low bending strain energy in the flexures, the flexure lengths are reduced to channel more strain energy in the piezoelectric. 3. The entire lever arm width is doubled to 2cm to increase the flexure's axial stiffness to bending stiffness ratio. 4. The thick semi-rigid beam is also doubled in thickness. 5. The semi-rigid beam is symmetric about the flexures in order to reduce the footprint length from 8.6 to 1.1 times the flexure length as discussed in chapter 3.

The loss factor of the new design in table 2, increases only slightly over the experimental results of the original design, since the damper's potential performance decreases with an increase in the demanded stroke amplification.

In the next chapter the component's damping performance in the testbed is simulated with the experimental component data and the new design values.

CHAPTER 5

SIMULATED FREQUENCY RESPONSE PERFORMANCE FOR ASTREX

Once the piezoelectric material properties have been integrated into the equivalent mechanical model in chapter 1, the piezoelectric-based dampers can be assembled into the larger finite element model of ASTREX. The ASTREX finite element model consists of approximately 900 nodes and 400 elements as seen in figure 50. The frequency response can also be derived from the finite element method.

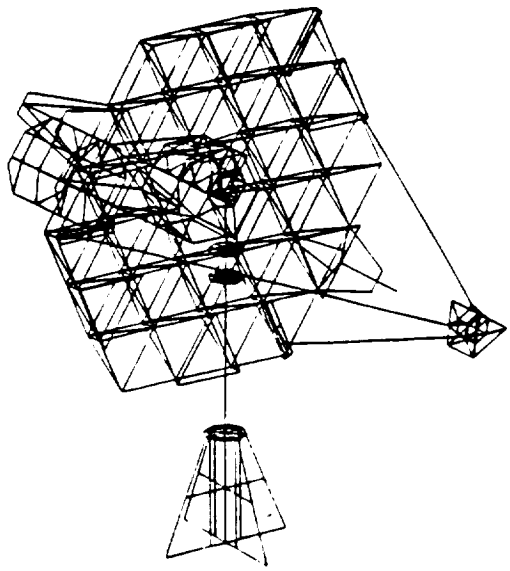

Figure 50. Finite element model of ASTREX.

5.1. FINITE ELEMENT FORMULATION AND SOLUTION ALGORITHMS OF THE DAMPED TESTBED MODEL

The tripod struts are modeled with nine beam elements to accurately capture the third bending mode around 100Hz. The backplane composite struts are each modeled with a single beam element, since the second bending mode at over 150Hz is of no modeling concern. The CROD beam elements have three displacement and three rotational degrees of freedom at each end. Half the composite tube's mass is lumped at each node, in order to produce a diagonal mass matrix.

The six hexagonal steel mirrors are each modeled with six triangular plate elements to fit the shape smoothly without using highly distorted quadrilateral finite elements. The three node triangular elements, CTRIA3 have five degrees of freedom per node. Bending, stretching and twisting are modeled. Since shear deformations are not modeled, large thin plates are used in the model assembly. One quarter of the steel plate's mass is lumped at each node, in order to produce a diagonal mass matrix. Two dimensional CQUAD plate elements were also used to model the steel plates of the tripod apex with minimal element distortion. These quadrilateral elements consist of four adjacent triangular elements with a statically condensed center node.

Rotary and linear dashpots and springs were used to model the airbearing that isolates ASTREX from the dynamics of the support pedestal. Dashpot elements were also used to model piezoelectric implementations as discussed in the previous section. In any event, all damping elements used in this model are one-degree of freedom displacement or rotary dampers that have proportional damping matrices in local coordinates.

After the local stiffness, mass and damping matrices are transformed into the global degrees of freedom of the ASTREX model, the global finite element equations of motion can be assembled as in equation (72).

$$\mathbf{M}\ddot{x} + \mathbf{E}\dot{x} + \mathbf{K}x = f \tag{72}$$

where $\mathbf{M}$, $\mathbf{E}$, and $\mathbf{K}$ are mass, proportional damping, and stiffness matrices, respectively. x is a vector representing generalized deflections (degrees of freedom) of grid points or nodes. An overdot indicates time derivative. The vector f includes forces and moments applied to the structure. The equation can be written in a state-space form as given by

$$\begin{Bmatrix} \dot{x} \\ \ddot{x} \end{Bmatrix} = \begin{bmatrix} 0 & I \\ -\mathbf{M}^{-1}\mathbf{K} & -\mathbf{M}^{-1}\mathbf{E} \end{bmatrix} \begin{Bmatrix} x \\ \dot{x} \end{Bmatrix} + \begin{Bmatrix} 0 \\ \mathbf{M}^{-1}f \end{Bmatrix} \tag{73}$$

such that

$$\dot{X} = AX + F \tag{74}$$

where $X = \begin{Bmatrix} x \\ \dot{x} \end{Bmatrix}$, $A = \begin{bmatrix} 0 & I \\ -\mathbf{M}^{-1}\mathbf{K} & -\mathbf{M}^{-1}\mathbf{E} \end{bmatrix}$ and $F = \begin{Bmatrix} 0 \\ \mathbf{M}^{-1}f \end{Bmatrix}$.

A transformation from physical degrees of freedom (n) to a modal state (m modes) can be made by defining $x = \Phi\eta$; the modal state vector η (m x 1) includes modal amplitudes, and the column of modal matrix Φ is normalized with respect to the mass matrix $\mathbf{M}$ such that $\Phi^T\mathbf{M}\Phi = I$ and $\Phi^T\mathbf{K}\Phi = \Lambda$; I is an identity matrix, and Λ is a diagonal eigenvalue matrix. Using the transformation, and multiplying by Φ^T, equation (72) is given by

$$\Phi^T\mathbf{M}\Phi\ddot{\eta} + \Phi^T\mathbf{E}\Phi\dot{\eta} + \Phi^T\mathbf{K}\Phi\eta = \Phi^T f$$

which from mass-normalization and assuming a proportional damping reduces to

$$I\ddot{\eta} + \left[2\zeta_{diag}\omega_n\right]\dot{\eta} + \Lambda\eta = \Phi^T f \tag{75}$$

In the diagonal modal damping matrix $\left[2\zeta_{diag}\omega_n\right]$, ζ_{diag} is a diagonal modal damping factor matrix with m diagonal entries. The diagonal natural frequency matrix of the structure, ω_n, is the square root matrix of the diagonal matrix, Λ. Taking the Laplace transform of both sides of equation (75) yields

$$\left[Is^2 + \left[2\zeta_{diag}\omega_n\right]s + \Lambda\right]\bar{\eta}(s) = \Phi^T\bar{f}(s).$$

Multiplying both sides by the modal matrix Φ, yields

$$\bar{x}(s) = \Phi\bar{\eta}(s) = \Phi\left[Is^2 + \left[2\zeta_{diag}\omega_n\right]s + \Lambda\right]^{-1}\Phi^T\bar{f}(s).$$

Let each eigenvector i, at the excitation degree of freedom e, be denoted Φ_{ie}. Let each eigenvector i, at the response degree of freedom r, be denoted Φ_{ir}. Since all the matrices are diagonal, the equations are decoupled and the total response is the sum of the responses at each mode. Summing the contribution of each excited mode to the overall response, yields the transfer function equation used to generate the performance plots in chapter 5, and determine peak dynamic component stresses in chapter 2.

$$\bar{x}_r(s) = \sum_i^m \left(\frac{\Phi_{ir}\Phi_{ie}^T}{s^2 + \left[2(\zeta_{diag})_i\omega_i\right]s + \Lambda_i} \right) \bar{f}_e(s) \tag{76}$$

where, $$(\zeta_{diag})_i \cong \frac{1}{2}(\eta)_i = \frac{1}{2}\left(\eta_{piezo}\frac{U_{piezo}}{U_{total}} \right)_i$$

The influence of passive damping, as mentioned earlier does not end with maximizing ζ_{diag} at a target ω such that the spacecraft's response is minimized. In fact, any passive

damping implementation must be reported to the controls engineer for updating the control equations. The modal damping factors of the manufactured damping device (See chapters 3 and 4) were carried through the following matrix manipulations to update the control matrices for the control engineer responsible for designing a control system that rolls off at a frequency of high passive damping.

The equation (75) can be written in a state space form as follows.

$$\begin{Bmatrix} \dot{\eta} \\ \ddot{\eta} \end{Bmatrix} = \begin{bmatrix} 0 & I \\ -\Lambda & -\left[2\zeta_{\omega_n}\omega_n\right] \end{bmatrix} \begin{Bmatrix} \eta \\ \dot{\eta} \end{Bmatrix} + \begin{Bmatrix} 0 \\ \Phi^T f \end{Bmatrix} \tag{77}$$

In compact notation, $$\dot{X}_\eta = A_\eta X_\eta + F_\eta \tag{78}$$

where $X_\eta = \begin{Bmatrix} \eta \\ \dot{\eta} \end{Bmatrix}$, $A_\eta = \begin{bmatrix} 0 & I \\ -\Lambda & -\left[2\zeta_{\omega_n}\omega_n\right] \end{bmatrix}$ and $F_\eta = \begin{Bmatrix} 0 \\ \Phi^T f \end{Bmatrix}$. Due to the fullness of the modal matrix Φ, a force on the structure, theoretically, affects all modal states.

The participation of a force or moment, applied in certain direction on the structure, in the modal state form can be explained as follows. Let the generalized displacement vector be written as $x = \{U, V, W, \psi, \theta, \phi\}^T$, where U, V, W are the displacement vectors along local x, y, z coordinates, and ψ, θ, ϕ are the slope vectors about the coordinates, respectively; each vector has dimension equal to number of nodes (numnodes x 1). The modal matrix Φ corresponds to this particular arrangement of the generalized displacement vector x. If a force is applied at location j in the local z direction, the force vector f *is given by*

$$f = \begin{Bmatrix} 0 \\ 0 \\ \vdots \\ 0 \\ f_{w_j} \\ \vdots \\ 0 \\ 0 \end{Bmatrix} \tag{79}$$

The number of zeros in the top of equation (79) equal to 2*numnodes + j - 1, and in the bottom equal to 6*numnodes - {2*numnodes + j}. This can also be written as a unit vector with all zeros except at the location of z direction at j node, multiplied by the

magnitude f_{ω_j}. Symbolically, it is written as $f_{\omega_j} = S_{uv_{\omega}} \left| f_{\omega_j} \right|$. This representation helps in relating F_η to applied force directly.

$$F_\eta = \begin{Bmatrix} 0 \\ \Phi^T S_{uv_{\omega}} \end{Bmatrix} f_{\omega_j}$$

Thus only the $\{\omega j\}$ displacement contribution of the modal matrix Φ is effective. For multiple force and moment inputs at different location or in different direction, a summation is carried out with appropriate placement unit vector:

$$F_\eta = \left\{ \begin{matrix} 0 \\ \Phi^T \Sigma_j \Sigma_d \left[S_{uv_{dj}} \cdot f_{d_j} \right] \end{matrix} \right\}$$

where d signifies the degree of freedom at node j. Effectively, a unit column-vector matrix is created leading to equation,

$$F_\eta = \begin{bmatrix} 0 \\ \Phi^T S_{uvmat_{dj}} \end{bmatrix} u = B_\eta u \tag{80}$$

in which u is the actual control input vector (non-zero terms in f of equation (72)), *uvmat* indicates that a matrix having unit vectors as columns is generated, and B_η is the control input matrix in the modal form. The force vector

$$F = \begin{bmatrix} 0 & 0 \\ 0 & M^{-1}\Phi^{-T} \end{bmatrix} F_\eta = \begin{bmatrix} 0 & 0 \\ 0 & \Phi \end{bmatrix} B_\eta u = Bu \tag{81}$$

In this equation, B is the influence matrix which could also be formulated from equation (79).

The output equation is given by $y = ax + b\dot{x} + c\ddot{x}$. The a, b, c matrices provide the combination of displacement, velocity, and acceleration output from the sensors. The equation can be written as

$$y = [a \quad b] \begin{Bmatrix} x \\ \dot{x} \end{Bmatrix} + [0 \quad c] \begin{Bmatrix} \dot{x} \\ \ddot{x} \end{Bmatrix}$$

$$y = [a \quad b] X + [0 \quad c][AX + F]$$

Using the transformation relation

$$A \begin{bmatrix} \Phi & 0 \\ 0 & \Phi \end{bmatrix} = \begin{bmatrix} \Phi & 0 \\ 0 & \Phi \end{bmatrix} A_\eta$$

and substituting for X, the output equation can be written in the modal form as

$$y = \left\{ (a\Phi - c\Phi\Lambda) \quad (b\Phi - c\Phi\zeta_{mat}) \right\} \begin{Bmatrix} \eta \\ \dot{\eta} \end{Bmatrix} + [0 \quad c]F$$

$$y = \left\{ (a\Phi - c\Phi\Lambda) \quad (b\Phi - c\Phi\zeta_{mat}) \right\} \begin{Bmatrix} \eta \\ \dot{\eta} \end{Bmatrix} + c\Phi B_\eta u$$

$$y = C_\eta X_\eta + D_\eta u \tag{82}$$

This equation is used to obtain response of the system. In summary, control system matrices are rewritten:

$$A_\eta = \begin{bmatrix} 0 & I \\ -\Lambda & -\zeta_{mat} \end{bmatrix}, \; B_\eta = \begin{Bmatrix} 0 \\ \Phi^T S_{uumat_{ij}} \end{Bmatrix}$$

$$C_\eta = \left\{ (a\Phi - c\Phi\Lambda) \quad (b\Phi - c\Phi\zeta_{mat}) \right\}, \; D_\eta = c\Phi B_\eta. \tag{83}$$

A compact form (quadruple) is generated by placing these matrices in a system matrix,

$$S_\eta = \begin{bmatrix} A_\eta & B_\eta \\ C_\eta & D_\eta \end{bmatrix}. \tag{84}$$

These are the matrices used in state space control system design. Notice that the passive damping implementation will show up as two non-negligible damping terms: one on the A_η matrix diagonal, and one term from the C_η matrix. This makes the controls engineers goal of inverting the plant a more realistic objective.

5.2. LINE-OF-SIGHT PERFORMANCE TRANSFER FUNCTIONS

The effect upon the plant transfer function (from control actuator to error sensor) of inserting a six-axis isolation stage to support the payload at the secondary mirror, is simulated in figure 51, using experimentally measured component characteristics. This simulation employs a NASTRAN dynamic model of the ASTREX structure. This model has not been tuned with a modal survey. The results are thus at best representative, and certainly not trustworthy in detail. A control engineer, faced with these two plants, will be happy with neither, but would certainly prefer to compensate the damped plant.

The solid trace in figures 51, 52 and 53 represents the predicted damping effect of the six-axis vibration absorber with resistively-shunted piezoelectric damping (R = 360kΩ). When the vibration absorber's proof mass is rigidly mounted to the structure, the undamped effect is predicted by the dash trace in figures 51, 52 and 53. When the

piezoelectric stacks are shunted with zero resistance, the short-circuit effect is predicted by the dash-dot trace in figures 51, 52, and 53.

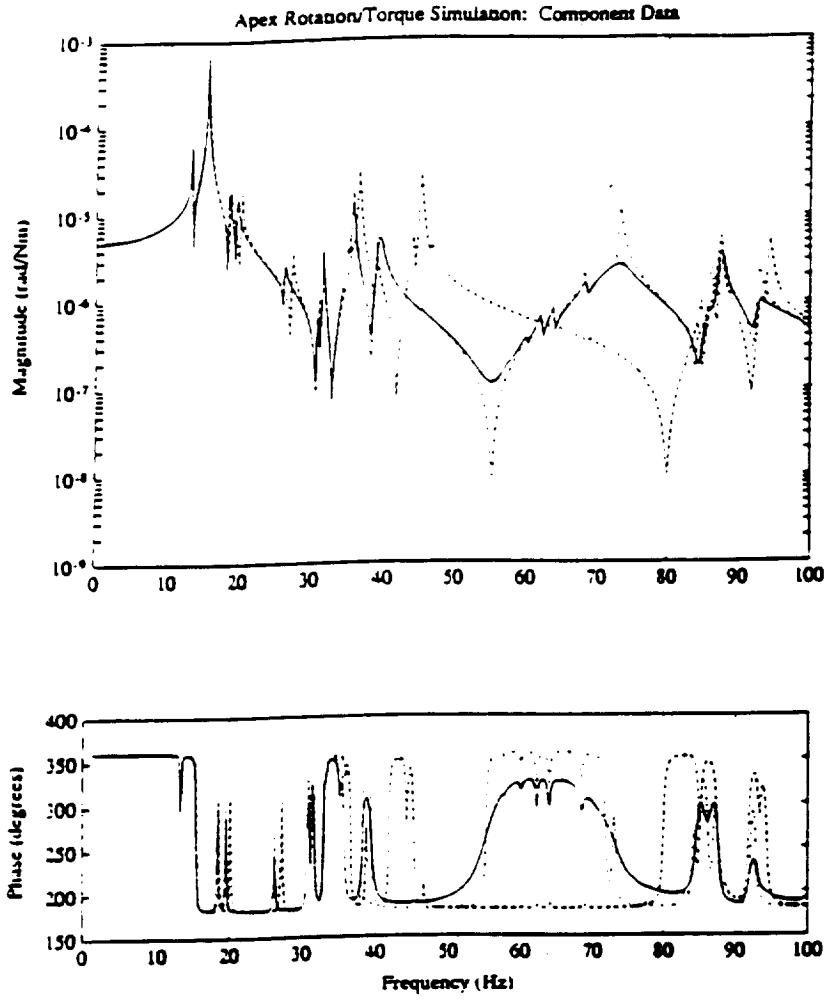

Figure 51. ASTREX simulation using experimental stiffness and damping data of the component. The solid trace shows the damping performance of the six-axis vibration absorber with resistively-shunted piezoelectric damping (R = 360kΩ). The dash trace represents the undamped dynamics with the vibration absorber's proof mass mounted rigidly to the structure. The dash-dot trace represents the undamped dynamics of the structure with short-circuit piezoelectrics.

The effect upon the plant transfer function (from control actuator to error sensor) of inserting a six-axis isolation stage to support the payload at the secondary mirror, is simulated in figure 52, using the new design component properties described in chapter 3. The design modifications are summarized as follows: 1. The lever angle is halved to obtain

the desired component stiffness of 1.5N/um. 2. Due to the extremely low bending strain energy in the flexures, the flexure lengths are halved to channel more strain energy in the piezoelectric. 3. The entire lever arm width is doubled to 2cm to increase the flexure's axial stiffness to bending stiffness ratio. 4. The thick semi-rigid beam is also doubled in thickness. 5. The semi-rigid beam is symmetric about the flexures in order to reduce the footprint length from 8.6 to 1.1 times the flexure length as discussed in chapter 3.

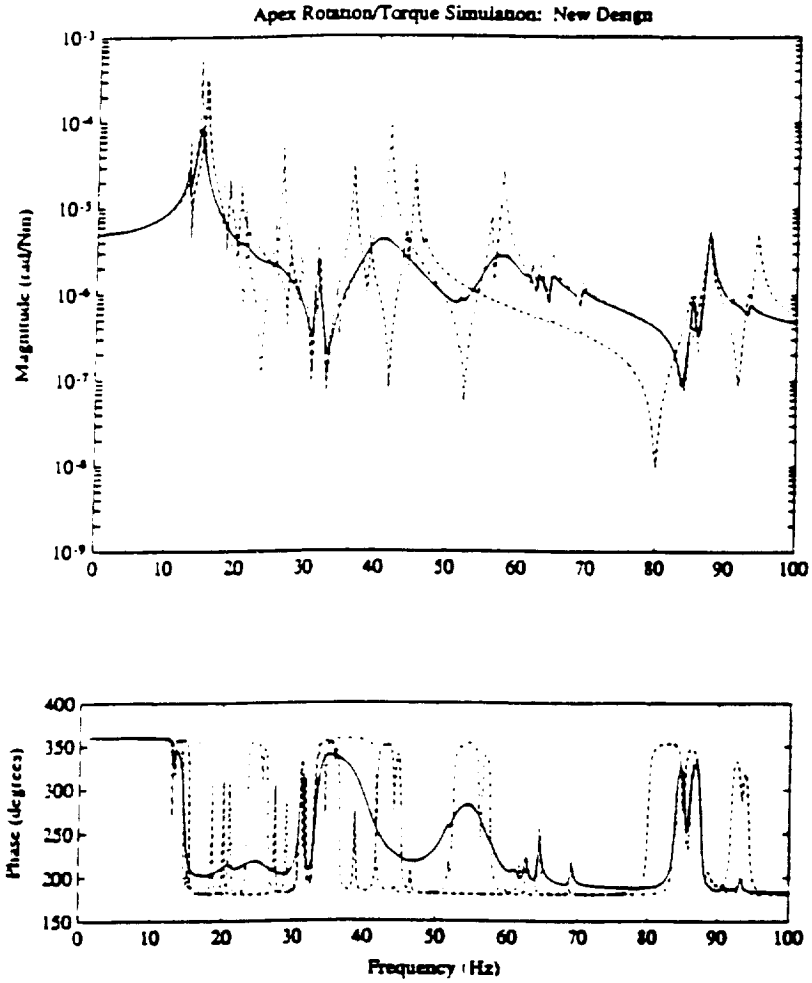

Figure 52. ASTREX simulation using new design stiffness and damping values of the component. The solid trace shows the damping performance of the six-axis vibration absorber with resistively-shunted piezoelectric damping (R = 360kΩ). The dash trace represents the undamped dynamics with the vibration absorber's proof mass mounted rigidly to the structure. The dash-dot trace represents the undamped dynamics of the structure with short-circuit piezoelectrics.

5.3. ISOLATION SYSTEM PERFORMANCE TRANSFER FUNCTION

An alternate use of the six-axis stage is for isolation; it is possible to isolate the control system from unpleasant structural dynamics of the ASTREX structure. This is summarized in figure 53, in which the actuator torque is applied not to the tripod apex but to the 90kg. suspended mass that is presumably supporting the secondary optics. In this plant, the isolation properties of the six-axis stage lead to very clean plant dynamics above 40Hz, and would permit robust closed-loop control.

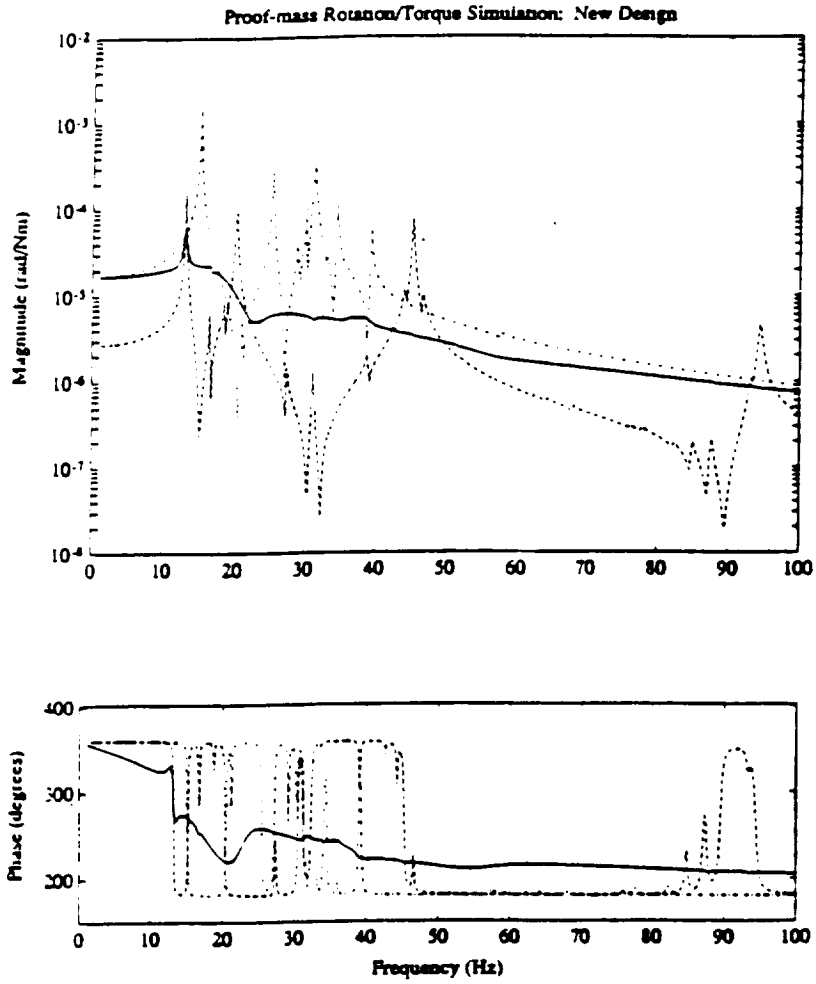

Figure 53. ASTREX simulation using the new design stiffness and damping values of the component. The solid trace shows the damping performance of the six-axis vibration absorber with resistively-shunted piezoelectric damping (R = 360kΩ). The dash trace represents the undamped dynamics with the vibration absorber's proof mass mounted rigidly to the structure. The dash-dot trace represents the undamped dynamics of the structure with short-circuit piezoelectrics.

CHAPTER 6.

CONCLUSIONS AND RECOMMENDATIONS

Passive damping is important for space structure performance and controller stability robustness requirements. The ability of resistively-shunted piezoelectric damping to meet these requirements was investigated. A summary of contemporary passive damping implementations for large space structures was presented. This paper has presented the piezoelectric passive damping modeling approach and its modifications for finite element software implementation. The dynamic behavior and passive damping needs of the ASTREX testbed were addressed with a comparison of two potential damping design options: the piezoelectric joint and the tuned piezoelectric vibration absorber. The latter design was designed, manufactured and tested at the component level.

An analytical truss model was developed for the vibration absorber components. The model was used iteratively to optimize the lever ratio and piezoelectric strain energy of the component with respect to dimensional requirements and desired design features. A finite element model of the component was used to verify the design and to ensure stress limits were not exceeded.

The finite element model was also used to generate design curves that depict the optimal flexure dimensions that maximize the piezoelectric strain energy subject to stiffness, stress and manufacturing limitations. Several trends were noted from these design curves. The effective stiffness curves illustrated that longer and thinner flexures decrease the effective stiffness and stubby flexures increase the effective stiffness. The stiffness curve is relatively constant for the middle flexure values where the transition from axially-dominated to bending-dominated flexure properties occurs. This transition zone is also where the

piezoelectric strain energy is maximized. The strain-energy curve for small flexure dimensions that approach zero is analogous to the narrowband damping provided by resonant LRC circuit piezoelectric damping. Just as the peak damping is largest over the small range of frequencies influenced by the resonant circuit, so also is the strain energy of piezoelectric maximized over a more limited range of flexure thicknesses. The virtues of the strain-energy curve for large flexure dimensions is analogous to those provided by the broadband damping of resistive RC circuit piezoelectric shunting: both are insensitive to minor parameter variations, frequency and flexure thickness, respectively. Piezoelectric stress plots illustrated that the amount of applied load that reaches the piezoelectric decreases with increasing flexure bending stiffness. Flexure stress curves illustrate that stress is conveniently minimized when piezoelectric strain energy is maximized. Axial stresses and bending stresses increase as the curve shifts to the left and the right, respectively. One important limitation to a small-flexure, high-performance component design, is ensuring that the stress in the flexure does not exceed the yield and fatigue stress limits. The EDM technique also excludes small flexure designs from the manufacturable design space of the component.

A local elasticity analysis of the beam/flexure interface was made to include the lever's "footprint" flexibility in the component models. The results of this study, motivated a new design that used the original design as a starting point. A trial and error procedure was conducted to illustrate how the new design was found from the original component properties.

Test results indicate that it is challenging to channel a large fraction of the structural strain energy into the piezoceramic material without sacrificing some strain energy to residual parallel and series non-piezoelectric stiffnesses. Despite this discrepancy in component performance, the first-order stiffness change and bell-shaped loss factor curve were verified as predicted.

This report has addressed some of the practical considerations encountered when attempting piezoceramic passive damping of a large flexible structure. The report presents a first-iteration solution to these problems. Future work will use this as a starting point.

Another interesting topic that requires interesting research is developing a magnetostrictive actuator. The actuator/damper would not require a new flex-tensional component as the piezoelectric and magnetostrictive share similar material properties. The potential advantage of magnetostrictive damping is its ability to absorb strain energy without the glue-layer strain energy sharing problem inherent to piezoelectric stacks. The potential disadvantages need investigation. For example, the number of required coils wraped about the magnetostrictive must be numerous enough to efficiently transform the

magnetic field into an induced current. Commanded current sources could make the stack too bulky for practical steel flex-tensional design. Fortunately, a magnetic field source could be supplied by magnets that would replace the shims in the piezoelectric design. The return path of the magnetic flux could also be conveniently channeled through the effective "arc-bridge" provided by the eight lever arm pairs.

The effectiveness of this design would also be dependent on finding or developing a low-stiffness, high-magnetic conductivity material (ideally, identical to steel in terms of magnetic conductivity) to fill the "dogbone" shapes cut out of the steel during lever arm manufacturing. Without such an implementation, the returning magnetic flux path would be forced to arc across the thin flexures.

APPENDIX I

ANALYTICAL FINITE ELEMENT COMPONENT MODEL

An analytical finite element model was constructed to study the effects of bending and axial/bending coupling that are not present in the analytical truss model. This appendix attempts to provide a more accurate, but less elegant, analytical model with all the important bending and axial/bending terms included. This appendix begins where the NASTRAN component model section of chapter 3 leaves off.

The finite element model of the component, shown again in figure 54 below, is now ready to be assembled with linear springs (one for the piezoelectric and one for the preload springs) and six-degree-of-freedom slender beam elements (one for the semirigid beam and two for the flexures).

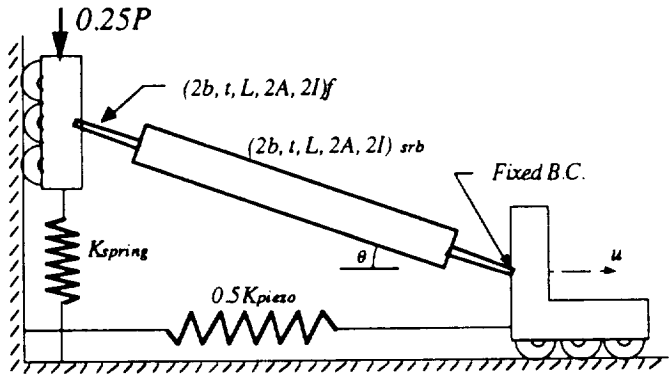

Figure 54. The one-eighth model with combined lever arm properties.

The first task is to assemble three beam elements together as depicted in figure 55.

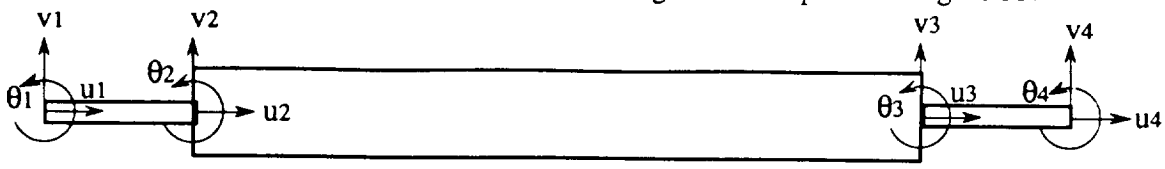

Figure 55. 12 degree-of-freedom lever arm in local coordinate system.

The slender beam element equations for the flexure on the left of figure 55 are written in matrix form:

$$\begin{bmatrix} F_1^x \\ F_1^y \\ M_1 \\ F_2^x \\ F_2^y \\ M_2 \end{bmatrix} = \begin{bmatrix} \frac{2EA_f}{L_f} & 0 & 0 & \frac{-2EA_f}{L_f} & 0 & 0 \\ 0 & \frac{24EI_f}{L_f^3} & \frac{-12EI_f}{L_f^2} & 0 & \frac{-24EI_f}{L_f^3} & \frac{-12EI_f}{L_f^2} \\ 0 & \frac{-12EI_f}{L_f^2} & \frac{8EI_f}{L_f} & 0 & \frac{12EI_f}{L_f^2} & \frac{4EI_f}{L_f} \\ \frac{-2EI_f}{L_f} & 0 & 0 & \frac{2EI_f}{L_f} & 0 & 0 \\ 0 & \frac{-24EI_f}{L_f^3} & \frac{12EI_f}{L_f^2} & 0 & \frac{24EI_f}{L_f^3} & \frac{12EI_f}{L_f^2} \\ 0 & \frac{-12EI_f}{L_f^2} & \frac{4EI_f}{L_f} & 0 & \frac{12EI_f}{L_f^2} & \frac{8EI_f}{L_f} \end{bmatrix} \begin{bmatrix} u_1 \\ v_1 \\ \theta_1 \\ u_2 \\ v_2 \\ \theta_2 \end{bmatrix} \tag{85}$$

This stiffness matrix is identical to the stiffness matrix of the flexure on the right. Substituting the semirigid beam properties into the matrix above yields the center beam element's stiffness matrix.

In order to see how the larger global stiffness matrices are assembled and manipulated throughout the rest of this section, dummy alphabet variables will be used to represent the stiffness matrix elements. The stiffness matrices are now represented as

$$K_1 = K_3 = \begin{bmatrix} aa & & & ad & & \\ & bb & bc & & be & bf \\ & cb & cc & & ce & cf \\ da & & & dd & & \\ & eb & ec & & ee & ef \\ & fb & fc & & fe & ff \end{bmatrix} \tag{86}$$

$$K_2 = \begin{bmatrix} AA & & & AD & & \\ & BB & BC & & BE & BF \\ & CB & CC & & CE & CF \\ DA & & & DD & & \\ & EB & EC & & EE & EF \\ & FB & FC & & FE & FF \end{bmatrix} \tag{87}$$

When these matrices and the corresponding semirigid beam stiffness matrix are assembled into the global stiffness matrix in local coordinates, a 12 by 12 matrix is constructed

$$\begin{bmatrix} F_1^x \\ F_1^y \\ M_1 \\ F_2^x \\ F_2^y \\ M_2 \\ F_3^x \\ F_3^y \\ M_3 \\ F_4^x \\ F_4^y \\ M_4 \end{bmatrix} = \begin{bmatrix} aa & & & ad & & & & & & & & \\ & bb & bc & & be & bf & & & & & & \\ & cb & cc & & ce & cf & & & & & & \\ da & & & dd + AA & & & AD & & & & & \\ & eb & ec & & ee + BB & ef + BC & & BE & BF & & & \\ & fb & fc & & fe + CB & ff + CC & & CE & CF & & & \\ & & & DA & & & aa + DD & & & ad & & \\ & & & & EB & EC & & bb + EE & bc + EF & & be & bf \\ & & & & FB & FC & & cb + FE & cc + FF & & ce & cf \\ & & & & & & da & & & dd & & \\ & & & & & & & eb & ec & & ee & ef \\ & & & & & & & fb & fc & & fe & ff \end{bmatrix} \begin{bmatrix} u_1 \\ v_1 \\ \theta_1 \\ u_2 \\ v_2 \\ \theta_2 \\ u_3 \\ v_3 \\ \theta_3 \\ u_4 \\ v_4 \\ \theta_4 \end{bmatrix} \tag{88}$$

Four boundary conditions can be applied to reduce the number of equations and unknowns from twelve to eight. Two of them, $\theta_1 = 0$ and $\theta_4 = 0$, can be directly applied to equation (88) to reduce the number of equations and unknowns to ten.

$$\begin{bmatrix} F_1^x \\ F_1^y \\ F_2^x \\ F_2^y \\ M_2 \\ F_3^x \\ F_3^y \\ M_3 \\ F_4^x \\ F_4^y \end{bmatrix} = \begin{bmatrix} aa & & ad & & & & & & & \\ & bb & & be & bf & & & & & \\ da & & dd+AA & & & AD & & & & \\ & eb & & ee+BB & ef+BC & & BE & BF & & \\ & fb & & fe+CB & ff+CC & & CE & CF & & \\ & & DA & & & aa+DD & & & ad & \\ & & & EB & EC & & bb+EE & bc+EF & & be \\ & & & FB & FC & & cb+FE & cc+FF & & ce \\ & & & & & da & & & dd & \\ & & & & & & eb & ec & & ee \end{bmatrix} \begin{bmatrix} u_1 \\ v_1 \\ u_2 \\ v_2 \\ \theta_2 \\ u_3 \\ v_3 \\ \theta_3 \\ u_4 \\ v_4 \end{bmatrix} \tag{89}$$

$$\{F\}_{xy} = [K]_{xy}\{u\}_{xy}$$

The remaining two boundary conditions must be applied after the local degrees of freedom of node one and four are transformed to the global coordinate system as in figure 56.

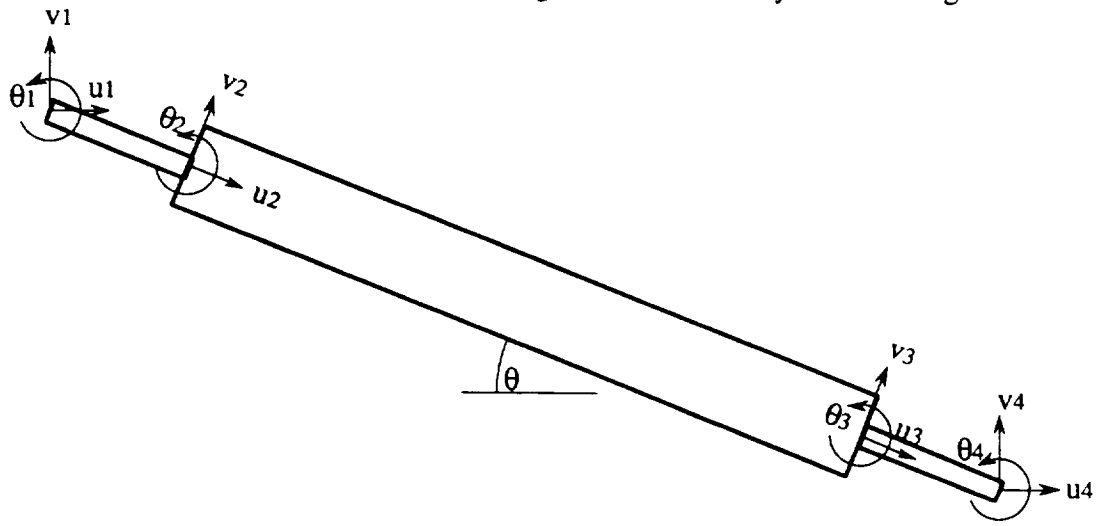

Figure 56. Degree's of freedom at nodes one and four are transformed into the global coordinate system.

Transformation matrices are used to transform the degrees of freedom of nodes one and four to the global coordinate system. Both the force vector and the displacement vector need to be transformed with the transformation matrix

$$[A_1] = \begin{bmatrix} [A_0] & & & \\ & 1 & & \\ & & \ddots & \\ & & & 1 \\ & & & & [A_0] \end{bmatrix} \tag{90}$$

where $$[A_0] = \begin{bmatrix} \cos\theta & \sin\theta \\ -\sin\theta & \cos\theta \end{bmatrix}.$$

The force vector in Equation (89) is transformed as follows:

$$\{F\}_{xy} = [K]_{xy}\{u\}_{xy}$$

$$\{F\}_{XY} = [A_1]\{F\}_{xy}$$

$$\{F\}_{XY} = [A_1][K]_{xy}\{u\}_{xy} \tag{91}$$

The displacement vector in Equation (89) is transformed as follows:

$$\{u\}_{XY} = [A_1]\{u\}_{xy}$$

$$\{u\}_{xy} = [A_1]^{-1}\{u\}_{XY} = [A_1]^T\{u\}_{XY} \tag{92}$$

Equation (91) and (92) are combined to find the new global stiffness

$$\{F\}_{XY} = [A_1][K]_{xy}[A_1]^T\{u\}_{XY}$$

$$\{K\}_{XY} = [A_1][K]_{xy}[A_1]^T \tag{93}$$

The resulting global stiffness matrix has the following matrix structure, where the constants indicate non-zero elements.

$$\begin{bmatrix} F_1^X \\ F_1^Y \\ F_2^x \\ F_2^y \\ M_2 \\ F_3^x \\ F_3^y \\ M_3 \\ F_4^X \\ F_4^Y \end{bmatrix} = \begin{bmatrix} a1 & a2 & a3 & a4 & a5 & & & & & \\ b1 & b2 & b3 & b4 & b5 & & & & & \\ c1 & c2 & c3 & & & c6 & & & & \\ d1 & d2 & & d4 & d5 & & d7 & d8 & & \\ e1 & e2 & & e4 & e5 & & e7 & e8 & & \\ & & f3 & & & f6 & & & f9 & f10 \\ & & & g4 & g5 & & g7 & g8 & g9 & g10 \\ & & & h4 & h5 & & h7 & h8 & h9 & h10 \\ & & & & & i6 & i7 & i8 & i9 & i10 \\ & & & & & j6 & j7 & j8 & j9 & j10 \end{bmatrix} \begin{bmatrix} U_1 \\ V_1 \\ u_2 \\ v_2 \\ \theta_2 \\ u_3 \\ v_3 \\ \theta_3 \\ U_4 \\ V_4 \end{bmatrix} \tag{94}$$

Applying the remaining two boundary conditions, $U_1 = 0$ and $V_4 = 0$ yields an eight by eight matrix

$$\begin{bmatrix} F_1^Y \\ F_2^x \\ F_2^y \\ M_2 \\ F_3^x \\ F_3^y \\ M_3 \\ F_4^X \end{bmatrix} = \begin{bmatrix} b2 & b3 & b4 & b5 & & & & \\ c2 & c3 & & & c6 & & & \\ d2 & & d4 & d5 & & d7 & d8 & \\ e2 & & e4 & e5 & & e7 & e8 & \\ & f3 & & & f6 & & & f9 \\ & & g4 & g5 & & g7 & g8 & g9 \\ & & h4 & h5 & & h7 & h8 & h9 \\ & & & & i6 & i7 & i8 & i9 \end{bmatrix} \begin{bmatrix} V_1 \\ u_2 \\ v_2 \\ \theta_2 \\ u_3 \\ v_3 \\ \theta_3 \\ U_4 \end{bmatrix} \tag{95}$$

Equation (95) describes the eighth model below

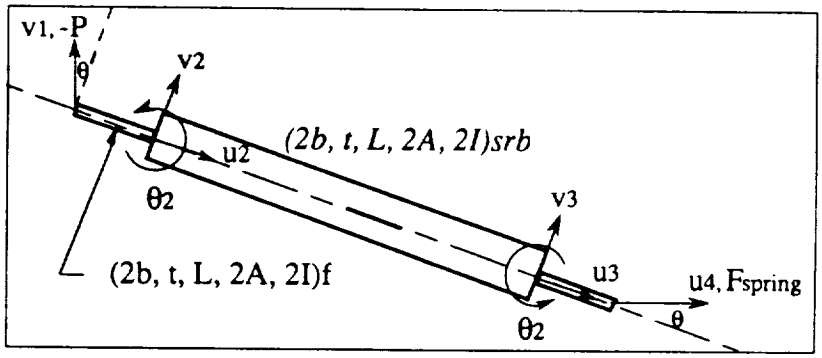

Figure 57. The one-eighth model with combined lever arm properties and eight remaining beam element degrees of freedom.

Since U_4 and V_1 are the only degrees of freedom needed to calculate the effective stiffness of the component and the percent strain energy in the piezoelectric, the other degrees of freedom can be statically condensed out of the global stiffness matrix. The first step is to rearrange the matrix equations into a form suitable for static condensation. The following matrix has maintained its symmetry since each row exchange is followed by a column exchange.

$$\left[\begin{array}{c} P/4 \\ \hline 0 \\ 0 \\ 0 \\ 0 \\ 0 \\ 0 \\ 0 \end{array}\right] = \left[\begin{array}{cc|cccccc} b2 & & b3 & & b4 & & b5 & \\ & i9 & & i6 & & i7 & & i8 \\ \hline c2 & & c3 & c6 & & & & \\ & f9 & f3 & f6 & & & & \\ d2 & & & & d4 & d7 & d5 & d8 \\ & g9 & & & g4 & g7 & g5 & g8 \\ e2 & & & & e4 & e7 & e5 & e8 \\ & h9 & & & h4 & h7 & h5 & h8 \end{array}\right] \left[\begin{array}{c} V_1 \\ U_4 \\ \hline u_2 \\ u_3 \\ v_2 \\ v_3 \\ \theta_2 \\ \theta_3 \end{array}\right] \tag{96}$$

Static condensation will involve inversion of the six by six submatrix, which is actually a 2 by 2 inversion and a 4 by 4 inversion combined. Since $\theta_3 = \theta_2$ as noticed in the deflected shape and NASTRAN output, it is advantageous to add the elements of the eighth column to the elements of the seventh column to reduce the matrix to a 7 by 7 and reduce the maximum submatrix inversion to a 3 by 3 (Computationally, this inverse is an order of magnitude less difficult.) Note that the new redundant eighth equation must be added to the seventh equation in order to maintain symmetry within the matrix.

$$\left[\begin{array}{c} P/4 \\ \hline 0 \\ 0 \\ 0 \\ 0 \\ 0 \\ 0 \end{array}\right] = \left[\begin{array}{cc|ccccc} b2 & & b3 & & b4 & & b5 \\ & i9 & & i6 & & i7 & i8 \\ \hline c2 & & c3 & c6 & & & \\ & f9 & f3 & f6 & & & \\ d2 & & & & d4 & d7 & (d5+d8) \\ & g9 & & & g4 & g7 & (g5+g8) \\ e2 & h9 & & & (e4+h4) & (e7+h7) & \begin{pmatrix} e5+e8+ \\ h5+h8 \end{pmatrix} \end{array}\right] \left[\begin{array}{c} V_1 \\ U_4 \\ \hline u_2 \\ u_3 \\ v_2 \\ v_3 \\ \theta_2 \end{array}\right] \tag{97}$$

These equations have the block matrix form described in (98).

$$\left[\begin{array}{c} R_a \\ \hline 0 \end{array}\right] = \left[\begin{array}{c|c} K_{aa} & K_{ac} \\ \hline K_{ca} & K_{cc} \end{array}\right] \left[\begin{array}{c} U_a \\ \hline U_c \end{array}\right] \tag{98}$$

where $R_a = P/4$, and

$$K_{aa} = \begin{bmatrix} \left(+\frac{2EA_f}{L_f}(s\theta)^2 + \frac{24EI_f}{L_f^3}(c\theta)^2 + K_{spring} \right) & 0 \\ 0 & \left(+\frac{2EA_f}{L_f}(c\theta)^2 + \frac{24EI_f}{L_f^3}(s\theta)^2 + 0.5(K_{piezo}) \right) \end{bmatrix}$$

$$K_{ac} = \begin{bmatrix} \frac{2EA_f}{L_f}(s\theta) & \frac{-24EI_f}{L_f^3}(c\theta) & \frac{-12EI_f}{L_f^2}(c\theta) \\ \frac{-2EA_f}{L_f}(c\theta) & \frac{-24EI_f}{L_f^3}(s\theta) & \frac{12EI_f}{L_f^2}(s\theta) \end{bmatrix}$$

$$K_{cc} = \left[\begin{array}{c|c} K_{2x2} & 0 \\ \hline 0 & K_{3x3} \end{array}\right]$$

$$K_{2x2} = \begin{bmatrix} \left(\frac{2EA_f}{L_f} + \frac{2EA_{srb}}{L_{srb}} \right) & \frac{-2EA_{srb}}{L_{srb}} \\ SYM. & \left(\frac{2EA_f}{L_f} + \frac{2EA_{srb}}{L_{srb}} \right) \end{bmatrix} = \begin{bmatrix} y & z \\ z & y \end{bmatrix} \tag{99}$$

$$K_{3x3} = \begin{bmatrix} \left(\frac{24EI_f}{L_f^3} + \frac{24EI_{srb}}{L_{srb}^3} \right) & \frac{-24EI_{srb}}{L_{srb}^3} & \left(\frac{12EI_f}{L_f^2} + \frac{-24EI_{srb}}{L_{srb}^2} \right) \\ & \left(\frac{24EI_f}{L_f^3} + \frac{24EI_{srb}}{L_{srb}^3} \right) & \left(\frac{-12EI_f}{L_f^2} + \frac{24EI_{srb}}{L_{srb}^2} \right) \\ SYM. & & \left(\frac{16EI_f}{L_f} + \frac{24EI_{srb}}{L_{srb}} \right) \end{bmatrix} = \begin{bmatrix} p & q & r \\ q & p & -r \\ r & -r & s \end{bmatrix}.$$

Retaining the U_a displacement vector and condensing the U_c displacement vector yields

$$U_c = -K_{cc}^{-1} K_{ca} U_a$$

$$\left(K_{aa} - K_{ac}K_{cc}^{-1}K_{ca}\right)U_a = R_a \tag{100}$$

Inversion of K_{cc}, consists of two decoupled inversions:

$$K_{cc}^{-1} = \left[\begin{array}{c|c} K_{2x2}^{-1} & 0 \\ \hline 0 & K_{3x3}^{-1} \end{array}\right]$$

$$K_{2x2}^{-1} = \frac{1}{y^2 - z^2}\begin{bmatrix} y & -z \\ -z & y \end{bmatrix}$$

$$K_{3x3}^{-1} = \begin{bmatrix} \left(\frac{ps - r^2}{p^2s - 2pr^2 - q^2s - 2qr^2}\right) & \left(\frac{-qs - r^2}{p^2s - 2pr^2 - q^2s - 2qr^2}\right) & \left(\frac{-r}{ps - 2r^2 - qs}\right) \\ & \left(\frac{ps - r^2}{p^2s - 2pr^2 - q^2s - 2qr^2}\right) & \left(\frac{r}{ps - 2r^2 - qs}\right) \\ SYM. & & \left(\frac{p - q}{ps - 2r^2 - qs}\right) \end{bmatrix}$$

It is now evident that if $K_{3x3}$is not simplified or constrained, the inversion and subsequent matrix multiplications will yield hundreds of stiffness terms of little analytical value. This was verified with the MAPLE matrix manipulation software. Equations (99) and (100) are modified with the following three changes in an attempt to bring out the important terms while eliminating negligible ones.

1. Multiply the seven matrix equations by the semi-rigid beam bending flexibility:

$$\left(\frac{24EI_{srb}}{L_{srb}^3}\right)^{-1}.$$

2. Substitute beam properties:

$$A_f = b_f t_f,\ I_f = \frac{1}{12}b_f t_f^3,\ A_{srb} = b_{srb}t_{srb},\ I_{srb} = \frac{1}{12}b_{srb}t_{srb}^3.$$

3. Define flexure to semi-rigid beam bending stiffness ratio, β.

$$\beta = \frac{\frac{24EI_f}{L_f^3}}{\frac{24EI_{srb}}{L_{srb}^3}} = \frac{I_f L_{srb}^3}{L_f^3 I_{srb}} = \left(\frac{\frac{t_f}{L_f}}{\frac{t_{srb}}{L_{srb}}}\right)^3 = \left(\frac{\alpha_f}{\alpha_{srb}}\right)^3 \tag{101}$$

where α's represents the "aspect ratios" of the beams.

These modifications yield the following new matrices:

$$R_a = \begin{bmatrix} \left(\frac{P}{8Eb\alpha_{srb}^3}\right) \\ 0 \end{bmatrix}$$

$$K_{aa} = \begin{bmatrix} \left(\frac{1}{\alpha_{srb}^3}\left(\frac{K_{spring}}{2Eb} + \alpha_f(s\theta)^2 + \alpha_f^2(c\theta)^2\right)\right) & 0 \\ 0 & \left(\frac{1}{\alpha_{srb}^3}\left(\frac{K_{piezo}}{4Eb} + \alpha_f(c\theta)^2 + \alpha_f^2(s\theta)^2\right)\right) \end{bmatrix}$$

$$K_{ac} = \begin{bmatrix} \frac{\alpha_f}{\alpha_{srb}^3}(s\theta) & 0 & \left(\frac{\alpha_f}{\alpha_{srb}}\right)^3(-c\theta) & 0 & \frac{L_f}{2}\left(\frac{\alpha_f}{\alpha_{srb}}\right)^3(-c\theta) \\ 0 & \frac{\alpha_f}{\alpha_{srb}^3}(-c\theta) & 0 & \left(\frac{\alpha_f}{\alpha_{srb}}\right)^3(s\theta) & \frac{L_f}{2}\left(\frac{\alpha_f}{\alpha_{srb}}\right)^3(s\theta) \end{bmatrix}$$

$$K_{2x2} = \begin{bmatrix} \frac{\alpha_f}{\alpha_{srb}^3}\left(1 + \frac{\alpha_{srb}}{\alpha_f}\right) & \frac{-1}{\alpha_{srb}^2} \\ SYM. & \frac{\alpha_f}{\alpha_{srb}^3}\left(1 + \frac{\alpha_{srb}}{\alpha_f}\right) \end{bmatrix}$$

$$K_{3x3} = \begin{bmatrix} \left(1 + \left(\frac{\alpha_f}{\alpha_{srb}}\right)^3\right) & -1 & \left(\frac{L_f}{2}\left(\frac{\alpha_f}{\alpha_{srb}}\right)^3 - L_{srb}\right) \\ & \left(1 + \left(\frac{\alpha_f}{\alpha_{srb}}\right)^3\right) & \left(\frac{-L_f}{2}\left(\frac{\alpha_f}{\alpha_{srb}}\right)^3 + L_{srb}\right) \\ SYM. & & \left(\frac{2L_f^2}{3}\left(\frac{\alpha_f}{\alpha_{srb}}\right)^3 - L_{srb}^2\right) \end{bmatrix} \quad (102)$$

The initial motivation behind dividing by the semi-rigid beam stiffness in step one, is to divide out the presumed insignificant flexure stiffnesses from the 7 by 7 matrix by an "infinite" stiffness. This presumption is what was assumed as truth in the analytical model in section 3.2. However, the flexure to semirigid beam bending ratio of the first design, ß=4.1 (equation 101), indicates that the "rigid-beam" in the analytical model is actually more flexible than the "flexure" in *pure bending*. It cannot, however, be concluded that the truss model is inadequate for use as an initial estimate, since its accuracy is derived from modeling the kinematics of the device based on its deflected shape, regardless of the coupled bending stiffness interaction. It can be concluded that another assumption about

the bending stiffness ratio, β, is mandatory for simplifying the analytical model. It should also be noted that the *pure bending* ratio, β, is a practical non-dimensionalization parameter for matrix simplification. It is not necessarily an accurate ratio for comparing the total bending stiffness contributions of the flexure and semirigid beam to the effective stiffness of the component. Since the internal bending moment is zero in the center of the semirigid beam (point of counterflexure), and maximum at the ends of the flexures, the flexibility of the semirigid beam is relatively unexercized. A more useful bending ratio would also compare the flexibility of one flexure to *one-half* the semirigid beam, since there are two flexures for every semirigid beam.

The important simplification comes from recognizing three facts about the beam aspect ratio for the flexure and and semi-rigid beam.

Fact 1. The first design had beam aspect ratios of 16% and 10% for the flexure and semi-rigid beam, respectively. The thickness and, in turn, aspect ratio of the semi-rigid beam was semi-arbitrarily selected to please aesthetic requirements. Increasing the semi-rigid beam's thickness until both beam's aspect ratio were equal at 16% would have channeled more strain energy into the piezoelectric, while the effective stiffness of the component would remain relatively *insensitive* to such a modification. In conclusion, it is recommended that the aspect ratio of the semirigid beam should be greater than or equal to that of the flexure.

Fact 2. The geometrical constraints of the device limit the upper bound of the semi-rigid beam aspect ratio.

Fact 3. It can be argued that the technical efficacy of the device is improved as the aspect ratios converge toward the same value.

Fact 4. Since, the Bernoulli-Euler beam theory, used here, neglects the shear deflections important to "stubby" beams, it is important to limit the upper bound of the semi-rigid beam aspect ratio to the 10-20% range shared by the flexure.

All these facts suggest that arbitrarily equating aspect ratios is a harmless constraint that does not limit design alternatives, but rather, replaces arbitrary variable selection with a sound design rule:

$$\alpha = \alpha_f = \alpha_{srb} \tag{103}$$

Figure 58 illustrates that the imposed aspect ratio constraint does not limit design options.

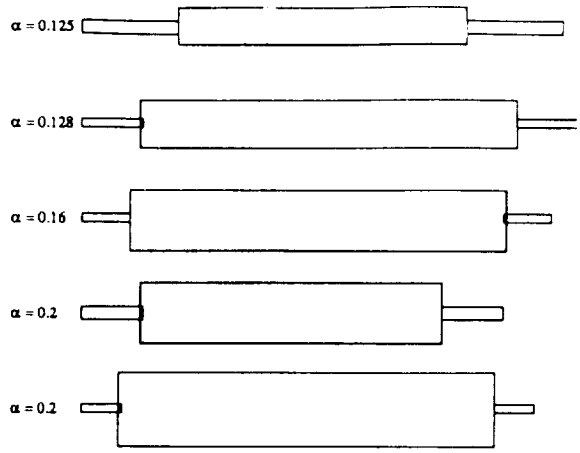

Figure 58. Five examples of lever arms with $\alpha_f = \alpha_{srb}$ illustrate that the aspect ratio constraint does not limit design options.

The aspect ratio constraint simplifies the matrices as follows:

$$R_a = \begin{bmatrix} \left(\frac{P}{8Eb\alpha^3}\right) \\ 0 \end{bmatrix}$$

$$K_{aa} = \begin{bmatrix} \left(\frac{K_{spring}}{2Eb\alpha^3} + \frac{1}{\alpha^2}(s\theta)^2 + \frac{1}{\alpha}(c\theta)^2\right) & 0 \\ 0 & \left(\frac{K_{piezo}}{4Eb\alpha^3} + \frac{1}{\alpha^2}(c\theta)^2 + \frac{1}{\alpha}(s\theta)^2\right) \end{bmatrix}$$

$$K_{ac} = \begin{bmatrix} \frac{1}{\alpha^2}(s\theta) & 0 & (-c\theta) & 0 & \frac{L_f}{2}(-c\theta) \\ 0 & \frac{1}{\alpha^2}(-c\theta) & 0 & (s\theta) & \frac{L_f}{2}(s\theta) \end{bmatrix}$$

$$K_{2x2} = \begin{bmatrix} \frac{2}{\alpha^2} & \frac{-1}{\alpha^2} \\ SYM. & \frac{2}{\alpha^2} \end{bmatrix}$$

$$K_{3x3} = \begin{bmatrix} 2 & -1 & \left(\frac{L_f}{2} - L_{srb}\right) \\ & 2 & \left(\frac{-L_f}{2} + L_{srb}\right) \\ SYM. & & \left(\frac{2L_f^2}{3} + L_{srb}^2\right) \end{bmatrix} \qquad (104)$$

The simplicity of matrix (104) is appreciated when considering that the initial matrix inversion involved a densely populated six by six matrix. The assembled stiffness matrix is now a function of the lever angle, the aspect ratio, the semi-rigid beam and flexure lengths and the piezoelectric properties. The aspect ratio is the ideal parameter for designing the flexure and constraining the semi-rigid beams thickness. A similar relationship between the two beam lengths is needed to eliminate impractical designs. Obviously, cases where $L_f > L_{srb}$ are of no interest to the designer. The following substitution will be made:

$$L_{srb} = nL_n \tag{105}$$

where $n > 8$.

The scaling parameter, n, defines the size of the component and will later indicate when the beam can be assumed a rigid beam.

$$K_{3x3} = \begin{bmatrix} 2 & -1 & -\left(n-1/2\right)L_f \\ & 2 & \left(n-1/2\right)L_f \\ SYM. & & \left(n^2+2/3\right) \end{bmatrix} \tag{106}$$

Substitute $$\bar{m} = \left(n^2 + 2/3\right), \quad \bar{n} = \left(n - 1/2\right) \tag{107}$$

into (106) to yield: $$K_{3x3} = \begin{bmatrix} 2 & -1 & -\bar{n}L_f \\ & 2 & \bar{n}L_f \\ SYM. & & \bar{m}L_f^2 \end{bmatrix} \tag{108}$$

Inverting (108) yields:

$$K_{3x3}^{-1} = \frac{1}{\left(3\bar{m}L_f^2 + 2\bar{n}^2L_f^2\right)} \begin{bmatrix} -2\bar{m}L_f^2 + \bar{n}^2L_f^2 & -\bar{m}L_f^2 + \bar{n}^2L_f^2 & -\bar{n}L_f \\ & -2\bar{m}L_f^2 + \bar{n}^2L_f^2 & \bar{n}L_f \\ SYM. & & -3 \end{bmatrix} \tag{109}$$

Assuming that $\bar{n}^2 = \bar{m} = n^2$, simplifies the matrix inversion with single term matrix elements. Without this substitution, the static condensation matrix multiplications in the next solution step produce too many terms to be used in a simple analytical tool.

$$K_{3x3}^{-1} = \frac{1}{5} \begin{bmatrix} -1 & 0 & \dfrac{-1}{nL_f} \\ & -1 & \dfrac{1}{nL_f} \\ SYM. & & \dfrac{-3}{\left(nL_f\right)^2} \end{bmatrix} \tag{110}$$

The errors associated with substituting $\bar{n}^2 = \bar{m} = n^2$ into (106) are graphed in figure 59. The errors indicate that a maximum 5% error is introduced into the matrices, if n > 20. For n < 20, the model is less useful, due to the large matrix substitution errors. Thus, this constraint does limit design options, unlike the unnoticable aspect ratio constraint. It should be noted that the current design cannot be modeled with this analysis, since n = 8 to satisfy a stress factor of safety of 4.0. The model is practical if a small flexure to semirigid-beam size ratio is desired for the sake of performance at the expense of the flexure's yield stress safety factor.

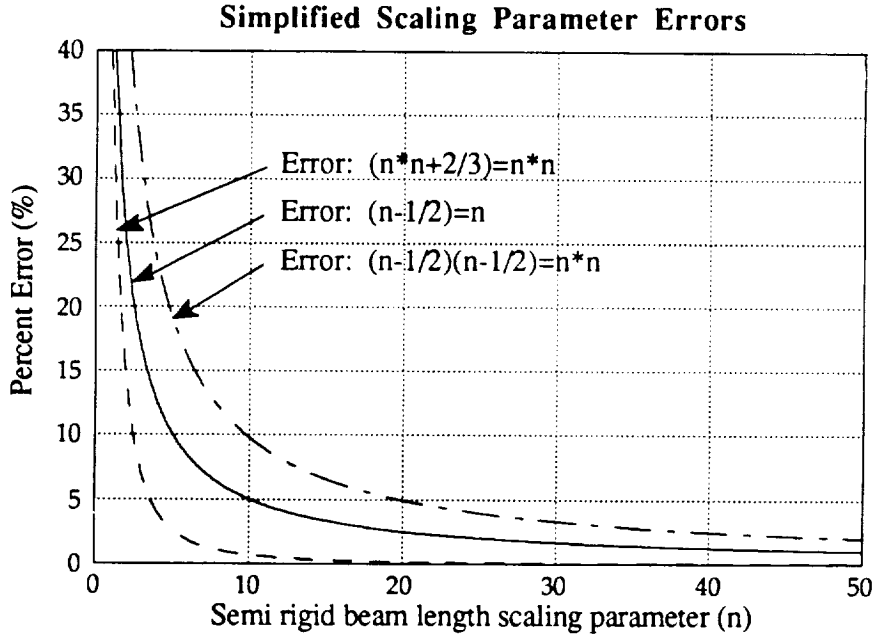

Figure 59. Simplified Scaling Parameter Errors

Now that the five by five matrix has been inverted successfully with single term elements in the resulting matrix, static condensation of the undesired degrees of freedom is accomplished with the following matrix multiplication,

$$K_a = \left(K_{aa} - K_{ac}K_{cc}^{-1}K_{ca}\right)$$

where, $$K_a U_a = R_a \qquad (111)$$

Multiplying (111) by $2Eb\alpha^3$ yields the 2x2 effective stiffness matrix equation:

Q-2.

$$\left[\begin{array}{c|c} \left(\frac{2Eb(\sin\theta)^2}{3}\right)\alpha & 2Eb(\cos\theta)(\sin\theta)\left(\frac{\alpha}{3}-\frac{3\alpha^3}{20n^2}\right) \\ +2Eb(\cos\theta)^2\left(\alpha^2+(Q)\alpha^3\right) & \\ \hline SYM. & \frac{K_{piezo}}{2}+\left(\frac{2Eb(\cos\theta)^2}{3}\right)\alpha \\ & +2Eb(\sin\theta)^2\left(\alpha^2+(R)\alpha^3\right) \end{array}\right]\left[\begin{array}{c} V_1 \\ \\ U_4 \end{array}\right]=\left[\begin{array}{c} 0.25P \\ \\ 0 \end{array}\right] \tag{112}$$

where, $$Q=\frac{1}{5}+\frac{1}{5n}+\frac{3}{20n^2} \text{ and } R=Q-\frac{2}{5n}, \tag{113}$$

The Q and R coefficients are analogous to a finite element's "pure bending" stiffness coefficients because they are multiplied by the cubic aspect ratio, α^3. Likewise, the terms depending on the α^2 are "shear-bending" coefficients, and the terms depending on α are the "axial" coefficients.

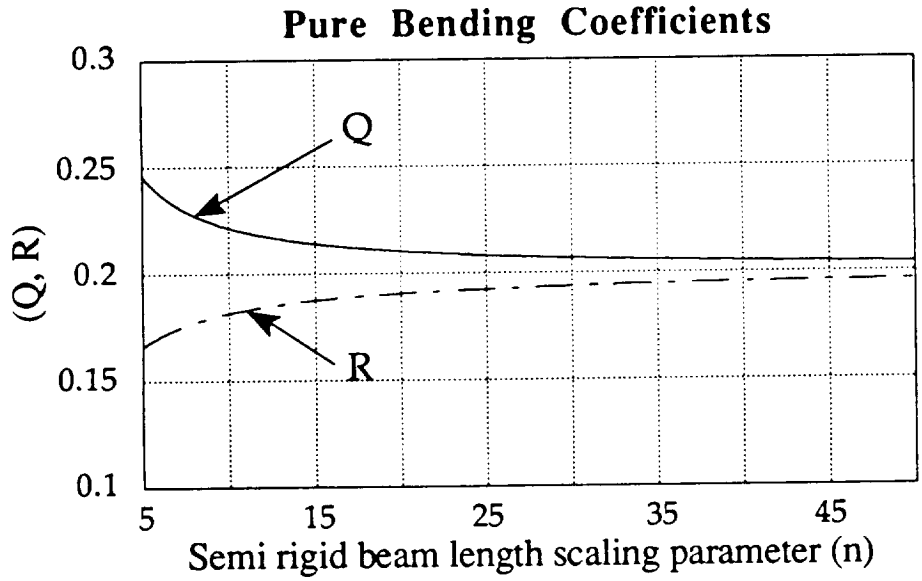

Figure 60. The discrepancy between Q and R is indicative of the 5% simplification errors imposed during static condensation.

Since static condensation pre-and-post-multiplied a symmetric matrix by another matrix, pure bending from node 4 should be resisted by the same stiffness as pure bending from node 1, (with exception to the sine-squared and cosine-squared term differences at the opposite ends of the lever arm which are responsible for transforming "pure-bending" moments and rotations into the model's forces and displacements, v1 and u4). Since this is not the case, since Q does not equal R for all n. The discrepancy between Q and R, in

figure 60, is indicative of the 5% simplification errors imposed during static condensation. Thus, for n > 20, Q = R = 0.2.

Since, $\frac{-3}{20n^2} << \frac{1}{3}$, for n > 20, the matrix (112) becomes,

$$\left[\begin{array}{l|l} \left(\frac{2Eb(\sin\theta)^2}{3}\right)\alpha & \left(\frac{2Eb(\cos\theta)(\sin\theta)}{3}\right)\alpha \\ +2Eb(\cos\theta)^2\left(\alpha^2+0.2\alpha^3\right) & \\ \hline SYM. & \frac{K_{piezo}}{2}+\left(\frac{2Eb(\cos\theta)^2}{3}\right)\alpha \\ & +2Eb(\sin\theta)^2\left(\alpha^2+0.2\alpha^3\right) \end{array}\right]\left[\begin{array}{c} V_1 \\ \\ U_4 \end{array}\right]=\left[\begin{array}{c} 0.25P \\ \\ 0 \end{array}\right] \tag{114}$$

Due to the fact that this does not look like an ordinary stiffness matrix, it is insightful to resubstitute the original beam properties into this matrix.

$$\alpha=\frac{t}{L},\quad A=bt,\quad I=\frac{bt^3}{12} \tag{115}$$

$$\left[\begin{array}{l|l} \frac{(\sin\theta)^2}{3}\left(\frac{2EA}{L}\right) & \\ +\frac{2(\cos\theta)^2}{t}\left(\frac{12EI}{L^2}\right) & \frac{(\sin\theta)(\cos\theta)}{3}\left(\frac{2EA}{L}\right) \\ +\frac{(\cos\theta)^2}{5}\left(\frac{24EI}{L^3}\right) & \\ \hline SYM. & \frac{K_{piezo}}{2}+\frac{(\cos\theta)^2}{3}\left(\frac{2EA}{L}\right) \\ & +\frac{2(\sin\theta)^2}{t}\left(\frac{12EI}{L^2}\right) \\ & +\frac{(\sin\theta)^2}{5}\left(\frac{24EI}{L^3}\right) \end{array}\right]\left[\begin{array}{c} V_1 \\ \\ U_4 \end{array}\right]=\left[\begin{array}{c} 0.25P \\ \\ 0 \end{array}\right]$$

where,

$$\left[\begin{array}{l|l} a & b \\ \hline b & c \end{array}\right]\left[\begin{array}{c} V_1 \\ U_4 \end{array}\right]=\left[\begin{array}{c} 0.25P \\ 0 \end{array}\right] \tag{116}$$

The first term in the "a" matrix element can now be easily deciphered as the double beam's axial stiffness, of three-series-element lever arm, transformed through theta to v1. The second and third terms in "a" together model the bending stiffness of the lever arm in shear.

The effective stiffness of the component can be found by

$$Keff = \frac{P}{4v_1} = a - \frac{b^2}{c} \tag{117}$$

The percentage of the total strain energy that is in the piezoelectric is found by

$$\%U_{piezo} = \frac{U_{piezo}}{U_{total}} = \frac{K_{piezo}}{K_{eff}}\left(\frac{u_4}{v_1}\right)^2 = \frac{b^2}{c\left(ac - b^2\right)} \tag{118}$$

The aspect ratio that corresponds to the maximum strain energy in the piezoelectric can be found by finding the roots to the fifth-order equation:

$$\frac{\partial}{\partial \alpha}\left(U_{piezo}\right) = 0. \tag{119}$$

APPENDIX II

LOW-FREQUENCY ASTREX MODE SHAPES

As depicted in the transfer functions of chapter 5, the high-amplitude dynamics below 35 Hertz are an order of magnitude larger, and thus more influencial to the performance of the testbed. Although the passive damping implementation was targeted for a higher frequency bandwidth to facilitate line of sight control roll-off, a careful look at the first 18 mode shapes, indicates that the low-frequency testbed dynamics are simply the larger modal displacements of the apex. Although there is significant modal deformation in the backplane, the largest modal displacements of the structure are primarily due to tripod bending. The following mode shapes are also helpful in appreciating the need for a tuned-mass damper in the apex.

BIBLIOGRAPHY

[1]R. Guela, A. H. von Flotow, D. W. Vos, "Passive Damping for Robust Control of Flexible Structures," *AIAA Journal of Guidance, Control and Dynamics*, in press, 1993.

[2]A. H. von Flotow and D. W. Vos, "The Need for Passive Damping in Feedback Controlled Flexible Structures," *Shock and Vibration Symposium*, 1990, pp. 1-2.

[3]Ashley, H. and Edberg, D.L., "On the Virtues and Prospects for Passive Damping in Large Space Structures," *Proceedings of the Damping '86 Conference*, Flight Dynamics Lab., Air Force Wright Aeronautical Labs., OH, Rept. AFWAL-TR-86-3059, March, 1986, pp. DA-1-DA-7.

[4]N. W. Hagood, and A.H. von Flotow, "Damping of Structural Vibrations with Piezoelectric Materials and Passive Electrical Networks," *Journal of Sound and Vibration*, April-May, 1991.

[5]G. Chen, and B. K. Wada, "Passive Damping for Space Truss Structures," *Proceedings of the 29th AiAA/ASME/ASCE/AHS Structures, Structural Dynamics, and Materials Conference*, AIAA Paper 88-2469, Washington, DC, May 1988, pp.1742-1749.

[6]J. L. Fanson and T. K. Caughey, "Positive Position Feedback Control for Large Space Structures," *Proceedings of the 28th AIAA/ASME/ASCE/AHS Structures, Structural Dynamics and Materials Conference*, AIAA Paper No. 87-0902, April 1987, pp. 588-598.

[7]J. F. Wilson and L. P. Davis, "Very High Damping in Large Space Structures," *ASME Vibration Damping Conference Proceedings*, 1988, pp. 167-171.

[8]B. K. Wada, and D. L. Edberg, "Adaptive Damping for Spacecraft by Temperature Control," *ASME Vibration Damping Conference Proceedings*, 1988, pp. 89-92.

[9]P. J. Torvik, W. Gibson, "The Design and Effectiveness of Impact Dampers for Space Applications," *ASME Vibration Damping Conference Proceedings*, 1988, pp. 65-74.

[10]J. Fanson, G. Blackwood, and C. Chu, "Active-Member Control of Precision Structures," *Proceedings of the 30th AIAA/ASME/ASCE/AHS Structures, Structrual Dynamics, and Materials Conference*, AIAA Paper 89-1329, Washington, DC, May 1989, pp.1480-1494.

[11]R.L. Forward, "Electronic Damping of Vibrations in Optical Structures," *Journal of Applied Optics*, 1979, pp. 690-697.

[12]T. R. Gururaja, D. Christopher, R. E. Newnham and W. A. Schulze, "Continuous Poling of PZT Fibers and Ribbons and its Application to New Devices," *Ferroelectrics*, New York: Gordon and Breach, 1983, pp. 193-200.

[13]E. F. Crawley and J. DeLuis, "Use of Piezoelectric Actuators as Elements of Intelligent Structures," *American Institute of Aeronautics and Astronautics*, Journal 25 (10), 1987, pp. 1373-1385.

[14]N. W. Hagood, and E. F. Crawley, "Experimental Investigation of Passive Enhancement of Damping for Space Structures," *Journal of Guidance, Control, and Dynamics*, Nov.-Dec. 1991, pp. 1100-1109.

[15]S. Hanagud, M. W. Obal, and A. J. Calise, "Optimal Vibration Control by the Use of Piezoceramic Sensors and Actuators," *Proceedings 28th AIAA/ASME/ASCE/AHS Structures, Structural Dynamics, and Materials Conference*, Monterey, CA, AIAA Paper No. 87-0959, April 1987, pp. 987-997.

[16]T. Bailey and J. E. Hubbard, "Distributed Piezoelectric-Polymer Active Vibration Control of a Cantilever Beam," *Journal of Guidance Control and Dynamics*, AIAA, **8** (5), , 1985, pp. 605-611.

[17]D. Pines and A. H. von Flotow, "Active Control of Bending Wave Propagation at Acoustic Frequencies," *Journal of Sound and Vibration*, 1990, pp. 391-412.

[18]A. H. von Flotow, N. W. Hagood, K. Napolitano, E. Austin, L. P. Davis, "A Case Study in Passive Piezoceramic, Viscous and Viscoelastic Damping," *Proceedings of the International Symposium on Active Materials and Adaptive Structures*, Alexandra, VA, Nov. 4-8, 1991.

[19]D. R. Morgenthaler, "Design and Analysis of Passively Damped Large Space Structures," *ASME Vibration Damping Conference Proceedings*, 1988, pp. 1-8.

[20]R. A. Flinn, *Engineering Materials and Their Applications*, New York, Houghton Mifflin, 1986, pp. 77.

[21]Zygo Corporation, *AXIOM Laser Measurement System Reference Guide*, New York, Zygo Corporation, 1988, pp. 2-1 to 2-22.

[22]Specialty Engineering Associates, Inc., *Piezoelectric Material Properties Verification using Impedence Frequency Response Results Summary*, Santa Cruz, CA, 1993, pp. 1-2.

[23]J. Jaung, "Optimal Design of a Passive Vibration Absorber for a Truss Beam," *Journal of Guidance, Control, and Dynamics*, Vol. 7, No. 6, 1984, pp.733-739.

[24]L. Peterson, J. Allen, J. Lauffer, A. Miller, and R. Skelton, "An Experimental and Analytical Synthesis of Controlled Structure Design," *Proceedings of the 30th AIAA/ASME/ASCE/AHS Structures, Structural Dynamics and Materials Conference*, AIAA Paper 89-1170, Washington, DC, May 1989, pp. 91-103.

[25]J.B. Aldrich, N.W. Hagood, A.H. von Flotow, and D.W. Vos, "Design of Passive Piezoelectric Damping for Space Structures," *Smart Structures and Intelligent Systems Conference Proceedings*, Albuquerque, NM, 1993. pp. 1-13.

[26]R.N. Gehling, "Large Space Structure Damping Treatment Performance: Analytic and Test Results," *ASME Vibration Damping Conference Proceedings*, 1988, pp. 93-100.

[27]E Hilbrandt, and L. Kolsch, "Damping in Spacecraft Structures--A Review of Research and Hardware Development in European Space Programs," *ASME Vibration Damping Conference Proceedings*, 1988, pp. 173-185.

[28]G.H. Blackwood, R.N. Jacques, D.W. Miller, "The MIT Multipoint Alignment Testbed: Technology Development for Optical Interferometry," *SPIE Conference on Active and Adaptive Optical Systems*, 1991, pp. 1-15.

REPORT DOCUMENTATION PAGE

Form Approved
OMB No. 0704-0188

1. AGENCY USE ONLY (*Leave blank*)	2. REPORT DATE	3. REPORT TYPE AND DATES COVERED
	September 1994	Contractor Report

4. TITLE AND SUBTITLE
Design of Passive Piezoelectric Damping for Space Structures

5. FUNDING NUMBERS
C NAS1-19381

WU 590-14-91-52

6. AUTHOR(S)
Nesbitt W. Hagood IV, Jack B. Aldrich, and Andreas H. von Flotow

7. PERFORMING ORGANIZATION NAME(S) AND ADDRESS(ES)
Massachusetts Institute of Technology
77 Massachusetts Avenue
Room 33-313
Cambridge, MA 02139-4307

8. PERFORMING ORGANIZATION REPORT NUMBER

9. SPONSORING / MONITORING AGENCY NAME(S) AND ADDRESS(ES)
National Aeronautics and Space Administration
Langley Research Center
Hampton, VA 23681-0001

10. SPONSORING / MONITORING AGENCY REPORT NUMBER
NASA CR-4625

11. SUPPLEMENTARY NOTES
Langley Technical Monitor: Rudeen Smith-Taylor
Final Report

12a. DISTRIBUTION / AVAILABILITY STATEMENT
Unclassified - Unlimited
Subject Category 18

12b. DISTRIBUTION CODE

13. ABSTRACT (*Maximum 200 words*)

Passive damping of structural dynamics using piezoceramic electromechanical energy conversion and passive electrical networks is a relatively recent concept with little implementation experience base. This report describes an implementation case study, starting from conceptual design and technique selection, through detailed component design and testing to simulation on the structure to be damped. About 0.5kg. of piezoelectric material was employed to damp the ASTREX testbed, a 5000kg structure. Emphasis was placed upon designing the damping to enable high bandwidth robust feedback control. Resistive piezoelectric shunting provided the necessary broadband damping. The piezoelectric element was incorporated into a mechanically-tuned vibration absorber in order to concentrate damping into the 30 to 40Hz frequency modes at the rolloff region of the proposed compensator. A prototype of a steel flex-tensional motion amplification device was built and tested. The effective stiffness and damping of the flex-tensional device was experimentally verified. When six of these effective springs are placed in an orthogonal configuration, strain energy is absorbed from all six degrees of freedom of a 90kg. mass.

A NASTRAN finite element model of the testbed was modified to include the six-spring damping system. An analytical model was developed for the spring in order to see how the flex-tensional device and piezoelectric dimensions effect the critical stress and strain energy distribution throughout the component. Simulation of the testbed demonstrated the damping levels achievable in the completed system.

14. SUBJECT TERMS	15. NUMBER OF PAGES
Passive Damping, Piezoceramic, Simulation, Flex-Tensional Device	96
	16. PRICE CODE: A05

17. SECURITY CLASSIFICATION OF REPORT	18. SECURITY CLASSIFICATION OF THIS PAGE	19. SECURITY CLASSIFICATION OF ABSTRACT	20. LIMITATION OF ABSTRACT
Unclassified	Unclassified		